DOCTOR OF PHILOSOPHY

The interaction between tides, ice shelves and ice streams

Rosier, Sebastian

Award date:
2015

Awarding institution:
Bangor University

Bangor University

Doctoral Thesis

The Interaction Between Tides, Ice Shelves and Ice Streams

Author:
Sebastian H. R. Rosier

Supervisors:
J. A. M. Green
G. Hilmar Gudmundsson

A thesis submitted in fulfilment of the requirements for the degree of Doctor of Philosophy

in the

School of Ocean Sciences

November 2015

for Dad

Abstract

Observation of ice-stream and ice-shelf flow has revealed interaction with the ocean tide, in some cases far upstream of the grounding line. Ice-stream velocities can be greatly affected by local ocean tides at a variety of timescales but of particular interest is a fortnightly modulation in flow that has been observed on the Rutford Ice Stream. This frequency is absent in the forcing, far stronger than the dominant tidal constituent signals and has been observed far inland. Understanding what mechanism can produce this signal can provide a window into mechanisms at the base of the ice stream that affect its flow. A consequence of this nonlinearity is that the mean flow of the Rutford Ice Stream is increased in comparison to a situation where no tidal forcing is present, implying that changes in tides could alter the long term flow of ice from Antarctica. Since local tides are sensitive to bathymetry which can change drastically due to changes in ice-shelf geometry and grounding line position, a feedback exists between tides and the ice sheet whereby changes in the flow of ice could alter tides which in turn would change the ice velocity. This thesis presents results from both ice-stream/shelf and tidal models to investigate these two mechanisms. Firstly a nonlinear 3D viscoelastic full-Stokes finite element model explores possible sources of nonlinearity that can produce fortnightly modulation in ice-stream flow far upstream of the grounding line. This model looks at stress transmission, grounding zone flexure, hydrology and grounding line migration and the conclusion is that tidally-induced changes in the subglacial water pressure play the largest role in producing this effect. Then, the OTIS tidal model is used to demonstrate that reduction in the thickness and/or extent of ice-shelves, in particular the Filchner-Ronne ice shelf, could greatly impact both tidal amplitudes and dissipation rates in the region. The research in this thesis clearly shows the importance of tidal interactions with the Antarctic ice sheet and that these are not limited to short temporal timescales.

Acknowledgements

I would like to begin by thanking the patience of my many officemates, both at Bangor and BAS, who have had to listen to me complain about model issues throughout my studies. Particular thanks must go to William for our long talks about life, Ian for late night office racket sports and Richard for always putting me in my place. My time at BAS would have been much less enjoyable without the friendship and support of the many people who work there; Jan, Rob, Jonny and Alex and many others but especially Carlos who has guided me through from the start. Thanks to all of you for always being so generous with your time.

Thanks to everyone in team Angorfa, what an amazing house and great year! I want to say a special thank you to my good friends Benny and Harriet, you both changed my outlook on life completely.

Now I should thank the people responsible for setting me on my path that has lead me to BAS and getting me excited about research. Firstly Thank you to James, your guided walks through Cwm Idwal and Snowdon helped stoke my interest in glacial processes. My irrational hatred for physics, ingrained during secondary school, was snuffed out by Alan Davies and Tom Rippeth. Thankyou both for making me see the light!

I certainly would not have been able to continue my studies for so many years without the support of my family. Nick and Alex, you're the best brothers I could ask for, I miss you both a lot! Mum, I could write so much here but I don't think you'd want anyone else to read it so I will just say thank you for always being there at the drop of a hat and always supporting me.

Victoria, thank you for always making me smile, for putting up with my work schedule and trips to Antarctica and for being the most kind and thoughtful person I know. We cannot see each other as often as we'd like but I hope that will change soon.

Finally, I owe so much to my two supervisors. Mattias, thanks for your humour, all your support and for being so patient and understanding in my move to Cambridge. Hilmar, I am so grateful for the opportunity to work at BAS; it has been an incredible experience. Working alongside you is always fun and exciting and has been a huge motivating force during the course of my Ph.D., Thank you!

Contents

List of Figures

List of Tables

Abbreviations & Acronyms

AIS	**A**ntarctic **I**ce **S**heet
CATS	**C**ircum- **A**ntarctic **T**idal **S**imulation
FRIS	**F**ilchner-**R**onne **I**ce **S**helf
FS	**F**ull-**S**tokes
GPS	**G**lobal **P**ositioning **S**ystem
HT	**H**alf **T**hickness
HTE	**H**alf **T**hickness and **E**xtent
InSAR	**In**terferometric **S**ynthetic **A**perture **R**adar
ISS	**I**ce **S**team/**S**helf
LGM	**L**ast **G**lacial **M**aximum
LHS	**L**eft **H**and **S**ide
OTIS	**O**regon state university **T**idal **I**nversion **S**oftware
RIS	**R**utford **I**ce **S**tream
RHS	**R**ight **H**and **S**ide
RMS	**R**oot **M**ean **S**quare
SAL	**S**elf **A**ttraction and **L**oading
SLE	**S**ea **L**evel **E**quivalent
SSA	**S**hallow **S**helf **A**pproximation
SSHV	**S**ea **S**urface **H**eight **V**ariability
TPF	**T**ide **P**roducing **F**orce
WAIS	**W**est **A**ntarctic **I**ce **S**heet

Symbols

General

$x,\ y,\ z$	along-flow, across-flow and vertical coordinates	
$u,\ v,\ w$	along-flow, across-flow and vertical velocity	ms^{-1}
ρ_i	ice density	$\mathrm{kg\,m}^{-3}$
ρ_w	ocean density	$\mathrm{kg\,m}^{-3}$
ω	angular frequency	$\mathrm{rad\,s}^{-1}$
k	wavenumber	m^{-1}
H	water column thickness	m
h	ice thickness	m
d	ice draft	m
b	basal ice profile	m
B	bed profile	m
s	surface ice profile	m
S	sea level	m
z	depth below surface	m
p	pressure	Pa
T	Period	s
g	gravitational acceleration	$\mathrm{m\,s}^{-2}$
p	pressure	Pa

Ice physics

$\boldsymbol{\sigma}$	stress tensor	Pa
$\boldsymbol{\epsilon}$	strain tensor	dimensionless
$\boldsymbol{\tau}$	deviatoric stress tensor	Pa
$\mathbf{e}$	deviatoric strain tensor	dimensionless
$I_1,\ I_2,\ I_3$	first, second and third invariants	Pa
σ_n	normal stress	Pa
τ_e	effective stress	$\mathrm{Pa}^{1/2}$
τ_b	basal resistive stress	Pa
τ_d	driving stress	Pa
τ_L	longitudinal drag	Pa
τ_w	sidewall drag	Pa
τ_E	effective stress	Pa
E	Young's Modulus	Pa
G	Shear Modulus	Pa
η	ice viscosity	Pa s
α	surface ice slope	dimensionless
β	bed slope	dimensionless
λ	Maxwell relaxation time	s
u_b	basal slip velocity	$\mathrm{m\,s^{-1}}$
u_d	deformational velocity	$\mathrm{m\,s^{-1}}$
c_s	slip ratio	dimensionless
p_w	water pressure	Pa
p_i	ice overburden pressure	Pa
κ	permeability	$\mathrm{m^2}$
p_b	buttressing	Pa
ν	Poisson's ratio	dimensionless
$\hat{h}$	hydraulic head	m
N	effective pressure	Pa
K	hydraulic conductivity	$\mathrm{m^2\,s^{-1}}$

m	stress exponent	dimensionless
q	effective pressure exponent	dimensionless
n	Glen's law exponent	dimensionless
A	rate factor	Pa^{-n}
R_a	bedrock bump spacing	m
c	slipperiness	$\mathrm{m\,s^{-1}\,Pa^{-(m-q)}}$
S_s	specific storage	$\mathrm{m^{-3}}$
ξ	effective pressure perturbation	dimensionless
c'	slipperiness distribution	$\mathrm{m\,s^{-1}\,Pa^{-m}}$
$\wp$	ρ_i/ρ_w density ratio	dimensionless
γ	up ($^+$) or downstream ($^-$) migration parameter	dimensionless
L	grounding line migration distance	m
L_e	elastic stress-coupling length scale	m
L_v	viscous stress-coupling length scale	m
L_{ve}	viscoelastic stress-coupling length scale	m
λ_c	a-priori slipperiness length scale	m
$\mathbf{K}$	transfer function matrix	
$\hat{\mathbf{S}}$	Fischer information matrix	
$\mathbf{S}_e$	measurement error covariance matrix	
$\mathbf{S}_a$	a-priori error covariance matrix	

Tides

μ	viscosity of water	Pa s
F_b	bed friction	$\mathrm{m^2\,s^{-2}}$
F_w	tidal conversion	$\mathrm{m^2\,s^{-2}}$
f	coriolis acceleration	$\mathrm{s^{-1}}$
S_{EQ}	equilibrium tide	m
C_d	drag coefficient	dimensionless
S_{SAL}	ocean SAL	m
G_c	gravitational constant	$\mathrm{m^3\,kg^{-1}\,s^{-2}}$

T_f	natural oscillation period	s
L_c	bay length	m
L_R	Rossby radius	m
W	work done by TPF	$\mathrm{kg\,m^2\,s^{-2}}$
D	tidal dissipation	$\mathrm{kg\,m^2\,s^{-2}}$
P	barotropic energy flux	$\mathrm{kg\,m^2\,s^{-2}}$

Mathematical

$\mathbf{I}$	identity matrix
δ	Kronecker delta
ε_{ijk}	Alternating unit tensor
$\hat{\mathbf{n}}$	unit normal vector
$\hat{\mathbf{t}}$	unit vector perpendicular to $\hat{\mathbf{n}}$
tr	matrix trace
det	matrix determinant
∂_x	partial derivative with respect to x
$\frac{D}{Dt}$	Material (Langrangian) derivative

Chapter 1

Introduction

1.1 Background and motivation for this study

The Antarctic Ice Sheet (AIS, Fig. 1.1) is surrounded by ocean and changes in this boundary forcing have important implications for its flow and future evolution. Ocean tides play an important role in ice dynamics of the continent; inducing currents that alter basal melting beneath the floating ice shelves [Makinson et al., 2011, Mueller et al., 2012], affecting the motion of the ice shelves [Brunt et al., 2010, Doake et al., 2002, Makinson et al., 2012] and causing changes in short term and mean flow of ice streams, often far upstream of the grounding line [Aðalgeirsdóttir et al., 2008, Anandakrishnan et al., 2003, Bindschadler et al., 2003a,b, Gudmundsson, 2006, King et al., 2010, Marsh et al., 2013, Murray et al., 2007, Winberry et al., 2009, 2011]. This interaction is reciprocal, since any change in the thickness of the ice shelf will change the local water column thickness beneath the shelf, thereby altering the ocean tide [Rosier et al., 2014a].

Understanding how the AIS reacts to external forcings is crucial to enable accurate predictions of its response to climate change. Currently the greatest uncertainty in future sea level rise arises in the difficulties of modeling this large and complex ice sheet [Vaughan, 2005]. Overall the AIS contains 58 m sea level equivalent (SLE) and 5 mm of SLE pass in and out of the ice sheet every year [Rignot et al., 2013,

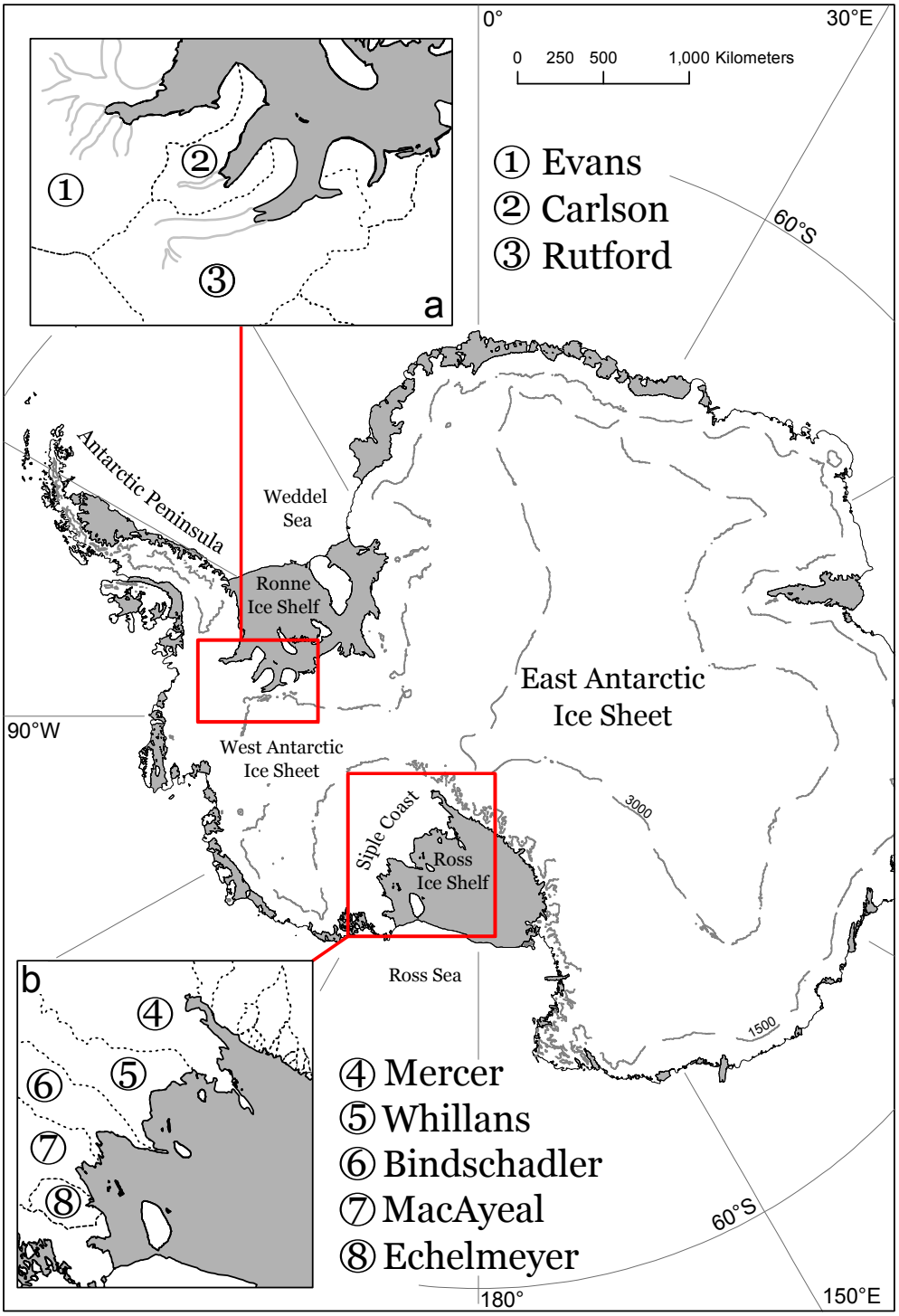

FIGURE 1.1: Map of Antarctica, showing the main locations mentioned in the text including active ice streams of the Siple Coast and Ronne Ice Shelf. Grounded ice is shown in white and ice shelves in gray. Dotted lines indicated drainage basins, gray lines show the outline of topographic ice streams and dashed lines are the 1500 and 3000m surface contours. Data from BEDMAP2 [Fretwell et al., 2013] and the Antarctic Digital Database (http://www.add.scar.org).

Vaughan, 2005]. The impact of even a small portion of the total AIS SLE being released would be devastating for the billions of people who live in coastal regions.

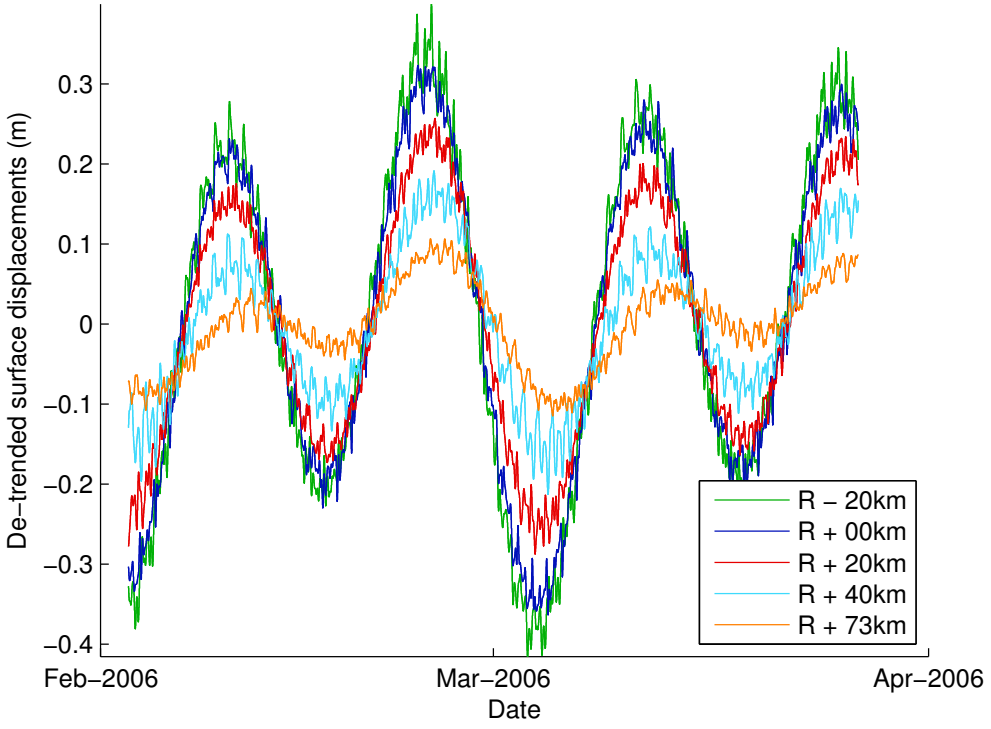

FIGURE 1.2: Tidal re-analysis of the de-trended surface velocities of the RIS. Original GPS data was put into the t_tide [Pawlowicz et al., 2002b] matlab package which performs classical harmonic analysis to determine tidal constituents and the predicted tides arising from this calculation are plotted.

Tides provide a unique insight into ice-stream dynamics which can help improve ice-sheet models and produce more accurate predictions for future sea level rise. Floating ice shelves are moved vertically by the ocean tide and, where the tidal range is large, this can have large affects on any adjoining ice streams. Through this process the tide can act as a natural experiment, perturbing ice streams in a predictable way which is clearly visible in data and that we can attempt to model. Arguably the most interesting effect is the nonlinear M_{sf} response first observed on the Rutford ice stream (RIS; Gudmundsson 2006). Figure 1.2 shows de-trended surface velocities from Global Positioning System (GPS) measurements collected at distances of up to 73 km upstream from the grounding line. The tidal forcing at the grounding line of the RIS is dominated by the semi-diurnal tidal constituents (M_2 and S_2 , see Table 4.1) however the response is at a fortnightly M_{sf} frequency,

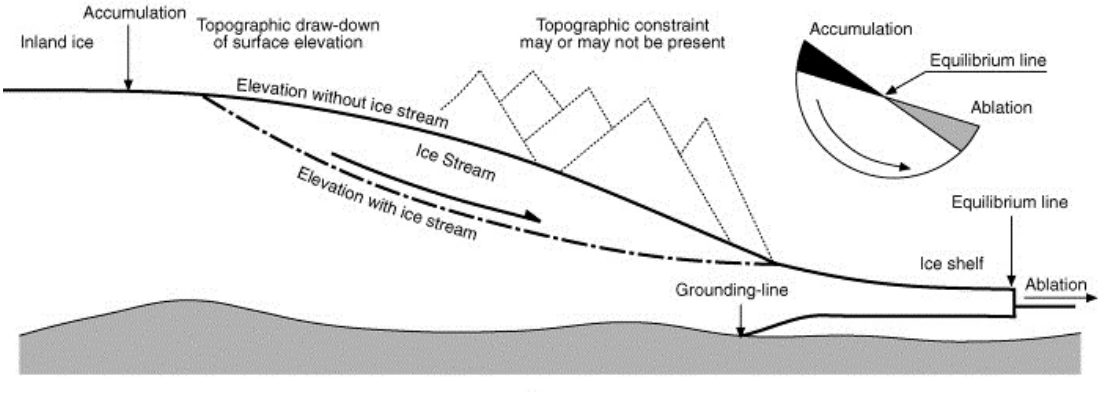

FIGURE 1.3: Schematic diagram of an ice stream, adapted from Bennett [2003]

and causes up to 20% change in peak to peak velocity. Re-producing this effect in models of ice-stream flow is not trivial and can help constrain model parameters which are often considered free.

In this introductory chapter I will briefly introduce the Antarctic region and the main processes relevant to this work. I focus somewhat on the RIS since a large part of the motivation for this study comes from data collected on that ice stream. I then summarise the ways in which tides interact with the ice-sheet and the work that has been previously done in this field.

1.2 The Antarctic ice sheet

The AIS is the largest body of ice on the planet, covering an area of fourteen million square kilometers and greater than 4 km thick in some places. The AIS is characterized by slow moving ice divides, fast moving ice streams and floating ice shelves. An ice stream is a portion of the ice sheet that moves much faster than surrounding ice, typically due to the presence of water and/or deforming sediments at its base. Some of the key features and processes of an ice stream are shown schematically in Fig 1.3. Ice shelves occur where ice begins to float and move rapidly due to gravity driven viscous spreading. Ice that is resting on a solid

bed is 'grounded' and the point at which the transition from grounded to floating ice occurs is called the grounding line.

Figure 1.4 shows surface ice velocity of the AIS derived from various remote sensing techniques [Rignot et al., 2011]. The ice streams are clearly visible as fast moving stream-like features which flow into the even faster flowing ice shelves. The two largest ice shelves are the Ross ice shelf (bordering the Ross Sea) and the Filchner-Ronne ice shelf (FRIS, bordering the Weddel Sea).

The AIS is generally divided into three regions; the Antarctic peninsula, East and West Antarctica. East Antarctica constitutes the majority of the continent's ice mass and large areas around the ice divide are slow moving. Because the bulk of the East Antarctic ice sheet lies on bedrock above sea level this portion of the ice sheet is generally considered to be stable, with a slightly positive mass balance [Davis et al., 2005, Pritchard et al., 2009, Rignot, 2006, Shepherd et al., 2012]. The West Antarctic ice sheet (WAIS) on the other hand is considered much more vulnerable to climate change because it is a marine ice sheet, that is to say that much of it is grounded below sea level.

Mercer [1978] and Weertman [1974] first pointed out the danger of a collapse of the WAIS and since then much observational and modeling work has been done to determine the timescales and implications. A general consensus is that an ice sheet cannot be stable on a retrograde slope and so if ice streams retreat beyond current pinning points to areas where this is the case the resultant ice loss will be rapid and dramatic [Katz and Worster, 2010, Robison et al., 2010, Schoof, 2007a,b, Thomas and Bentley, 1978, Wilchinsky, 2001]. This unconditional instability has been shown to only be true in 1HD (one horizontal dimension) however, and in 3D an ice-sheet may be stable on a retrograde slope [Gudmundsson, 2013, Gudmundsson et al., 2012]. Ultimately whether or not an ice-sheet is stable on a retrograde slope appears dependant on the local stress regime along the grounding line, however there is an undeniable danger that the WAIS is particularly vulnerable to climate warming.

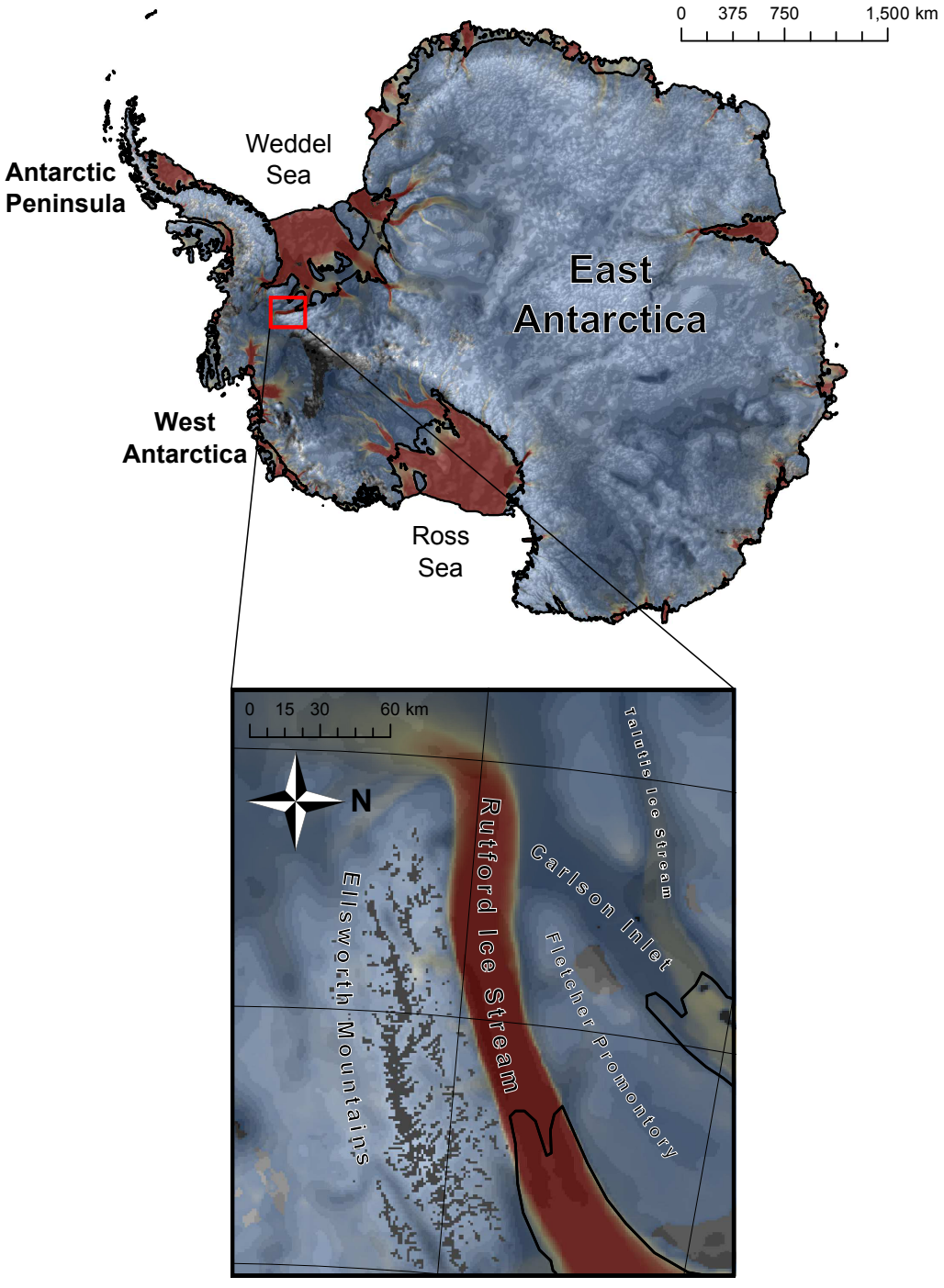

FIGURE 1.4: Surface velocities of the Antarctic ice sheet, derived from satellite measurements [Rignot et al., 2011], along with bed topography and grounding line location from BEDMAP2 [Fretwell et al., 2013]. The inset shows a closer view of the RIS.

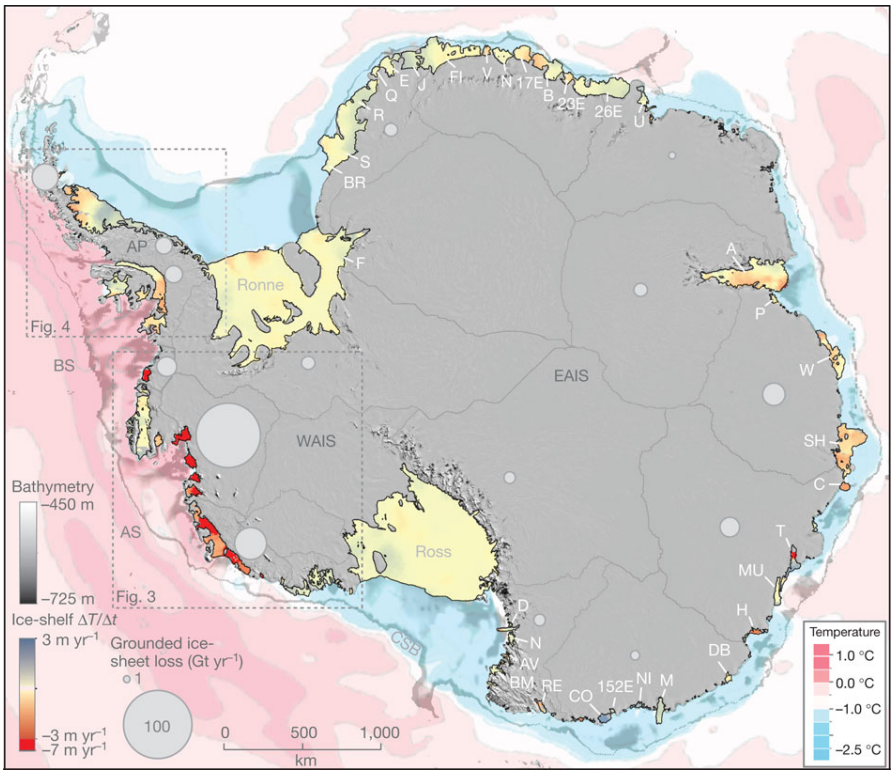

FIGURE 1.5: Antarctic ice-shelf thickness change rate ($\Delta T/\Delta t$) along with bathymetry, potential temperature and grounded ice sheet loss, from Pritchard et al. [2012]

.

Ice streams account for the vast majority of ice discharge from the AIS and therefore understanding how they flow and capturing this in models is of paramount importance. Ice streams are often characterised as either topographic ice streams (constrained by topography) or pure ice streams (bounded by slow moving ice) [Bennett, 2003]. Currently in Antarctica the majority of pure ice streams are found on the Siple Coast and topographic ice streams are more common. Generally they sit in topographic lows as the thicker ice leads to greater basal temperatures and driving stresses which all lead to an increase in velocity. Overall about 90% of all the accumulation on the AIS upstream of grounding lines is discharged through ice streams even though they only form a small proportion of its total area [McIntyre, 1985].

Ice shelves play an equally important role in ice-sheet dynamics through their role in buttressing adjoining ice streams. It was previously thought that ice shelves could be safely ignored in large scale models but the recent collapses of the Larsen

A and B ice shelves showed this was not the case. In both cases the ice streams adjoining the collapsed ice shelves showed dramatic increases in velocity[Rack and Rott, 2004, Rignot et al., 2004, Rott et al., 1996, Scambos et al., 2004] that continue to this day [Berthier et al., 2012, Glasser et al., 2011, Hulbe et al., 2008, Khazendar et al., 2015, Rott et al., 2002, 2011, Shuman et al., 2011, Wuite et al., 2014], suggesting that the ice shelf had been having a considerable buttressing effect. In the case of the collapse of Larsen B, ice-stream velocities increased by up to eightfold following the collapse, with thinning of up to $10\,\mathrm{m\,yr^{-1}}$ [Rignot et al., 2004]. Subsequent modeling work has shown that in general the loss of an adjoining ice shelf will cause a considerable increase in the velocity of any buttressed ice streams, with important implications for global sea levels [Bamber et al., 2007, Dupont and Alley, 2005, 2006, Goldberg et al., 2009, Rott et al., 2011].

Recent warming has lead to intrusion of warm water through deep troughs beneath several Antarctic ice shelves, causing increased basal melting and hence extensive thinning [Pritchard et al., 2012, Rignot et al., 2013, Shepherd et al., 2004]. Figure 1.5 shows the increase in ocean temperatures, particularly in and around the Amundsen Sea, and the accompanying increased loss of grounded ice mass. Clearly the AIS is a highly complex system with many interactions and feedbacks between the ocean, atmosphere, grounded and floating ice and it is in this context that modeling is a valuable tool that can enhance our understanding of the interplay between these many varied processes.

1.2.1 Rutford ice stream

The RIS forms a focus for much of this work and it is worth giving a brief overview of its main characteristics. It is a topographic ice stream, lying in a trough bounded by the Fletcher Promontory on its left flank and the Ellsworth mountains on the right, and drains an area of $49{,}000\,\mathrm{km}^3$ from the WAIS [Doake et al., 2001]. Its width varies between 20-30 km, with a thickness averaging around 2 km and speeds of about $1\,\mathrm{m\,d^{-1}}$ for much of its length, eventually flowing into the Ronne ice shelf

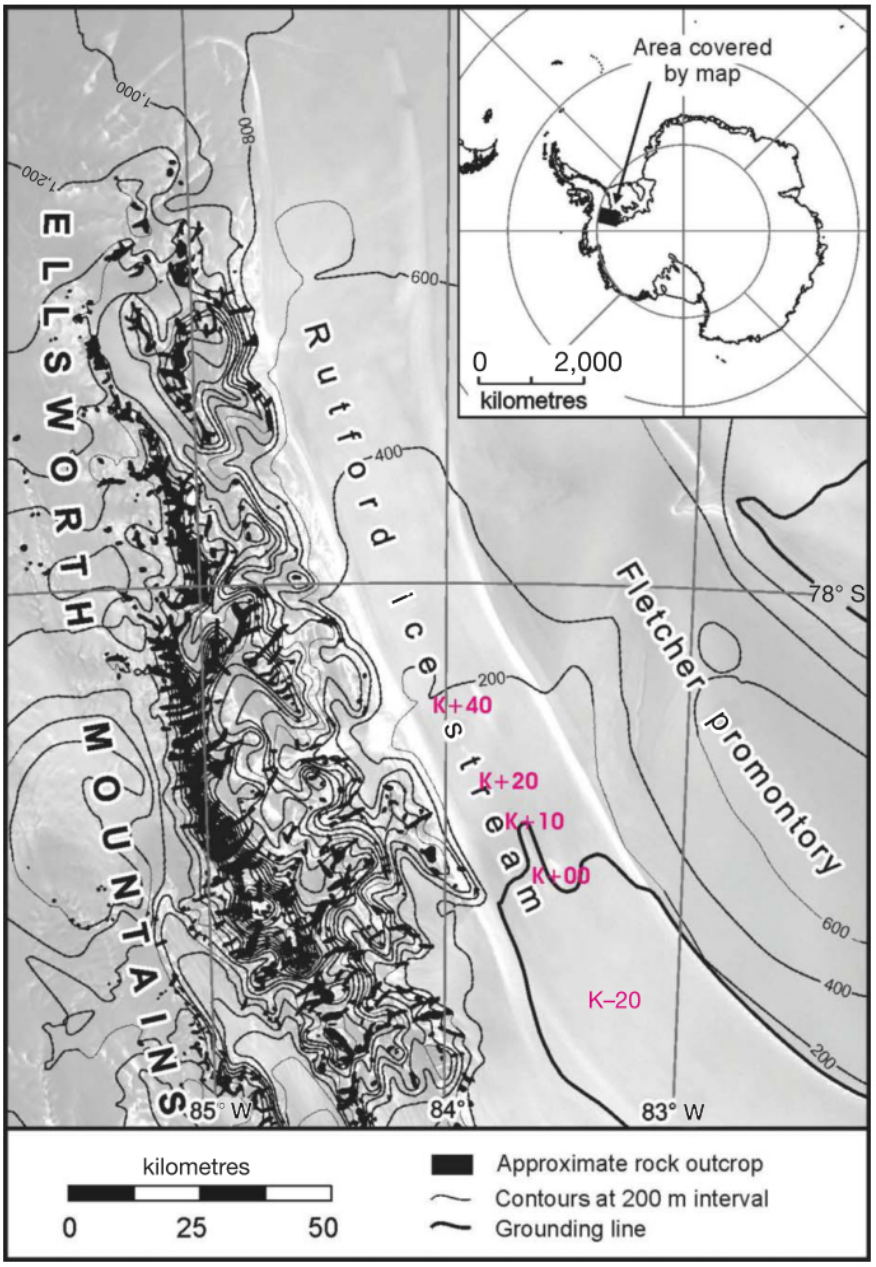

FIGURE 1.6: Map of the RIS from Gudmundsson [2006], with locations of the original GPS sites marked.

(Fig. 1.6). It is a reasonably well studied ice stream with numerous seismic and GPS surveys having been conducted on its surface.

Seismic surveys have revealed the basal regime of the RIS to be complex and spatially variable. Calculation of the acoustic impedance from the reflection coefficient can give information on bed material and reveal that the RIS contains a mix of consolidated sediment and soft deforming till [Smith, 1994, 1997]. A later

survey found changes in this spatial distribution and inferred this as evidence for changes in subglacial hydrology over a timescale of several years [Smith et al., 2007]. Nearer the grounding line the proportion of soft deforming till increases, and the harder sediment is confined to a narrow region in the center of the ice stream [Smith, 1997]. Due to the thickness of the ice these spatial variations in basal properties are not readily visible in spatial variations of surface velocity.

More recent seismic measurements further upstream have produced strong evidence for a canalised drainage system beneath the RIS. King et al. [2004] found areas of very high reflectivity which were indicative of a water layer beneath the ice stream. The authors estimate this covers an area at least 1 km by 0.2 km with an average water layer thickness of less than 1 m. The dimensions suggest a canal rather than a pool of water but it could not be determined whether this was one large canal or many smaller ones.

A subsequent study that combined seismic data with airborne radar data found further evidence for a water layer at the bed, downstream of the previous survey and approximately 50 km upstream from the grounding line [Murray et al., 2008]. Here the features were found to be narrower and the water thickness was estimated at less than 0.2 m. The conclusion was that these were either channelised or canalised hydrological systems but canalised was considered more likely since they occur in a region of deforming till.

1.3 Antarctic tides

Ocean tides form an important boundary condition for ice flow and here I will summarise some of their main general and geographical characteristics. Measurements of the tides beneath a floating ice shelf can be accomplished by satellite altimetry [Fricker and Padman, 2002, Padman et al., 2008], GPS data [King and Aoki, 2003, King et al., 2005] or gravity meters [King et al., 2005, Williams and Robinson, 1980]. Of particular relevance are the two largest ice shelves: the Ross and Filchner–Ronne ice shelves. Conveniently, these two embayments are dominated by

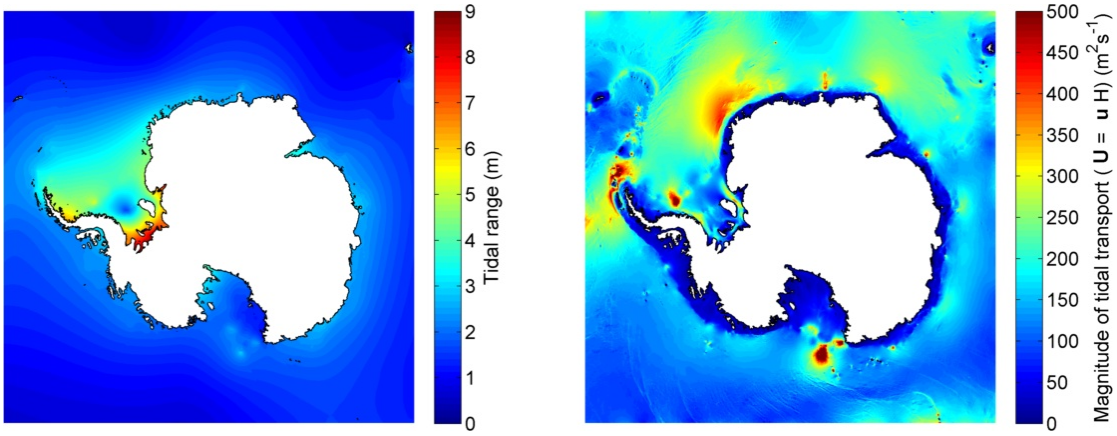

FIGURE 1.7: Tidal range (left panel) and time averaged magnitude of volume transport (right panel) for all tidal constituents in the CATS2008 model (M_2, S_2, N_2, K_2, K_1, O_1, P_1, Q_1, M_f, M_m).

different tidal constituents allowing us to see how the ice response changes with different forcing periods. The Weddell Sea tides are largely semi-diurnal with the M_2 and S_2 tidal constituents dominating and leading to a tidal range of up to 7 m [King et al., 2011, Robertston et al., 1998]. Conversely, the Ross Sea is dominated by O_1 and K_1 tides with a smaller maximum peak-to-peak amplitude of 3 m and causing currents in excess of $1\,\mathrm{m\,s^{-1}}$ [Padman et al., 2002]. An overview of the main tidal constituents considered in this thesis is given in Table 4.1.

Tidal range around Antarctica (calculated as the sum of all tidal constituents in the CATS2008 model) is plotted in Fig. 1.7 (left panel). This clearly shows that the largest tides can be found in the Weddel Sea and Larsen ice shelf regions. The right panel of Figure 1.7 shows the magnitude of volume transport from the same model and constituents. This is calculated as the sum of the magnitude of the velocity vectors for all tidal constituents multiplied by the water depth and provides a convenient measure of tidal currents in the area. Much of the currents are found on the continental shelf away from ice shelves, however tidal currents penetrate beneath the FRIS, entering the basin east of Berkner Island and traveling around the amphidromic point to exit on the west coast.

A more detailed map of the principal diurnal and semidiurnal tidal constituents

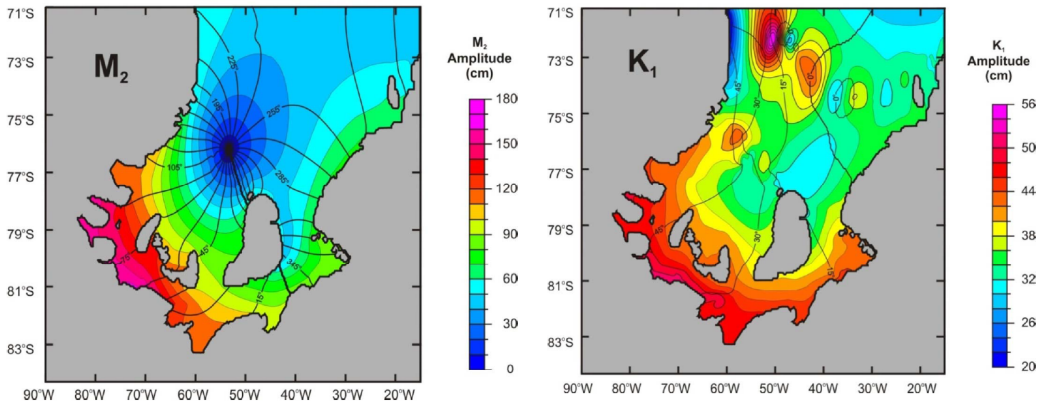

FIGURE 1.8: Tidal amplitude and phase for the M_2 and K_1 tides in the Weddel Sea region [Makinson et al., 2012].

of the Weddel Sea region is shown in Fig. 1.8 [Makinson et al., 2012]. The amphidromic point that dominates semidiurnal tides in this area is situated just offshore from the FRIS calving front and its position is crucial to tidal range along the coast. Spatial variation of the diurnal K_1 tide is less structured but shows a general increase in amplitude towards the most southerly end of the FRIS.

1.4 Ice and tide interaction

Since the discovery of tidal effects on ice streams [Anandakrishnan and Alley, 1997, Anandakrishnan et al., 2003, Bindschadler et al., 2003a,b, Engelhardt and Kamb, 1998, Harrison, 1993] the interpretation and understanding of the mechanisms and impacts has continued to develop. Initial measurements of tidal forcing on ice were limited to the surface of the ice shelves [Williams and Robinson, 1980] and the hinging zone where ice flexure occurs, near the grounding line [Doake et al., 1987, Smith, 1991]. In these regions tidal effects have often been simply described with analytical solutions and elastic beam theory [Holdsworth, 1969, 1977, Reeh et al., 2003]. Measurements made by Anandakrishnan and Alley [1997] on the Kamb Ice Stream first showed that these effects were not limited to regions within a few ice thicknesses of the ocean boundary but could be transmitted far upstream.

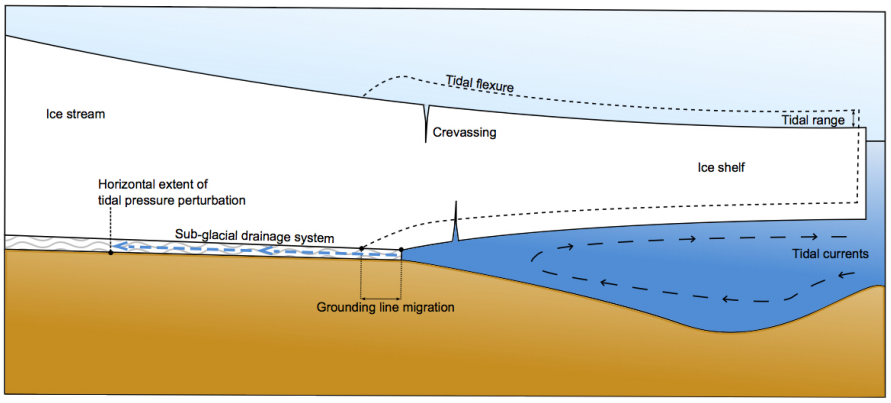

FIGURE 1.9: Schematic showing the various mechanisms by which tides can influence ice-stream flow

Aside from mechanical effects, tides have been shown to play a significant role in vertical mixing beneath ice shelves [Makinson et al., 2011, Mueller et al., 2012]. A model of melting/refreezing processes beneath the Ronne-Filchner ice shelf failed to match observations until tidal mixing was included, at which point both processes increased considerably and the model closely agreed with data [Makinson et al., 2011]. This is not only important in the context of the overall ice-shelf stability, but also plays a role in deep-water formation with far reaching consequences for global heat transport. An overview of the main tidal interactions with ice streams and ice shelves is presented schematically in Fig. 1.9.

1.4.1 Tidal effects on ice flow

The realisation that horizontal ice stream velocities could be modulated by the tides far upstream of the grounding line came relatively recently. Much of the initial work focused on the Whillans Ice Stream (WIS) which was shown to exhibit a stick-slip behaviour resulting from vertical ocean tides [Bindschadler et al., 2003a,b, Sergienko et al., 2009, Wiens et al., 2008, Winberry et al., 2009]. This ice stream has mean annual speeds of greater than $300\,\mathrm{m\,a^{-1}}$ but the majority of motion occurs in brief bursts over time scales less than 1 hour followed by longer periods where the ice is almost stationary. The Whillans Ice Plain portion of the WIS is dominated by stick-slip motion and the initiation of slip events strongly

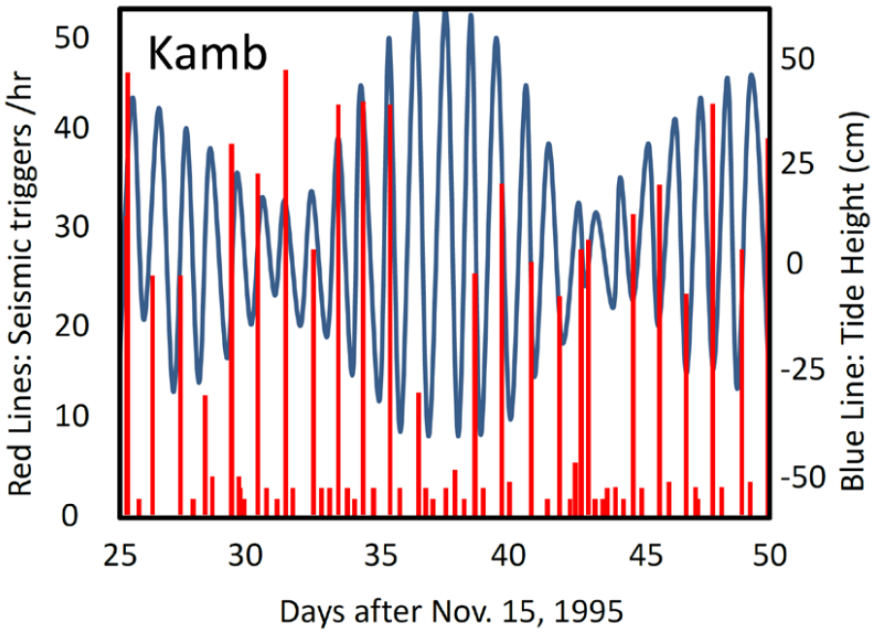

FIGURE 1.10: Seismicity as measured on Kamb Ice Stream 10 km upstream from the grounding line. Red lines show number of seismics events per hour and the tidal height from a tide meter is shown in blue. Reproduced from Thompson [2013], original data published by Anandakrishnan and Alley [1997].

correlates with tides in the Ross sea as accumulated stress is released [Bindschadler et al., 2003a,b].

The first and most intriguing observation that hinted at tidal effects on ice-stream flow was made through measurements of seismicity on the WIS. A station 300 km upstream from the grounding line showed variations in borehole strain at a diurnal frequency and the authors suggested tides as one possible cause [Harrison, 1993]. Both the authors themselves and subsequent studies have treated this with some scepticism and no other obvservations exist that show a tidal signal so far inland, however the possibility remains that this signal could be transmitted through a subglacial drainage system.

Seismicity has also been used on Kamb Ice Stream by Anandakrishnan and Alley [1997], where variation in seismicity at the diurnal tidal period was detectable 85 km upstream from the grounding line. A reproduction of the data from 10 km upstream is shown in Fig. 1.10 and shows strong correlation between the diurnal

tidal signal and the frequency of seismic events, although no apparent correlation related to the spring/neap cycle. Of particular note is the authors' conclusion that the tidal signal must be transmitted through the ice itself rather than through a subglacial drainage system. The main justification for this is an absence of subglacial water largely because water inland of the location of interest is diverted to the WIS and never reaches further downstream. While it appears unlikely that subglacial hydrology plays a role in the transmission of these signals, it is more likely that stress is transmitted through the till due to bending rather than through the ice itself.

More recently, GPS measurements have largely taken over as the largest source of data for tidal modulation of ice-stream flow. When presenting these results it is common to present them in a detrended form, such that the mean velocity signal is removed and only perturbations are shown, and all plots hereafter will follow this convention. On Bindschadler Ice Stream a variation in velocity that is clearly of tidal origin was first observed by Anandakrishnan et al. [2003]. Once again this tidal signal is transmitted far upstream and can be readily observed at a GPS station 80 km upstream from the grounding line (Fig. 1.11).

A common measurement that has been made on various ice streams is the phase lag in the tidal signal upstream from the grounding line. This is commonly defined as the change in phase of detrended horizontal ice motion relative to the vertical ocean tide at the grounding line. Information of this kind can be used to glean information on rheological properties of the ice. The phase shift as measured on Bindschadler Ice Stream corresponds to a phase speed of $5.6\,\mathrm{m\,s^{-1}}$ [Anandakrishnan et al., 2003], compared with a phase speed of $1.6\,\mathrm{m\,s^{-1}}$ on Kamb Ice Stream [Anandakrishnan and Alley, 1997]. On the RIS Aðalgeirsdóttir et al. [2008] gave an estimated phase velocity of $10 \pm 4\,\mathrm{m\,s^{-1}}$ based on two sites 3 km apart, however data analysed in Gudmundsson [2011] suggests a much lower speed of between 0.2 and $1\,\mathrm{m\,s^{-1}}$. In reality, as a result of the viscoelastic nature of ice at tidal timescales, the phase speed depends strongly on the frequency of the signal being considered as will be discussed in detail later.

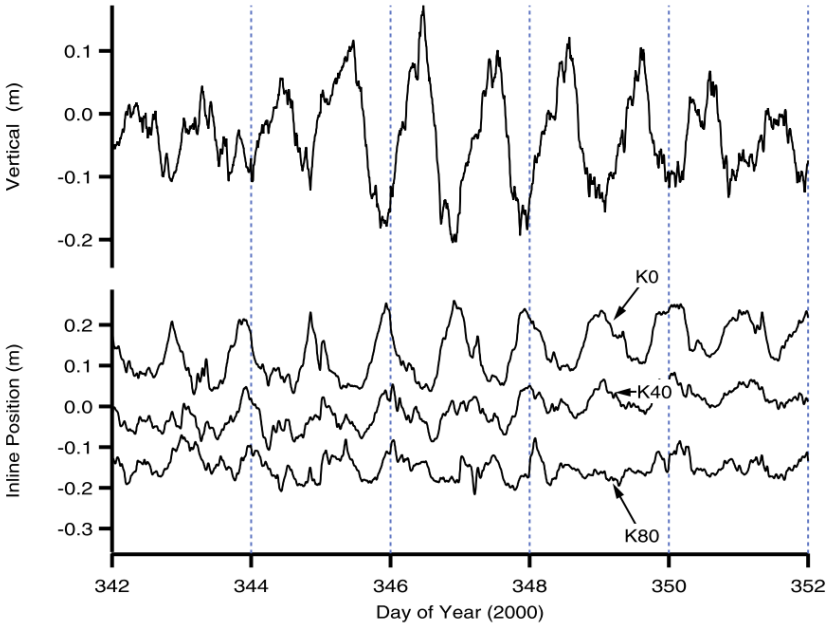

FIGURE 1.11: GPS measurements of vertical position and detrended inline positions at the grounding line (K0), 40 km upstream (K40) and 80 km upstream (K80) on Bindschadler Ice Stream Anandakrishnan et al. [2003].

Recent observations have shown that ice streams can exhibit a long period M_{sf} response to a short period tidal forcing at both diurnal and semi-diurnal frequencies [Gudmundsson, 2006, Marsh et al., 2013, Murray et al., 2007]. Of all the observed tidal effects on ice streams described above, it is arguably the long period modulation in horizontal velocity, often far upstream of the grounding line, which has proven the most challenging to explain as it cannot be described by linear theory and requires a different mechanism. Out of all the frequencies in the observed RIS response upstream of the grounding line, the M_{sf} is by far the largest, dwarfing both the semidiurnal and diurnal signals.

One of the first attempts to explain the fortnightly variations in flow speed at M_{sf} frequency observed on the Rutford Ice Stream was by Gudmundsson [2006, 2007] who suggested that they arise due to the nonlinear relationship between basal motion and basal shear stress. As an adjoining ice shelf rises and falls in phase with the local tide, there is a corresponding increase in tangential basal traction at low tide and a decrease at high tide. If it is assumed that the sliding law is nonlinear, an increase in basal traction leads to a larger increase in basal motion

than an equal and opposite decrease in basal traction. As a result of this imbalance over one tidal cycle there is a net forward motion and over several tidal cycles the variation in tidal range leads to long period modulation of flow speeds. During a spring tide this velocity variation will be greatest and thus the ice stream will flow faster than during a neap tide, leading to a long period modulation in ice stream velocity at M_{sf} frequency driven by a tidal forcing at semi-diurnal frequency.

Murray et al. [2007] put forward a number of possible mechanisms, including Gudmundsson's model described above. They conclude that Gudmundsson's proposal cannot satisfactorily explain observations and a combination of processes are responsible. A partial ungrounding of the ice shelf from pinning points at high tides acts to increase velocity due to reduced basal resistive stress which is counteracted by increased back-stress exerted by the lifted ice shelf [Heinert and Riedel, 2007] leading to a complex relationship between tidal range and horizontal velocities at different frequencies. The authors argue that none of the current theories can completely reproduce the difference in response between the solstice and equinox, whereby the ice stream flows fastest during the equinox when there are two large tides per day and slowest during the solstice when one of these tides is smaller. Subsequent work by King et al. [2010], using the same dataset, however showed that in fact the model presented by Gudmundsson [2007] could explain these observations using a simple stress perturbation model and was consistent with a nonlinear sliding law with $m = 3$ (the stress exponent m is introduced in detail in section 2.4).

A study by Doake et al. [2002] of the Brunt Ice Shelf has also been cited to explain tidal response in ice streams [Aðalgeirsdóttir et al., 2008, Murray et al., 2007]. Variations in basal friction from sub-ice ocean currents driven by the tides was proposed as a mechanism to induce lateral movement of the Ice Shelf at tidal frequencies and it was inferred that these motions would pull or push against the adjacent ice streams, thereby causing variations in horizontal velocities at the same frequency. Although this explanation for the motion of ice shelves has since been discounted [Makinson et al., 2012], the back stress arising from these motions will

still affect the ice streams, but this cannot explain longer period frequencies which are not large in the ice shelf.

Another theory suggested by Aðalgeirsdóttir et al. [2008] is that basal melting near the grounding line, affecting subglacial pressure, might lead to some ice stream modulation at tidal frequencies as warmer water is transported to the grounding line by tidal currents. This idea seems unlikely to have any measurable impact on ice stream velocity however considering the typical magnitude of melting at daily or fortnightly time scales.

Gudmundsson [2007] first proposed the link to a nonlinear basal sliding law and initial modelling efforts confirmed that a simple conceptual model including this process with $m = 3$ in the sliding law could produce the observed fortnightly variations in horizontal velocity. An extension of this work, in which ice was modelled as a non-linear visco-elastic medium and including all components of the equilibrium equation, further strengthened the argument [Gudmundsson, 2011]. Work by King et al. [2011] showed that the same mechanism can reproduce ice stream velocity fluctuations from 4 hours to 183 days observed in longer data series. A modeling study of the Bindschadler Ice Stream, forced primarily by diurnal rather than semidiurnal tidal constituents, further confirmed that a stress exponent $m > 1$ is needed but found that a value of 15 provided a better fit to the observed velocities [Walker et al., 2012]. Some of the differences may be due to different model assumptions, for example the modeling study by Walker et al. [2012] solved a reduced set of equilibrium equations not including flexure stresses. According to the model by Gudmundsson [2011], flexure stresses can contribute to the tidal modulation in flow.

An additional consequence of this nonlinearity in the ice-stream response to tides is an increase in the mean velocity. Since the velocity variation is highly asymmetric the time-averaged mean flow will be increased for any symmetric periodic perturbation in forcing. Gudmundsson [2011] estimated this would lead to a $\sim$5% increase in mean velocity due to the presence of the tides. This finding leads to an

important additional feedback to be considered when examining tidal interaction with ice shelves and ice streams.

Some ice streams that show very little or no tidal modulation in surface velocities are occasionaly cited as examples where interaction is weak, suggesting different processes are at play. GPS sites closest to the coast at Pine Island Glacier do not show any tidal signal at 55 km upstream from the grounding line [Scott et al., 2009], and on the Ekström ice stream the same is true of GPS measurements made only 1 km upstream [Heinert and Riedel, 2007]. Certainly factors such as ice-stream width, basal conditions and ice thickness must play a role in the transmission of tidal stresses and in some situations this may be limited, but care must always be taken to first consider tidal amplitudes beneath the adjoining ice shelf. In both cases the tidal range is far smaller than in the Weddel Sea or along the Siple coast (Fig. 1.7) and this should always be considered first before making any statements about the lack of tidal interaction in these areas.

1.4.2 Subglacial pressure variations due to tides

Ice-stream velocities are highly dependent on conditions at the bed, in particular the presence of subglacial water can lubricate the bed and promote rapid flow. In some cases even very small changes in subglacial water pressure of a few percent can account for velocity changes of up to 40% [Sugiyama et al., 2011]. Due to the difficulty in accessing the bed of thick Antarctic ice streams much of the work in this area has focused on glaciers outside of the Antarctic. As a result of the large amounts of surface melt in the summer the subglacial pressure variations in these regions tend to be dominated by diurnal changes in water input to the bed as temperatures fluctuate during the day. In the majority of the AIS the basal water arises from melting at the bed due to the geothermal heat flux.

In a steady state any drainage system will be eventually flow into and be connected to the ocean. Many types of drainage system are known to exist, including R-channels, linked cavities, canals and Darcian porewater flow [Benn and Evans,

2010]. The level of connectivity to the ocean will depend on the subglacial hydrology, but it is expected that in places with large tidal ranges, the change in water pressure at the grounding line may be transmitted upstream through the drainage system.

Modeling work by Walker et al. [2013] treated ice as a viscoelastic beam supported by an elastic foundation and looked at the resulting effect on subglacial water pressure. The grounding line in this case was not permitted to move but instead acted as a fulcrum and hence as the tide dropped there was a corresponding uplift of the ice stream upstream from this fulcrum, reducing the ice overburden pressure. This mechanism was found in some cases to draw water into the drainage system at low tide and pump water out at high tide. This result is somewhat counterintuitive, since water pressure will rise at high tide and hence it would be expected that this would force seawater upstream into the subglacial drainage system.

1.4.3 Ice flexure and grounding line migration

A final consideration for ice and tide interaction is the migration of ice stream grounding lines due to the ocean tide. Given sufficient tidal amplitude and assuming low effective pressure in the region of the grounding line (note that by definition the effective pressure is zero at the grounding line, see Sec. 2.4), a rising tide will cause the portion of floating ice to increase and the grounding line to retreat and visa versa for a decreasing tide. This process causes a region of ice, known as the grounding zone, to flex in response to the periodic rise and fall of sea level with the tide. The schematic in Fig. 1.12 shows how an ice shelf transitions from free-floating (downstream of point H), through an inflexion point (I), to the grounding line itself where the ice stream detaches from the bed (point G) and finally the upstream limit of flexure (point F). The grounding zone is commonly defined as the region between the hydrostatic limit and the upstream limit of flexure (between points F and H).

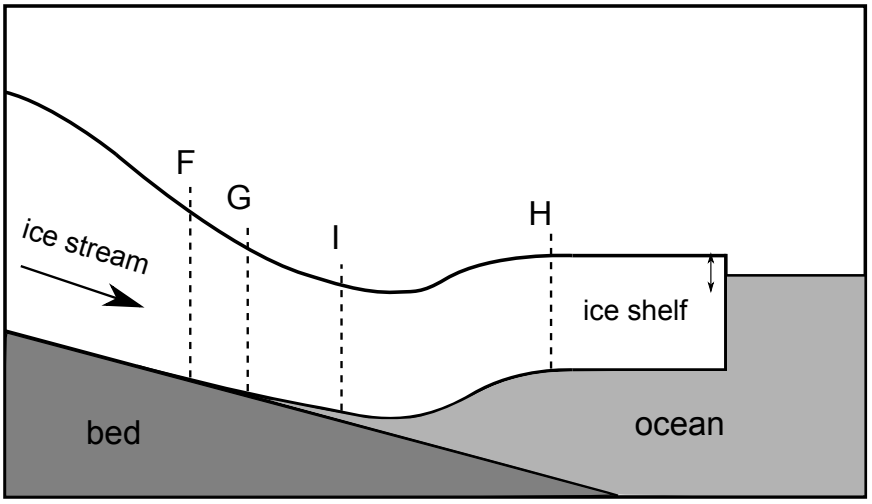

FIGURE 1.12: Schematic showing an ice stream grounding zone, adapted from Fricker and Padman [2006]. H is the hydrostatic limit, I is the inflexion point where bending stresses cause ice to be depressed relative to the hydrostatic level, G is the floatation point and F is the upstream limit of ice flexure. All of these points move with the tide and the grounding zone is defined as the region between H and F.

The extent of this flexural region can be measured by Interferometric Synthetic Aperture Radar (InSAR), altimetry and tiltmeters. Typical the upwards limit of flexure (point F) has been found to extend between 5 and 10 km upstream from the grounding line (point G). Several grounding zone studies exist that look specifically at the RIS. A tiltmeter survey by Stephenson [1984] found the hydrostatic limit (point H) at between 1 and 2 km downstream of the grounding line and the upwards limit approximately 5 km upstream. Rignot [1998] undertook a study of the RIS and Carlson inlet grounding zones using InSAR with the aim of detecting possible changes in mass balance and no significant changes could be found, with a suggestion of a slightly positive mass budget.

Repeat track laser altimetry was first used by Gray et al. [2002] to detect the grounding zone extent. The Ice, Cloud and land Elevation Satellite (ICESat) mission has spawned many similar studies, first mapping the grounding zone of the Institute Ice Stream [Fricker and Padman, 2006], followed by the Amery [Fricker et al., 2009], Ross [Brunt et al., 2010] and Filchner-Ronne ice shelves [Brunt et al., 2011].

Tidal flexure has also been used extensively to provide an estimate of the rheological properties of ice. Studies measure the flexural profile and attempt to infer the rheological model parameters needed to match a given profile. Both purely elastic [Holdsworth, 1969, 1977, Lingle et al., 1981, Stephenson, 1984, Vaughan, 1995] and linear viscoelastic [Marsh et al., 2014, Reeh et al., 2003] models typically suggest rheological properties that differ considerably from laboratory experiments of the propogation of sound waves through ice (e.g. Schulson and Duval 2009).

An assumption is often made that ice immediately downstream of the grounding line is in hydrostatic equilibrium and for the shallow shelf approximation (SSA) this is true. In the full-Stokes (FS) case however this does not hold, and the grounding line is located upstream from its expected location if hydrostatic equilibrium is assumed [Gudmundsson et al., 2012, Pattyn et al., 2013, Tsai and Gudmundsson, 2015].

Several approaches other than the hydrostatic assumption have been used to deal with tidally induced grounding line migration. Sayag and Worster [2011, 2013] use an elastic beam model sitting on a deformable bed to investigate grounding line migration, elastic properties of ice and subglacial hydrology. In their model they find that elastic pressures in the hinge zone can be a barrier to water flow through the drainage system and may act as a control on water intrusion beneath an ice stream. Due to the uncertainties in bed geometry the model required multiple fitting parameters in order to match the observed flexural profile, however this means the resulting calculated migration may not be realistic [Tsai and Gudmundsson, 2015].

A previously overlooked aspect of grounding line migration, shown analytically in Tsai and Gudmundsson [2015], is that for typical ice-sheet geometries the upstream and downstream components of migration are not equal. This asymmetry arises because downstream of the grounding line the upwards slope of the ice base is related to the surface slope whereas upstream it is not. This may lead to upstream migration almost an order of magnitude greater than downstream [Tsai and Gudmundsson, 2015].

A new approach, proposed by Tsai and Gudmundsson [2015], is to treat grounding line migration as a fracture problem. The crack can be thought of as the ice-bed/ice-ocean interface and the grounding line as the crack tip. Thus the grounding line moves back and forth as the crack opens and closes. In this case the migration is even more asymmetric than the hydrostatic case would suggest due to a nonlinearity in the equations relating pressure forcing and crack growth. This novel approach is used to make new estimates of bed slopes in grounding zones which differ considerably from previous studies. Most importantly, where symmetrical migration has been assumed the true mean grounding line position is incorrect, with implications for mass balance estimates highly sensitive to the grounding line position (eg. Shepherd et al. 2012).

1.5 Aims of this thesis

In this chapter the importance of tide and ice interaction has been explained. The mechanisms considered are numerous and cannot all be explored since the necessary fully coupled model does not exist. Instead I will focus on three main research questions.

1. What is the source of nonlinearity observed on the RIS and other ice streams which leads to long-period modulation of their velocity?

2. What inferences can we make about the basal sliding law and characteristics of the RIS from attempting to match the M_{sf} effect?

3. How might changes in ice-shelf geometry cause changes in the ocean tide, possibly setting up feedbacks between the two?

1.6 Thesis structure

- **Chapter 2** - As a first step I introduce the governing equations for ice-stream and ice-shelf flow, including visco-elastic rheology, the basal sliding law and grounding line migration due to tides.

- **Chapter 3** - I present the finite element model MSC.Marc which is used for all ISS simulations. I outline the governing equations, the various domains and boundary conditions, along with a description of the subglacial hydrological model and inversion procedure used in a later results chapter.

- **Chapter 4** - Here I present a general mathematical background for ocean tides, introducing the equilibrium tide, dynamical tidal theory and shallow water equations. I then describe the OTIS and CATS2008 tidal models which I make use of in this thesis.

- **Chapter 5** - In this chapter I show results from a simple 3D ISS model that is an extension of previous work investigating the long period response of ice-stream flow to tidal forcing. This shows for the first time that a nonlinear sliding law can reproduce observed long period modulation of ice-stream flow when lateral effects are included. I also derive an expression for stress-coupling length scales of an ice stream based on the SSA.

- **Chapter 6** - This chapter presents results from a more advanced version of the ISS model in the previous chapter, attempting to match observations made on the RIS using a coupled hydrological model and formal inversion. The modelling work clearly shows that hydrology must play a role in producing the tidal signal and helps constrain the type of drainage system that must exist beneath the RIS, something that no other modelling technique has been able to do.

- **Chapter 7** - Here I show results from 2D models that investigate grounding line migration due to tides, both in terms of the expected migration asymmetry and the effect on the M_{sf} response. This type of contact simulation has not been attempted before in the context of grounding line position.

The model reproduces asymmetry predicted by theory and the effect is to increase the M_{sf} response of the ice stream to ocean tides.

- **Chapter 8** - This chapter investigates possible changes in tidal forcing resulting from perturbations in ice-shelf geometry, both in terms of the tidal amplitude and dissipation. The result of this work is to show that tides would change considerably in the Weddel Sea region if the ice shelf were to reduce in extent or thickness.

- **Chapter 9** - Finally, I summarise the model results presented in this thesis and suggest possible future work, including both model development and observational work.

Chapter 2

Mathematical Background

This chapter will present the relevant governing equations for ice flow. Since ice is a shear thinning non-newtonian fluid, the apparent viscosity decreases with increased stress, leading to considerable differences in how it is modelled compared to the ocean. Throughout this section the cartesian coordinate system is used, with the convention that x represents the downstream component, y is the across flow component and z is the vertical component and the accompanying components of the velocity vector $\mathbf{u}$ (u_i) are denoted u, v and w respectively. I use a comma to denote partial derivatives, dot notation for time derivatives and the summation convention, in line with notation commonly used in continuum mechanics. Geometrical entities of an ice stream are as follows: h is ice thickness, d is ice draft, f is ice freeboard, b is the basal ice profile, B is the bed profile, S is sea level, α is ice surface slope and β is bed slope. These are defined schematically in Fig. 2.1.

I use capital delta (Δ) to denote perturbations in a parameter and an overbar accent ($\bar{}$) to denote time mean values.

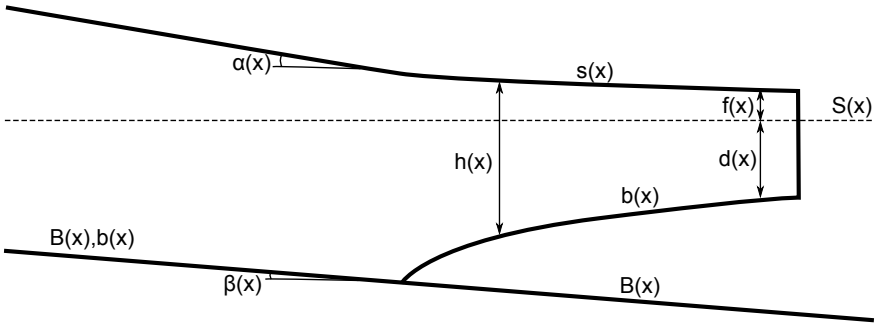

FIGURE 2.1: Schematic showing the defintions used in this thesis for various geometrical entities

2.1 Stress and Strain

Modeling of ice motion is generally expressed in terms of stresses (σ) and strains (ϵ). Stress and strain are second order symmetric tensors, such that $\sigma_{ij} = \sigma_{ji}$, $\epsilon_{ij} = \epsilon_{ji}$ and stress can be written out in full as

$$\boldsymbol{\sigma} = \begin{bmatrix} \sigma_{xx} & \sigma_{xy} & \sigma_{xz} \\ \sigma_{xy} & \sigma_{yy} & \sigma_{yz} \\ \sigma_{xz} & \sigma_{yz} & \sigma_{zz} \end{bmatrix}. \tag{2.1}$$

Stresses are resolved in a particular orientation with the aid of unit vectors. Here I define $\hat{\mathbf{n}}$ as a unit vector normal to a surface and $\hat{\mathbf{t}}$ as a unit vector perpendicular to $\hat{\mathbf{n}}$. Normal stress $\sigma_n = \hat{\mathbf{n}}^T \cdot \boldsymbol{\sigma} \cdot \hat{\mathbf{n}}$ and shear stress $\sigma_t = \hat{\mathbf{t}}^T \cdot \boldsymbol{\sigma} \cdot \hat{\mathbf{t}}$ are scalars giving the stress along a particular orientation. If $\sigma_n > 0$ the normal stress is considered tensile and if $\sigma_n < 0$ it is compressive.

As a second order tensor, $\boldsymbol{\sigma}$ has 3 invariants; quantities that are independant of the orientation of the coordinate axes. The first of these invariants, commonly known as the mean stress, is defined as:

$$I_1 = \mathrm{tr}(\boldsymbol{\sigma}) = \sigma_{kk}. \tag{2.2}$$

Directly related to this is the pressure $p = -(1/3)\sigma_{kk}$, the negative of the average of the three normal stress components of the stress tensor. It is often useful to only consider the part of the stress tensor that does not include 'mean pressure'. The

deviatoric stress (denoted $\boldsymbol{\tau}$) is what is left after adding the hydrostatic pressure to the stress tensor, ie.

$$\tau_{ij} = \sigma_{ij} - \frac{1}{3}\delta_{ij}\sigma_{kk}, \tag{2.3}$$

where δ_{ij} is the Kronecker delta symbol which is equal to one if i and j have the same value and zero otherwise, ie. $\delta_{ij} = I$. Similarly, deviatoric strains (e) are defined as

$$e_{ij} = \epsilon_{ij} - \frac{1}{3}\delta_{ij}\epsilon_{kk}. \tag{2.4}$$

Written out in full, the deviatoric stress tensor is given by:

$$\begin{bmatrix} \tau_{xx} & \tau_{xy} & \tau_{xz} \\ \tau_{xy} & \tau_{yy} & \tau_{yz} \\ \tau_{xz} & \tau_{yz} & \tau_{zz} \end{bmatrix} = \begin{bmatrix} \sigma_{xx} + P & \sigma_{xy} & \sigma_{xz} \\ \sigma_{xy} & \sigma_{yy} + P & \sigma_{yz} \\ \sigma_{xz} & \sigma_{yz} & \sigma_{zz} + P \end{bmatrix}. \tag{2.5}$$

The negative of the hydrostatic stress can be thought of as a 'mean pressure' at any given point in the ice stream, this acts to change the volume of the body if it is compressible. The deviatoric stress causes distortion and it is often a convenient way to express stress in an ice stream.

The second invariant, often defined in terms of deviatoric stresses as:

$$I_2 = \sqrt{(\tau_{ij}\tau_{ji})/2} \tag{2.6}$$

is another useful quantity in glaciology, related to the Von Mises stress, that will be discussed in more detail later. The third invariant is

$$I_3 = \det(\boldsymbol{\tau}) = \varepsilon_{ijk}\tau_{ij}\tau_{jk}\tau_{ki} \tag{2.7}$$

but is less commonly used that the first two. Here ε_{ijk} is the alternating unit tensor which equals zero if any two indices are equal, unity when the indices appear in order and negative unity if they do not.

It is sometimes convenient to express strain rate in terms of the velocity vector u_i. Assuming that the first derivative of this term is small and hence any products

of these derivatives are completely negligible leads to the infinitesimal strain rate tensor, expressed in tensor notation as

$$\dot{\epsilon}_{ij} = \frac{1}{2}\left(\frac{\partial u_i}{\partial x_j} + \frac{\partial u_j}{\partial x_i}\right), \tag{2.8}$$

which for the diagonal components simplifies to $\dot{\epsilon}_{kk} = \partial_{x_i} u_i$.

2.2 Glacier flow

Since acceleration terms are considered negligible, a glacier can be considered effectively in a stress equilibrium, meaning the sum of all forces acting on it will balance. Gravity drives a glacier downwards and this force, known as the driving stress, can be written as

$$\tau_d = \rho g h \sin(\alpha), \tag{2.9}$$

assuming the bed is flat ($\beta = 0$). Typically the largest force to balance this is the basal drag, denoted τ_b. Basal drag plays a crucial role in moderating ice-stream flow; relating the two remains a problem in glaciology and is discussed more in Section 2.4. Other resistive forces such as sidewall drag (τ_w) and longitudinal drag (τ_L) also play a role, such that

$$\tau_d = \tau_b + \tau_L + \tau_w. \tag{2.10}$$

Solving for glacier flow requires a set of field equations commonly referred to as the conservation of mass and linear momentum. If a material is compressible with a density ρ then the conservation of mass can be written as

$$\frac{\partial \rho}{\partial t} + \nabla \cdot (\rho\, \mathbf{u}). \tag{2.11}$$

This can be simplified considerably by assuming that density is both homogeneous ($\partial_{x_i} \rho = 0$) and does not vary with time ($\partial_t \rho = 0$), so that Eq. (2.11) becomes simply $\nabla \cdot \mathbf{u} = 0$.

Neglecting acceleration terms results in a set of equilibrium equations which simply state, from Newton's second law of motion, that the sum of all forces acting on a body must balance. Written out in full for the sake of clarity, and expressed in terms of deviatoric stresses, this gives the following set of equations:

$$\partial_x \tau_{xx} + \partial_y \tau_{xy} + \partial_z \tau_{xz} = \partial_x p \tag{2.12a}$$

$$\partial_x \tau_{xy} + \partial_y \tau_{yy} + \partial_z \tau_{yz} = \partial_y p \tag{2.12b}$$

$$\partial_x \tau_{xz} + \partial_y \tau_{yz} + \partial_z \tau_{zz} = \partial_z p + \rho_i g, \tag{2.12c}$$

where g is gravitational acceleration ($9.81\,\mathrm{m\,s^{-2}}$), p is pressure, ρ_i is ice density and assuming that gravity is the only body force. This type of motion where acceleration terms are assumed to be negligible is known as Stokes flow and this set of equations describe the conservation of linear momentum.

A commonly used approximation in ice-sheet modeling, known as the shallow-shelf approximation (SSA) or occasionally the shallow ice stream approximation, neglects the first two terms on the left hand side (LHS) of Eq. 2.12c. This has been derived a number of times in different forms and with different approaches, e.g. MacAyeal [1989], Morland [1984], and Muszynski and Birchfield [1987]. Some of the key features of the SSA are that vertical stresses are lithostatic ($\sigma_{zz} = -\rho_i g(s - z)$) and the slip ratio c_d, such that the SSA in 1-D gives

$$4\partial_x(h\eta\partial_x u) - \tau_b = \rho_i g h \sin\alpha, \tag{2.13}$$

where η is effective viscosity (Eq. 2.20) and τ_b is the basal drag (Eq. 2.23). This relates the longitudinal and basal resistive stresses (LHS) to the driving stress (RHS).

2.3 Ice rheology

Ice streams flow as the result of three mechanisms; deformation of ice, deformation of the substrate beneath the ice and sliding over the bed material. Of these the

latter two are often considered together as a basal slip term (Sec. 2.4). Internal deformation of ice, or 'creep', arises as a result of movement of individual ice crystals. The most commonly used flow law that relates creep flow to stresses within ice is known as Glen's law [Glen, 1955] and can be written as

$$\dot{e}_{ij} = A\tau_{ij}^{n} \tag{2.14}$$

where $\dot{e}_{ij}$ is the deviatoric strain rate, A is the rate factor and n is a constant. The value of n is generally taken from borehole tilt and labortatory experiments to be $\sim$3 [Benn and Evans, 2010, Cuffey and Patterson, 2010]. While there is no real justification for using this exact value the relationship is certainly nonlinear and so I use this value throughout unless explicitly stated otherwise in the text. A large number of different expressions for A have been used and there is no clear consensus on which is best. In this thesis I use the temperature relation derived by Smith [1981] by fitting to data from Mellor and Testa [1969]:

$$A = \alpha_1 e^{\beta_1 \tilde{T}} + \alpha_2 e^{\beta_2 \tilde{T}}, \tag{2.15}$$

where α_1, α_2, β_1 and β_2 are fitting parameters and $\tilde{T} = T + 273.15$ is the temperature relative to melting point at zero pressure ($\tilde{T}$ in degrees Kelvin). There is evidence that A can be dependant on ice density, water content, grain size and hydrostatic pressure [Cuffey and Patterson, 2010] however the strongest dependance is on temperature and I choose to only include this effect for the sake of simplicity.

The relation given in Eq. 2.14 is only valid for simple cases considering only a single component of the stress tensor. For more complex flow as might be expected in a glacier or ice stream a generalisation of Glen's law, commonly known as the Bailey-Norton law, is used. This expresses the relation between stress and strain rate as a function of their invariants such that

$$\dot{e}_{ij} = A\tau_E^{n-1}\tau_{ij}, \tag{2.16}$$

where $\tau_E = I_2 = \sqrt{\tau_{ij}\tau_{ji}/2}$ is the effective stress, the second invariant of the

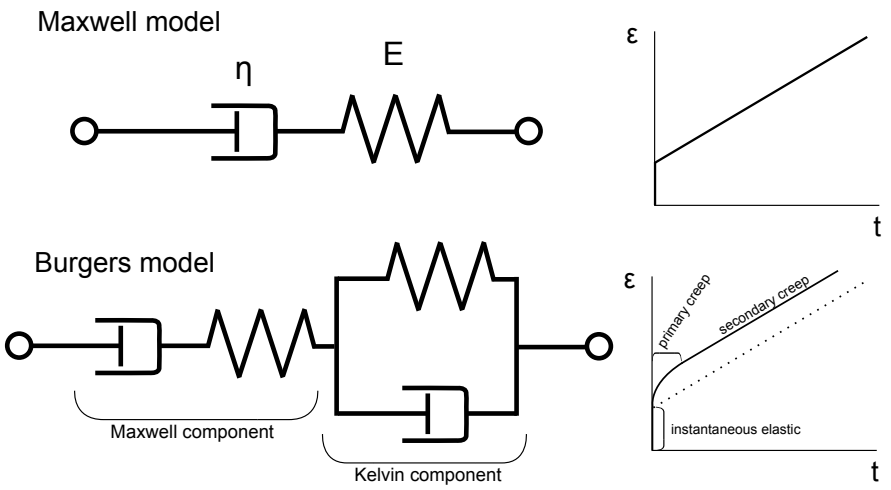

FIGURE 2.2: Diagram comparing arrangement of elastic springs and viscous dashpots for the Maxwell and Burgers rheological models. Alongside are the corresponding strain - time plots showing the response of each model to the application of an instantaneous constant stress.

deviatoric stress tensor [Glen, 1955, Steinemann, 1954, 1958]. A consequence of the assumed nonlinearity of creep flow is that all components of the stress tensor will act to increase a single component of the strain rate. This nonlinearity therefore adds a great deal of complexity to modelling of ice flow. It is worth mentioning that in the equations listed above and in my model I assume ice is isotropic. In reality the orientation of ice fabric will influence deformation as ice preferentially shears along a plane perpendicular to the fabric axis. The system of equations listed above assume that ice is a purely viscous medium. At relevant short timescales ice may behave visco-elastically, resulting in additional elastic terms.

Stress and strain of linear elastic materials are related through Hooke's law by the Young's modulus (E) such that $\sigma = E\epsilon$. The Young's modulus is an important parameter which is a measure of the stiffness of an elastic (or viscoelastic) material. Various models have been employed to describe viscoelastic behaviour of ice. The Maxwell rheological model is the simplest way of relating visco-elastic stresses and strains as an elastic spring and viscous dashpot connected in series (Fig. 2.2). The Kelvin model uses a spring and dashpot in parallel and the Burgers model is a four element model consisting of a Kelvin and Maxwell model connected in series. Laboratory experiments on ice at relevant stresses and temperature demonstrate that its response to a stress consists of an instantaneous elastic strain, a delayed

elastic strain and viscous strain [Glen, 1955]. The Burgers model is the only one of the three aforementioned models to capture all three responses of a viscoelastic material to stress [Shames and Cozzarelli, 1997].

Work by Reeh et al. [2003] investigated the tidal bending of glaciers using the four element Burgers model and derive rheological parameters that match observed flexural profiles. The Burgers model is numerically expensive and therefore a simpler approach is preferential if it does not sacrifice accuracy. In his study of tidal interactions with ice streams, Gudmundsson [2011] showed that primary creep timescale of the Burgers model for standard ice properties was of the order of minutes and the Maxwell model could be made to match the Burgers model exactly at tidal timescales. The resulting material parameters that best matched the model of Reeh et al. [2003] were a Young's modulus of 4.8GPa and a Poisson's ratio (ν) of 0.41.

The viscoelastic rheological model I use is the upper convected Maxwell model, using the justification given by Gudmundsson [2011]. The resulting viscoelastic strain is therefore the sum of the viscous and elastic strains and the total stress equals the stress in each component. Using these relations Eq. 2.16 becomes

$$\dot{e}_{ij} = \frac{\overset{\triangledown}{\tau}_{ij}}{2G} + A\tau_E^{n-1}\tau_{ij}, \tag{2.17}$$

where $\overset{\triangledown}{\tau}$ denotes the upper convected time derivative of deviatoric stress. This upper convected time derivative replaces the partial derivative in simpler Maxwell models to enable calculation of large strain under rotation which, although not essential for the strains presented in this model, I have chosen to use for the sake of completeness.

A useful quantity is the effective Maxwell relaxation time, λ, defined as

$$\lambda = \frac{\eta}{G}, \tag{2.18}$$

where

$$G = \frac{E}{2(1+\nu)}, \tag{2.19}$$

$$\eta = \frac{\boldsymbol{\tau}_E^{1-n}}{2A} \tag{2.20}$$

and ν is Poisson's ratio [Shames and Cozzarelli, 1997]. The relaxation time gives the relative importance of elastic and viscous components of deformation for a given material. Related to this is the Deborah number (De), defined as

$$\mathrm{De} = \frac{\lambda}{T} \tag{2.21}$$

where T is the period of the forcing being applied to the material. If this dimensionless number is large then a material will behave primarily elastically, and if small it will respond primarily viscously. Equation 2.20 gives the definition for effective viscosity and demonstrates that as the effective stress increases the effective viscosity decreases, ie. the ice becomes softer.

For most applications in Antarctic glaciology it is sufficient to treat ice as purely viscous (eg. using a rheology given in Eq. 2.16) because the relaxation time is of the order of a few days and most external forcing such as climate or seasonality has a period of months to years, such that $\mathrm{De} \ll 1$. When considering tidal interactions it is necessary to use the elastic or full viscoelastic rheology for ice given by Eq. 2.17 since the largest tidal constituents have periods less than λ. Note that for $n \neq 1$ (ie. the non-Newtonian case generally used for ice) both λ and η are referred to as effective values because they are dependent on the stress state as shown in Eq. 2.20.

Whether a material is elastic, viscous or viscoelastic also determines the phase lag between an applied stress and resulting strain. For an oscillatory force strain is 90° out of phase with stress for a purely viscous material and exactly in phase for a purely elastic material. A viscoelastic material exhibits a phase lag somewhere between the two, depending on the relaxation timescales described above.

2.4 Basal slip

Quantifying the basal slip term mentioned above remains one of the biggest problems in glaciology and a large variety of different relations are used to parameterise and model the various processes occurring at the ice bed that lead to overall motion [Cuffey and Patterson, 2010]. Overall along-flow velocity (u) of an ice stream is the sum of basal slip (u_b) and the internal ice deformation (u_d). The slip ratio, defined as $c_s = u_b/u_d$, is typically greater than 100 for a large Antarctic ice stream, hence the term u_d is sometimes neglected when considering overall flow velocities of an ice stream but calculating u_b is of crucial importance.

One of the first sliding laws proposed by Weertman [1957] was

$$u_b = c_w \left(\frac{\tau_b^{0.5}}{R_a} \right)^{n+1} \tag{2.22}$$

where c_w is a constant and R_a is spacing of bedrock bumps. More recently it has become common to express basal velocity using in an empirical form that includes the effects of hydrology (e.g. Bindschadler 1983, Budd and Keage 1979):

$$u_b = c\,\tau_b^m\,N^{-q} \tag{2.23}$$

where m and q are constants, c is slipperiness and

$$N = p_i - p_w. \tag{2.24}$$

N, the effective pressure, is the difference between ice overburden pressure (p_i, strictly defined as σ_{nn}) and subglacial water pressure (p_w). A negative value for N implies that the ice is detached from the bed and floating, as is the case downstream of the grounding line on an ice shelf. A commonly used assumption is that

$$p_i = \rho_i\,g\,h, \tag{2.25}$$

however for the FS solution this does not hold and σ_{nn} cannot be simply described

in this way. In the model described later no assumptions are made about p_i, it is not used directly in the equations since I use a mean effective pressure value that is the same everywhere.

The dependancy on N is often not included in models and the sliding velocity becomes a function of basal stress only. In either case, choosing an appropriate value for m remains an open question in glaciology. The sliding law given in Eq. 2.23 forms the basis for much of the work in this thesis as I seek to investigate likely values for the unknowns m and q.

2.5 Grounding line migration

The grounding line is the point at which grounded ice loses contact with the bed and begins to float, with its weight supported by water pressure. The position of the grounding line can move, either due to long term changes in ice thickness and sea level or through periodic changes in sea level as is the case with the ocean tide. In the vast majority of ice sheet models the floating ice is assumed to be in hydrostatic equilibrium such that

$$\rho_i g\, h = \rho_w g\, d. \tag{2.26}$$

In reality this is not the case in the flexural region near the grounding line and in order to accurately estimate the location of the grounding line a full-Stokes model is needed. In spite of this, much can be learnt about the nature of grounding line movement from simple hydrostatic considerations.

The migration of the grounding line ΔL due to a perturbation in sea level ΔS can be written as

$$d_x h\, \rho_i \Delta L = \rho_w \Delta S - \beta \rho_w \Delta L \tag{2.27}$$

where $d_x h$ is the along flow ice thickness gradient [Tsai and Gudmundsson, 2015]. Upstream of the grounding line $d_x h = \alpha - \beta$. Downstream of the grounding line

$$d_x h = \alpha\Big(1 + \frac{\wp}{1-\wp}\Big), \tag{2.28}$$

where $\wp$ is the ratio ρ_i/ρ_w, such that the dependence of the thickness gradient on β drops out and the upwards slope of the ice bed is a function of the surface slope only. This leads to the conclusion, as pointed out in Tsai and Gudmundsson [2015], that unless $d_x h$ is constant across the grounding line the migration of the grounding line will be asymmetric (assuming β is constant in this region). In fact for a typical ice stream constant $d_x h$ is unlikely and so asymmetric grounding line migration due to the tides is expected to be the norm. Tsai and Gudmundsson [2015] propose that this asymmetry could lead to an upstream migration ∼9 times greater than the downstream portion.

A more concise form of Eq. 2.27, $\Delta L = \Delta S/\gamma$, makes use of the parameter γ which for upstream migration is given by

$$\gamma^+ = \beta + \wp\big(\alpha - \beta\big) \tag{2.29}$$

and downstream migration is

$$\gamma^- = \beta + \wp\alpha\big(1 + \frac{\wp}{1-\wp}\big), \tag{2.30}$$

or more concisely:

$$\gamma^- = \beta + \frac{\wp\alpha}{1-\wp}. \tag{2.31}$$

Dividing γ^+ through by $1 - \wp$ gives

$$\frac{\gamma^+}{1-\wp} = \frac{\beta}{1-\wp} + \frac{\wp\alpha}{1-\wp} - \frac{\wp\beta}{1-\wp}, \tag{2.32}$$

and rearranging

$$\frac{\gamma^+}{1-\wp} = \frac{\beta(1-\wp)}{1-\wp} + \frac{\wp\alpha}{1-\wp}, \tag{2.33}$$

thus

$$\frac{\gamma^+}{1-\wp} = \gamma^-, \tag{2.34}$$

which for typical ice density of $920\,\mathrm{kg\,m^{-3}}$ and ocean density of $1030\,\mathrm{kg\,m^{-3}}$ gives the result that γ^- is approximately nine times smaller than γ^+.

The degree of asymmetry, defined here as $\Delta L^+/\Delta L^-$, is given by the ratio γ^-/γ^+ where $+/-$ refers to the upstream or downstream cases respectively. As stated previously, if $d_x h$ is the same either side of the grounding line then γ^+ and γ^- are equal and the migration is symmetrical. Furthermore, whether or not $d_x h$ is constant, if $d_x h << \beta$ the dependency on thickness gradient becomes negligible and the migration will be approximately symmetric and $\Delta L \approx \frac{\Delta S}{\beta}$.

Chapter 3

Model Description

In this chapter I present a description of the ice sheet/shelf (ISS) model that is used in the investigations of ice-stream response to tidal forcing. Results from three distinct ISS models are presented in this thesis. Initial modeling work is limited to qualitative comparison with data and hence uses a less complex setup which does not include basal hydrology (Section 3.4) or a Bayesian inversion (Section 3.7). Investigations of grounding line migration are limited to this earlier version of the model. Any other differences between the two models such as the domains are made clear in the text, otherwise the model description in this chapter refers to all models used. The three distinct models will be referred to as the 2D model (flowline model investigating grounding line migration), the 3D model (simplified 3D model with no inversion of basal hydrology) and the 3D coupled model (including a Bayesian inversion to initialise the model and coupling ice-stream velocity to a subglacial hydrological model). The models presented here seek to include all the processes that might play a role where this is possible, rather than assuming some terms are negligable and can be thrown out.

3.1 MSC.Marc solver

The ISS model is based around a commercial full-Stokes finite element analysis software MSC.Marc [MARC, 2013]. Most of the modeling work was done in 3D, however simulations of a migrating grounding line were limited to a 2D flow-line model due to computational limitations. The field equations are the conservation of mass, linear momentum and angular momentum:

$$\frac{D\rho_i}{Dt} + \rho_i u_{q,q} = 0, \tag{3.1}$$

$$\sigma_{ij,j} + \mathcal{G}_i = 0, \tag{3.2}$$

$$\sigma_{ij} - \sigma_{ji} = 0, \tag{3.3}$$

where D/Dt is the material time derivative (the derivative of a particular particle as it moves through space ie. Lagrangian derivative), u_i are the components of the velocity vector, σ_{ij} are the components of the Cauchy stress tensor and $\mathcal{G}_i$ are the components of the gravity force per volume. Equation (3.2) is identical to the expanded form given in Eq. (2.12) except expressed in terms of stresses.

The rheological model is a Maxwell model as used by Gudmundsson [2011] which has a close agreement to more complex Burgers model at the relevant timescales. A detailed description of the ice rheology can be found in Section 2.3. In all viscoelastic simulations the rate factor was made a function of temperature using the relation in Eq. (2.15). A static temperature distribution was chosen, varying linearly from 0°C at the bed to -25°C at the ice surface.

Changes in ice-stream mass balance through accumulation and ablation are not included in the model due to the short timescales being considered throughout this thesis.

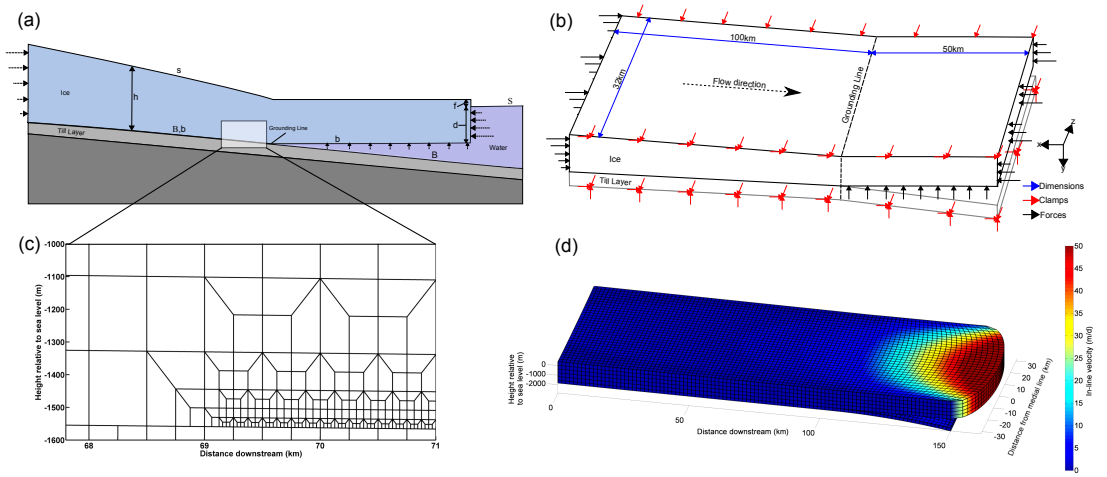

FIGURE 3.1: Model setup for 2D (a,c) and 3D (b,d) simulations Rosier et al. [2014b]. Panels a and b are schematic representations of the model domains while panels c and d show the model grid (panel c is zoomed in to show refinement near the grounding line). The 3D grid in panel d has been vertically exagerrated by a factor of 4.

3.2 Model domain

Results from three distinct model configurations are presented in later chapters and their domains are described in this section. The 3D model is intended to represent a generic Antarctic ice-stream and as such its geometry does not match that of any particular one. The domain extends 100 km upstream from the grounding line and 50 km downstream, with a constant surface slope $\alpha = 0.002$ and bed slope $\beta = 0.001$. The model domain has a width of 32 km and due to the boundary conditions used (as discussed in Section 3.5) this leads to an overall ice-stream width of 64 km. The 2D model uses the same ice thickness and slopes as the 3D model but with a slightly smaller domain, extending 80 km upstream of the grounding line and 40 km downstream. Beneath both 2D and 3D models lies a 'till' layer whose deformation leads to u_b. Figure 3.1 (panels a and b) show schematics of both the 3D and 2D models.

The 3D coupled model (shown schematically in Fig. 3.2) extends 100 km upstream from the grounding line and 20 km downstream. The width of the model is 16 km, leading to an overall ice-stream width of 32 km, and the subglacial drainage layer extends a total of 200km upstream from the grounding line. The model geometry

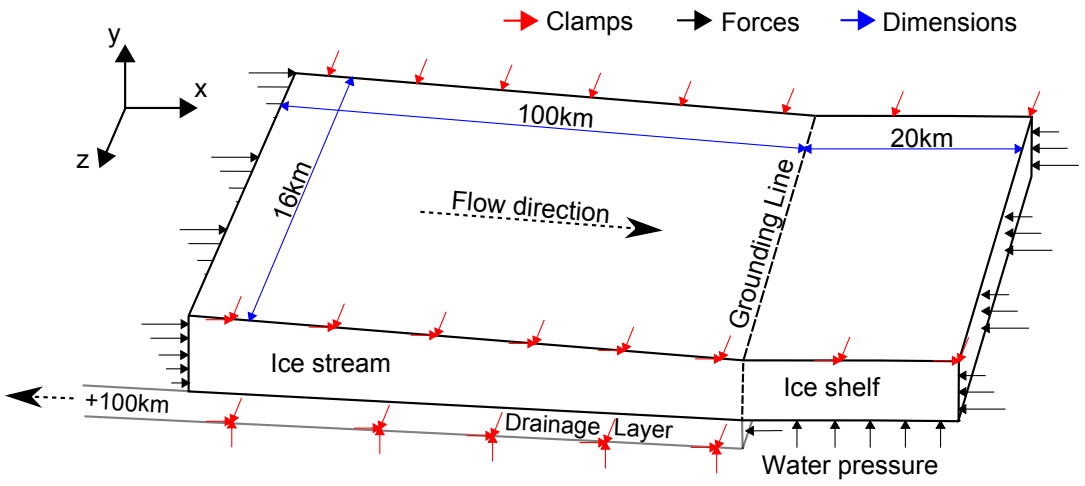

FIGURE 3.2: 3D coupled model domain, showing the boundary forces (black arrows) and flow constraints (red arrows). The subglacial drainage system extends a further 100 km upstream from the ice-stream boundary. Note that since the problem is symmetrical, the medial line is considered to be the plane $z = 0$ and the ice-stream being modelled is therefore 32 km wide. The term clamp is used to denote a node that cannot move in one or several degrees of freedom as indicated by the direction of the arrow.

is based on the RIS, however, I have not attempted to reproduce its geometry exactly and the thickness distribution in along-flow direction corresponds to the mean ice thickness across the ice-stream. It has has zero bed slope, a surface slope of 0.0036 and ice thickness at the grounding line of 2040 m. This simple geometry is derived from average bed and surface profiles along the RIS medial line from BEDMAP2 data [Fretwell et al., 2013]. While using constant slopes is a simplification and in reality the bed undulates considerably over the 100 km length being considered, there is no obvious overall shallowing or deepening, and the surface slope is relatively uniform.

3.3 Element discretisation

In 2D simulations an isoparametric, eight-node quadrilateral element was used, optimised for plane strain applications. Biquadratic interpolation functions are used to represent coordinates and displacements, and thus the strains have a linear variation within the element. The dimensions of the elements varied considerably

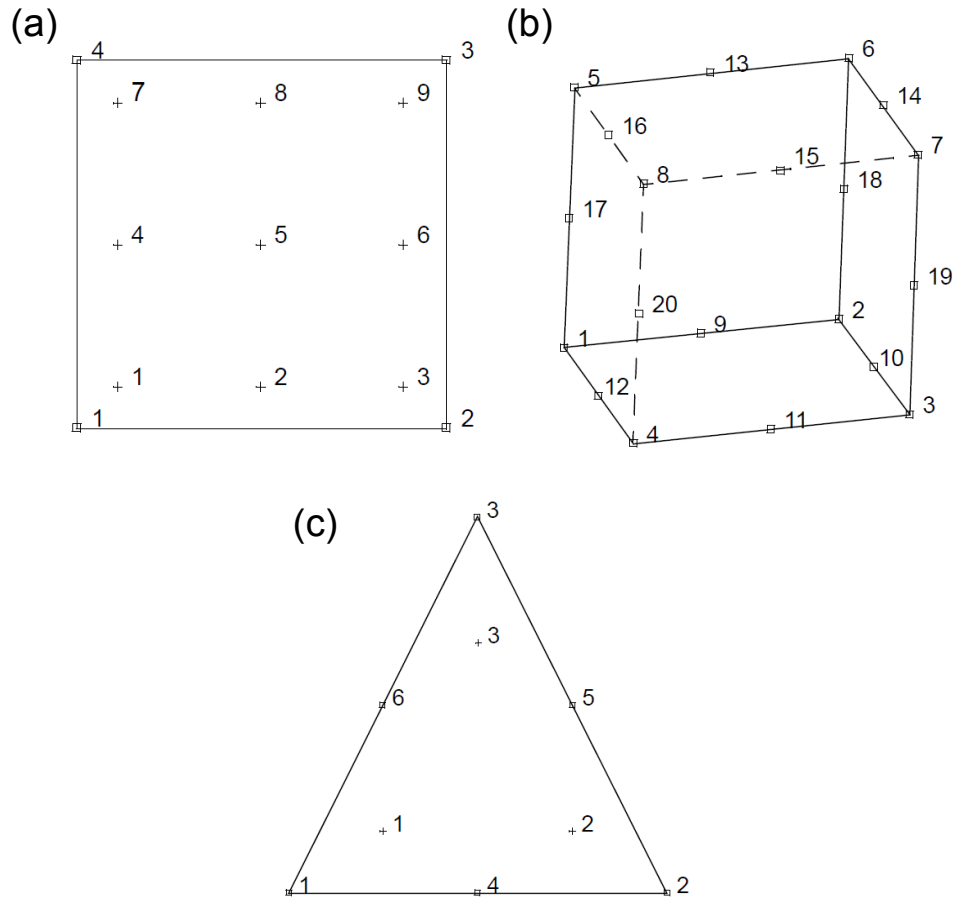

FIGURE 3.3: Nodes (squares) and gaussian integration points (crosses) for the elements primarily used in presented model simulations. Panel a shows the 20 node 3D brick element and panel b shows integration points through a plane of the element (the element has a total of 27 integration points). Panel c shows the 2D 6 node triangular element used in some contact simulations that involved very high resolution at the GL (Section 7.1).

from >1 km along much of the ice shelf to 30 m around the grounding line. A grid refinement of 150 m was initially used around the grounding line, but this was found to be insufficient and so the elements were subsequently reduced to the lower value. For both 3D and 3D coupled simulations an isoparametric, 20-node distorted brick was used with full integration, where each face consisted of eight nodes with the same layout as the 2D element described above. Dimensions vary considerably less than the 2D geometry and are typically 1.5 km, 2 km and 400m along the x, y and z planes, respectively.

3.4 Basal hydrology

The approach used to include a time varying subglacial hydrology within the finite element model is to reduce the problem to the simplest possible set of equations. Rather than attempt to model a complex system of connected channels and distributed flow, I treat the drainage system as a homogenous porous medium with a characteristic 'diffusivity' that, once coupled to the ice-flow model, can be tuned so that the velocity response matches observations. This approach to modeling subglacial hydrology has been used successfully in previous coupled studies eg. de Fleurian et al. [2014].

As a starting point it is necessary to lay out how the tide perturbs the subglacial water pressure. I write the subglacial water pressure (p_w) at any location upstream from the grounding line as

$$p_w(x,t) = \rho_w g \hat{h}(x,t) + \rho_w g(\bar{S} - b(x)), \tag{3.4}$$

where $\hat{h}(x,t)$ is the tidally induced perturbation in the hydrological head, ρ_w is the ocean density and the ocean surface elevation $S(t)$ is given by

$$S(t) = \bar{S} + \Delta S(t), \tag{3.5}$$

where $\bar{S}$ is the mean ocean surface elevation, and $\Delta S(t)$ the ocean tide. I incorporate the effects of the tides on subglacial water pressure through the grounding-line boundary condition for the perturbation in the hydrological head $\hat{h}$. I assume that at the grounding line the subglacial water system is in direct contact with the ocean, and the subglacial water pressure at that location is therefore equal to the ocean pressure, or

$$p_w(x,t) = \rho_w g(S(t) - b(x)) = \rho_w g(\bar{S} + \Delta S(t) - b(x)), \tag{3.6}$$

at $x = x_{gl}$, and hence

$$\hat{h}(x_{gl},t) = \Delta S(t), \tag{3.7}$$

The tidally-induced perturbation in hydrological head is then modelled as a diffusion process, i.e.

$$\partial_t \hat{h} = K \, \partial_{xx}^2 \hat{h}, \tag{3.8}$$

where K is the hydraulic diffusivity. In the context of Darcy groundwater flow, K can be expressed as

$$K = \frac{\rho_w g \kappa}{\mu S_s}, \tag{3.9}$$

where κ is the permeability, μ the viscosity of water, and S_s the specific storage capacity. In reality this parameter combination is poorly constrainted and here treated as an unknown.

Thus my approach is to solve for tidal perturbations in hydraulic head (rather than water pressure) which is known at the grounding line and transmitted upstream through a simple diffusion process controlled by the duffusivity K. When modeling the spatial and the temporal variations of the subglacial drainage system water, I only attempt to describe the perturbations in effective pressure due to tides. This avoids the complications of calculating the temporally-averaged pressure field, which is unnecessary as the effects of the mean pressure on basal flow are already accounted for in the temporally averaged value of the basal slipperiness which I derive in the inversion (Section 3.7).

The finite element software MSC.Marc has the capability of performing coupled thermal-structural simulations and I exploit the similarity between heat equation and Eq. (3.8) to enable me to solve for both effective pressure and ice flow simultaneously. This means the model is actually solving a temperature diffusion upstream from the grounding line but since K is treated as an unknown then in reality there is no need to differentiate between the two.

The goal in solving for hydraulic head is ultimately to obtain an effective pressure beneath the ice (Eq. 2.24). The hydraulic head is related to pore pressure (p_w) by:

$$\rho_w g \hat{h} = p_w + \rho_w g z, \tag{3.10}$$

where z is height relative to mean sea level (in this case $-b(x)$). This is coupled to the ice-stream model through the sliding law (Eq. 2.23) which I expand to consider perturbations in N:

$$u_b = c\frac{\tau_b^m}{(\overline{N} + \Delta N)^q} \tag{3.11}$$

where

$$\Delta N = -\rho_w g \hat{h}(x,t) \tag{3.12}$$

and $\overline{N}$ is mean effective pressure such that $N = \overline{N} + \Delta N$. Re-arranging this gives

$$u_b = c'\frac{\tau_b^m}{(1+\xi)^q}, \tag{3.13}$$

where $c' = c\overline{N}^{-q}$ and $\xi = \Delta N/\overline{N}$. This now puts slipperiness and mean effective pressure into a new c' term which is a function of x but not a function of t. In this way the baseline effective pressure and slipperiness conditions that affect the mean velocity of the glacier are separated from the perturbed terms. The c' term is what is inverted for, as described later, to match observed medial line flow. Re-arranging the equation in this way means that $\overline{N}$ only affects the relative size of the non-dimensionalised perturbation ξ and not the mean flow which is constrained by observations.

The 'effective diffusivity' (K) I refer to should not be compared directly to measured hydraulic diffusivity of till. Firstly, the system I model is a simplifcation of a number of different subglacial hydrological systems and the resulting diffusivity is just a characteristic value to represent the nature of the system. Secondly, since I only consider perturbations in hydraulic potential, the underlying gradient that must be present to force water downstream is not considered. Including this effect would mean that for the same fluxes resulting from tidal pressure variation you need a higher permeability to compensate.

In the non-coupled 3D and 2D simulations $\Delta N = 0$ and hence Eq. (3.13) reduces to a standard Weertman type sliding law with only 3 sliding parameters (τ_b, c and m).

3.5 Boundary conditions

Along the ice–bed interface upstream of the grounding line, a Weertman sliding law is used of the form given in Eq. (3.13), where basal resistive stress is defined as

$$\boldsymbol{\tau}_b = \boldsymbol{\sigma}\hat{\mathbf{n}} - (\hat{\mathbf{n}}^T \cdot \sigma\hat{\mathbf{n}})\hat{\mathbf{n}} \tag{3.14}$$

and $\hat{\mathbf{n}}$ is a unit vector normal to the ice bed interface.

Along the ice–ocean interface beneath the ice shelf, downstream of the grounding line, water pressure p_{w} acts normal to the ice surface:

$$p_{\mathrm{w}} = \rho_{\mathrm{w}} g(S(t) - z), \tag{3.15}$$

where ρ_{w} is the water density which is assumed to be constant ($1030\,\mathrm{kg\,m^{-3}}$). The tidal forcing in the model is introduced in the ΔS term (Eq. 3.5) with amplitude and period chosen depending on the simulation. For the 3D coupled model the tidal forcing is taken from the CATS2008 tidal model output [Padman et al., 2008], using the largest six tidal constituents at the RIS grounding line (M_2 , S_2, O_1, K_1, K_2 and N_2). The corresponding amplitudes used are listed in Table 3.1. This model performs particularly well in this region since it is constrained by previous GPS measurements in this area and comparison with the vertical GPS record of Gudmundsson [2006] shows very close agreement. Tidal currents beneath the ice shelf are not included in the model since the effect on basal drag is negligible [Brunt, 2008, Makinson et al., 2012] and effects on basal melt are too slow to affect velocities at daily timescales.

In all simulations the tide was only 'turned on' after a suitable amount of time had passed from startup, to allow the large initial elastic stresses to relax. For most simulations a time of 10 days was chosen after which the sea level was made a function of time. The tidal forcing was also ramped up from zero to full amplitude over a period of several days to avoid any numerical effects of immediately applying large sea level changes.

TABLE 3.1: CATS2008 tidal constituents and their approximate respective amplitudes near the RIS grounding line.

Tidal Constituent	Amplitude (m)
M_2	1.50
S_2	1.00
N_2	0.25
K_2	0.28
O_1	0.41
K_1	0.41

The ice–ocean interface boundary condition is implemented in the model as a linear elastic spring such that the pressure normal to the ice is given by

$$p_{\mathrm{w}} = k(z + z_0), \tag{3.16}$$

where k is the spring constant, z_0 the offset and z the position of the ice–ocean boundary. This is a convenient method for determining flotation within the software as it tends to converge faster than applying a direct vertical ocean pressure to the underside of the ice. Substituting in $k = -\rho_{\mathrm{w}} g$ and $z_0 = -S(t)$ gives Eq. (3.15). The result is that during high tide the maximum force is applied under the floating portion of the ice, lifting it vertically by the same distance as the tidal amplitude except for around the hinging zone.

At the upstream boundary of the model, a pressure p is applied normal to the ice:

$$p = \rho_i g(s - z), \tag{3.17}$$

where s is the ice surface and ρ_i is the ice density which is assumed to be constant ($917\,\mathrm{kg\,m^{-3}}$).

At the downstream boundary of the model, two different boundary conditions are used. In the 2D and 3D models I assume the ice shelf terminates at a calving front

and apply a normal pressure if the ice is below sea level, ie.

$$p = \begin{cases} \rho_{\mathrm{w}} g(S - z), & z < S \\ 0, & z > S \end{cases} \tag{3.18}$$

Although the assumption that the ice shelf is only between 40–50 km long is out by an order of magnitude for many of the large ice streams outflowing from Antarctica, it can be considered valid because the region of interest around and upstream of the grounding line is far enough away and fairly insensitive to the choice of boundary condition. In the 3D coupled model an alternative boundary condition was used in order to include the possibility of an additional buttressing term that could be inverted for in order to help match surface velocities of the RIS. The resulting pressure is based on the analytical solution for the flow of an ice-shelf in one horizontal dimension [Weertman, 1957] which gives

$$p = -\rho_i g(s - z) + \frac{\rho_i g h}{2}(1 - \wp) - p_b, \tag{3.19}$$

where p_b is the buttressing (addressed in Section 3.7).

In both 3D model configurations additional boundary conditions are applied which are not required for the 2D case. At both lateral boundaries of the model, the horizontal velocity component $v = 0$ and one side wall has the additional constraint that $u = 0$; however, vertical velocities are not constrained in this way anywhere. These additional boundary conditions replicate a situation where one margin of the ice stream is bounded by topography or ice with negligible velocity (no-slip) and the other side can be considered to be the ice stream medial line (free-slip). As a result of this choice of boundary conditions and the symmetry of the problem being considered, the ice-stream being modeled has a width which is double the model domain width and medial line velocities are taken along the free-slip sidewall.

Two boundary conditions are necessary in the 3D coupled model to solve for the diffusion of hydraulic head upstream from the grounding line. As mentioned earlier, at $x = x_{gl}$ subglacial water pressure and ocean pressure are assumed to

be equal, leading to the boundary condition given in Eq. (3.7). At the upstream boundary the condition $h \to 0$ as $x \to \infty$ is strictly correct for this form of diffusion equation. Since this is not possible to implement in the model I use $h = 0$ at $x = 200\,\text{km}$, assuming that h is very small at the upstream boundary. This can be justified analytically by solving Eq. (3.8) to give a decay length scale, for some periodic change in hydraulic head, of $\sqrt{2K/\omega}$ where ω is the tidal angular frequency being considered. For the range of diffusivity values and tidal frequencies considered here, the model domain of 200 km is far larger than this length scale, thus this boundary condition can be safely applied without influencing the model results.

3.6 Contact

The contact option of MSC.Marc is used to simulate the detachment and migration of the grounding line. The ice and till layer are defined as separate deformable contact bodies such that, during each incremental position, the software checks whether every potential contact node from each body is near a contact segment. A contact segment is either an edge of a 2D deformable body or the face of a 3D deformable body. In order to maximise computational efficiency, the software first defines a bounding box which quickly determines whether a node is near a segment; if the node falls within this box, more sophisticated techniques are used to find the exact status of the node. A contact tolerance is defined for each surface and if a node is within this tolerance region, it is considered to be in contact; if the node has passed through the tolerance range, it is considered to have penetrated and a procedure is invoked to avoid this penetration.

Once two contact segments come into contact, a 'glue' tying condition is applied so that there is no relative tangential motion between them. In the fully 3D case this is as far as contact goes; the two contact bodies remain glued throughout the procedure and the ice flows primarily by deforming the till layer. For simulations in 2D, where the grounding line migrates, the glue may separate, allowing the

grounding line to move back and forth with the time-varying ocean pressure. For the migration simulations presented here, the glue separation criterion is simply that the two bodies are released when the tensile force between them exceeds a certain stress. In reality, it would be expected that, as soon as tensile forces are greater than zero, the ice would lift and the grounding line would migrate; however, for numerical purposes, the separation stress is defined as a very small number to stop numerical chattering between segments. This avoids a situation where tiny variations in stresses between time increments cause two contact segments to repeatedly change in and out of contact at high frequency.

3.7 Bayesian inversion

Through preliminary modeling investigation it becomes apparent that the M_{sf} amplitude in the model is sensitive to mean flow conditions. Since matching the M_{sf} amplitude is not a goal of the 2D and 3D models this is not considered in depth. In these two models slipperiness does not vary spatially and it is tuned to get an approximate mean medial line velocity of $1\,\mathrm{m\,d^{-1}}$ to match typical fast moving Antarctic ice-streams. In the 3D coupled model, experiments were conducted in which the stress exponent of the flow law (m) was changed to examine the effect on M_{sf} response. Changing this parameter alters the mean flow in a non-trivial way that cannot be simply accounted for by altering slipperiness over the entire domain. For this model it is important when comparing results to keep the mean velocity as close to observations (and other simulations to enable comparison) as possible.

To reproduce the general pattern of observed surface velocities on RIS in the 3D coupled model I invert for slipperines (c') using the medial line velocities obtained from the MEaSUREs InSAR velocity dataset Rignot et al. [2011]. This slipperiness, which varies spatially but not temporally, encompasses various processes including but not limited to the effect of mean effective water pressure on basal motion. Although these InSAR derived velocities are potentially flawed in regions with long period tidal modulation in flow [Gudmundsson, 2006] this is addressed

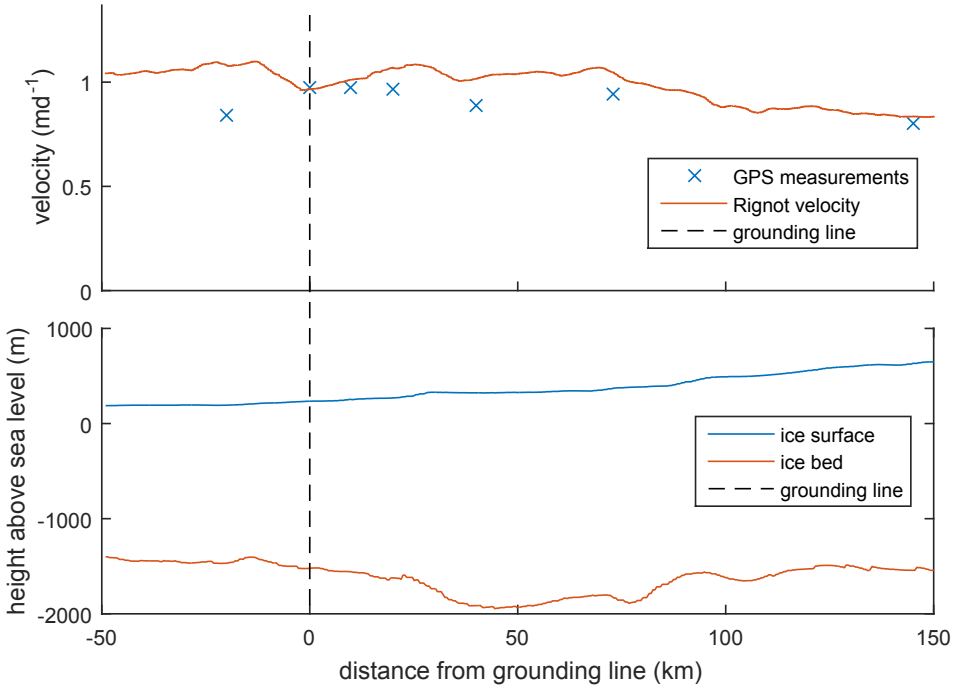

FIGURE 3.4: Medial line properties of RIS. The top panel compares surface velocities obtained from the MEaSUREs dataset Rignot et al. [2011] with mean velocities extracted from in-situ GPS measurements. The bottom panel shows surface and bed profiles from BEDMAP2 Fretwell et al. [2013] along the same line. Note that BEDMAP2 has no data for water column thickness near the grounding line and so this is not plotted.

by increasing the a-priori error estimate (discussed later) to be larger than the errors provided in the dataset. In general a comparison of the InSAR velocities with in-situ GPS measurements does show some differences but the only large discrepancy is on the ice shelf where I do not attempt to match the surface velocities. A plot showing InSAR velocities obtained along the RIS medial line and compared with mean velocities derived from GPS measurements is shown in Fig. 3.4.

A Bayesian inversion approach was used to empirically calculate the $i \times j$ sensitivity matrix $\mathbf{K}$ describing the sensitivity of surface velocities to basal slipperiness. The method and equations are broadly similar to those presented in Raymond and Gudmundsson [2009] except that, rather than using analytical expressions for the sensitivity matrix, it is computed as the partial derivative of the forward model

with respect to the state vector. The sensitivity matrix is given by

$$[\mathbf{K}]_{pq} = \frac{\partial u_p}{\partial c'_q}, \tag{3.20}$$

where p and q are nodal numbers along the upper and lower surfaces of the finite element mesh. Here the measurement vector u has i elements and is the surface velocity, and the state vector c' has j elements and is the slipperiness at the bed. Thus I calculate, for each element of the state vector, the change in measurement vector, giving one entire column of $\mathbf{K}$. This is repeated for every element of the state vector to build up a complete sensitivity matrix.

Since the model response to a change in slipperiness is nonlinear, the inversion will not converge to an optimum solution in a single iteration and so a Newton-Gauss iterative approach is used of the form

$$c'_{i+1} = c'_i + \hat{\mathbf{S}}^{-1}(\mathbf{K}_i^T \mathbf{S}_e^{-1}[u - \mathbf{F}(c'_i)] - \mathbf{S}_a^{-1}[c'_i - c'_a]), \tag{3.21}$$

where

$$\hat{\mathbf{S}}^{-1} = \mathbf{K}_i^T \mathbf{S}_e^{-1} \mathbf{K}_i + \mathbf{S}_a^{-1} \tag{3.22}$$

is the Fisher information matrix, $\mathbf{S}_e$ is the covariance of measurement errors, $\mathbf{S}_a$ is the covariance of a-priori errors, c'_a is the a priori estimate, and $\mathbf{F}(c')$ is the forward model [Rodgers, 2000]. Measurement errors (σ_e) are assumed to be uncorrelated and have a normal distribution, such that the measurement error covariance matrix is proportional to the identity matrix, in the form $\mathbf{S}_e = \sigma_e^2 \mathbf{I}$. I choose a large value of $0.2\,\mathrm{m\,d^{-1}}$ for σ_e to account for errors arising from undersampling of tidal effects in this area.

Treatment of the prior covariance matrix is the same as Gudmundsson and Raymond [2008], based on the assumption that basal slipperiness is spatially correlated, whereby each prior estimate of c' at location i is related to a neighbouring location $i-1$ by

$$c'_i = \phi_c c'_{i-1} + \epsilon_c \tag{3.23}$$

where ϵ_c has variance σ^2. The elements of $\mathbf{S}_a^{-1}$ can then be given by

$$[\mathbf{S}_a]_{pq} = \sigma_a^2 \, e^{-|p-q|/\lambda_c}, \tag{3.24}$$

where λ_c is a decay length scale, related to ϕ_c by $\lambda_c = -1/\ln \phi_c$ and the variance is

$$\sigma_c^2 = \frac{\sigma^2}{1-\phi_c^2}. \tag{3.25}$$

This results in a covariance matrix which has σ_a^2 along the diagonal and non-zero off-diagonal elements.

I reduce the number of calculations needed by only taking into account along-flow variations in slipperiness. Since I only invert for the medial line velocity and the geometry I use is idealised this simplification is valid. Buttressing (p_b, which is particularly relevant for flow velocities near the grounding line) is inverted for by adding a single non-dimensionalised element to the end of the state vector. This is treated in the same way as the other state vector elements apart from having its own (uncorrelated) prior error estimate.

Ice viscosity is not inverted for as this is only likely to make a big difference on the ice-shelf. Flow velocities on the shelf increase rapidly downstream of the grounding line and inverting for viscosity would help match actual velocities in this region, however since the effect being considered is generated upstream of the GL this is not done. The buttressing term helps alleviate the fast ice-shelf flow to some extent but adjusting sipperiness and buttressing alone is not sufficient to perfectly match flow velocities near the GL. The inversion procedure is shown as a flow diagram in Fig. 3.5. The forward model is first run with an initial guess of the state vector to produce $\mathbf{F}(c_i')$. The matrix $\mathbf{K}_i$ is constructed by altering each element of c_i' by 1% with the resulting change in $\mathbf{F}(c_i')$ giving one column of $\mathbf{K}_i$. The inversion procedure given in Eq. (3.21) is then run and checked for convergence. If the solution has not converged a new updated value $\mathbf{F}(c_{i+1}')$ is used in the forward model and the process repeated. I choose to use the a-priori

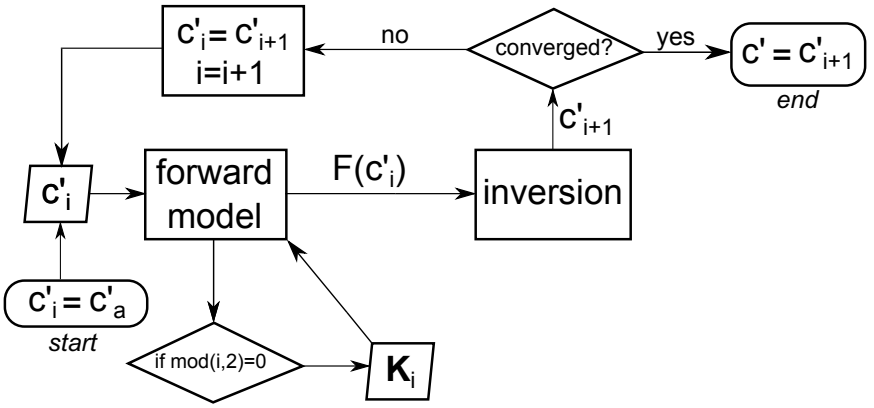

FIGURE 3.5: Flow diagram of the inversion procedure. The transfer function matrix is re-calculated every 2 iterations, at which point the forward model is run once for each column of $\mathbf{K}$ (simultaneously). Note that c'_a is used in the inversion but not updated at any point during the procedure.

estimate for the state vector as the initial guess in the Newton-Gauss iterative procedure although this is not essential.

This approach, whereby each column of $\mathbf{K}_i$ is calculated explicitly by running the forward model, could be termed a 'brute force' approach and although it is computationally more expensive than others such as the adjoint method, there are a number of advantages of this method such as giving an explicit estimate of the inversion error. The sensitivity matrix need not be calculated for each iteration and in fact it is advantageous to iterate a number of times using the same matrix before re-calculating it. Furthermore, because each element of the $\mathbf{K}$ matrix is independent of all the others, it is possible to easily parallelize its calculation, meaning that run times need not be orders of magnitude greater if sufficient computing resources are available. In order to considerably increase the computational speed of the forward model, a purely viscous rheology is used for the inversion which is valid since it is the viscous deformation that alters mean flow.

The iteration was continued until it converged on the maximum a posteriori solution, in contrast to many other similar studies which stop iterating once the misfit between model output and observations is below a given threshold. The cost function is calculated as $[c'_i - c'_a]^T \mathbf{S}_a^{-1} [c'_i - c'_a] + [u - \mathbf{F}(c'_i)]^T \mathbf{S}_e^{-1} [u - \mathbf{F}(c'_i)]$.

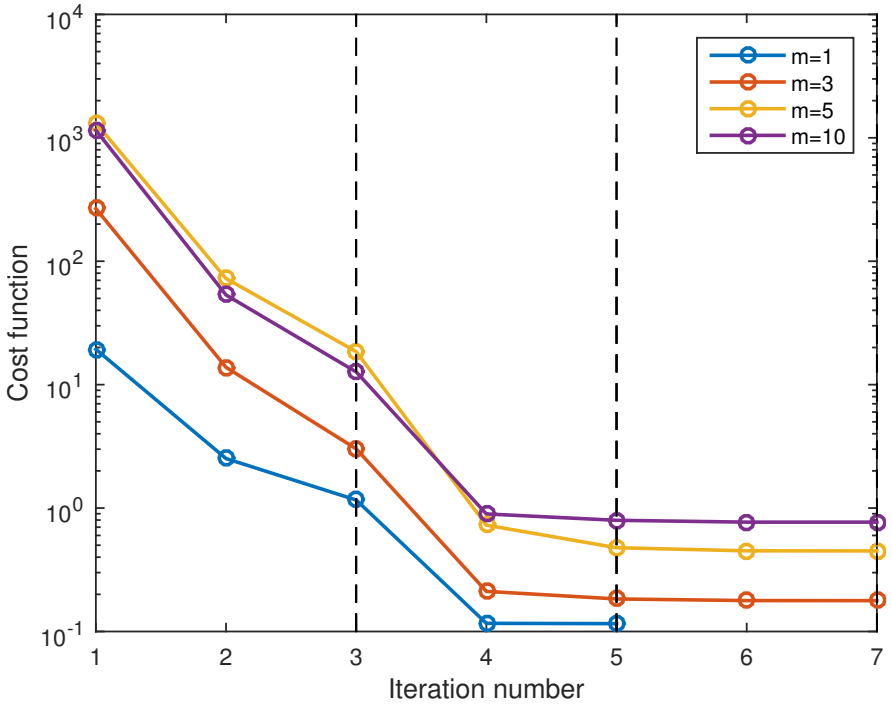

FIGURE 3.6: Convergence of the cost function for values of m ranging from 1 to 10. Dashed vertical lines represent re-calculation of the transfer function matrix.

The rate of convergence is plotted in Fig. 3.6. Rate of convergence appears fairly constant for a range of values of m, however the cost function converges to a larger value for increasing m. This is likely due to boundary affects and the final values represent a small misfit to observations when divided by the number of elements of c_i'. The final inverted velocities and slipperiness values are plotted in Fig. 3.7. The final inverted slipperiness values show considerably undulation along flow, however these values should not be taken to mean anything about the nature of the bed in this area, particularly because the model geometry is so simple and slipperiness is not allowed to vary laterally.

3.8 Unknown parameters

The set of equations described above leads to six constants: $\overline{N}$, K, ν, E, m and q which are treated as unknowns. The rheological parameters E (Young's modulus) and ν (Poisson's ratio) are constrained to some extent from previous visco-elastic modeling efforts on tidally induced motion (Section 2.3), a range of 1-6GPa is used

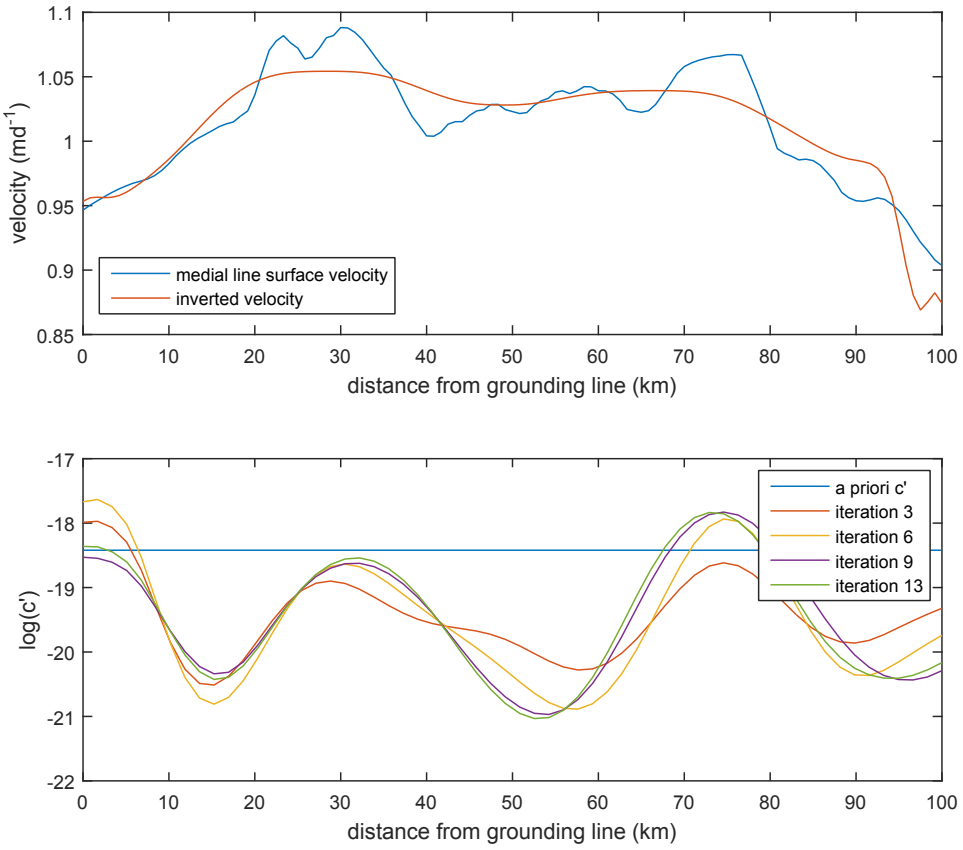

FIGURE 3.7: Results of the inversion, showing inverted medial line velocities compared to the InSAR derived velocities from Rignot et al. [2011] (also plotted in Fig. 3.4) in the top panel and the log of slipperiness c' at different stages in the inversion procedure in the bottom panel.

for E and 0.41-0.45 for ν. The sliding law exponents m and q are treated here as unknown parameters and the goal is to understand how the model responds to different values. An optimal choice for the form of the sliding law is that which can reproduce the observed response of an ice stream to tida forcing. For these parameters, unlike the inversion approach used for slipperiness, an informal approach is used to find their optimal values, whereby the exponents are changed until the model agrees well with observations in an iterative manner.

In spite of the importance that these exponents play in modeling large-scale ice masses and the extensive use of a sliding law of this form, there is still debate as to their values, choices ranging from 0 to infinity are commonly used in modelling studies of the flow of large ice masses (e.g. Cuffey and Patterson [2010], Walker

et al. [2012]). Note that once c' has been determined, through the inversion procedure outlined below, K and $\overline{N}$ only affect modeled flow through their combined effect on ξ.

Chapter 4

Tides and Tidal modeling

4.1 Ocean Tides

The phenomenon of ocean tides has been observed and studied by humans for millenia. Ocean tides are a consequence of the gravitational attraction of celestial bodies, most importantly the sun and moon, which gives rise to the 'tide producing force' (TPF). As these bodies move in relation to earth the TPF varies both temporally and spatially over the earth's surface. This means that modeling local tide around a continent such as Antarctica can be a complex issue, particularly due to uncertainties in bathymetry and the complication arising from floating ice-shelves. In this chapter I will set out the equations that are typically used in tidal models to calculate tides around Antarctica and describe the theory behind them.

4.1.1 Equilibrium theory of tides

Gravitational force acting on two bodies, of mass m_1 and m_2 and distance r_1 is

$$F_g = G_c \frac{m_1 m_2}{r_1^2} \tag{4.1}$$

where G_c is the gravitational constant. Thus, although the moon is small relative to other celestial bodies, gravitational force is proportional to to the inverse of

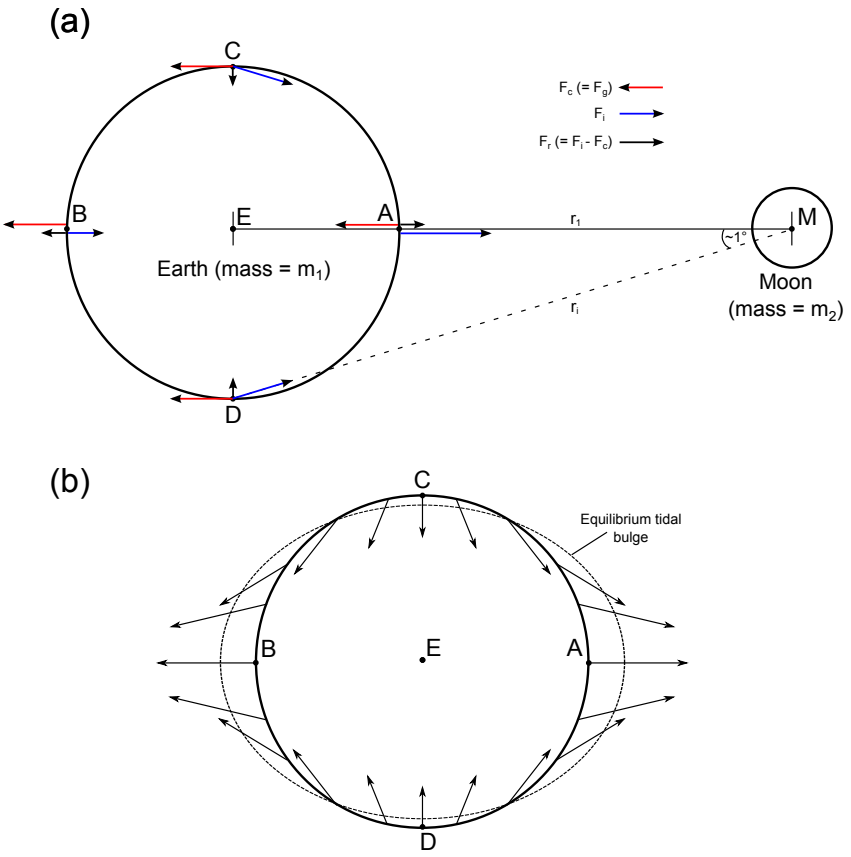

FIGURE 4.1: Force schematic showing the generation of the residual TPF (black lines) as the difference between the centripetal (red lines) and gravitational (blue lines) forces of the earth and moon (panel a). The diagram is not to scale and the angle CME is only approximately 1°. The TPF residuals are resolved at various points on the earth's surface (panel b) and the resulting tidal bulge that arises is outlined as a dashed line.

.

distance squared and only linearly dependent on mass, hence due to its proximity to earth the moon contributes the most to the TPF on earth.

Figure 4.1 shows the gravitational force of the moon resolved at four points (A, B, C and D) on the earth's surface. This force is largest at A because it is closest to the moon and smallest at B. The gravitational force (F_i) at each point i of distance r_i is balanced by the centripetal force F_c which keeps the earth-moon orbit in a (relatively) steady state (note: not the centripetal force of earth's rotation which is balanced by gravity). Crucially this force is constant everywhere on the earth's surface and thus regions of force imbalance occur. The spatial variation in F_i is

TABLE 4.1: Tidal constituents and their respective periods, adapted from Pond and Pickard [2003].

Species and name	Symbol	Period (hours)	Relative size
Semi-diurnal:			
Principal lunar	M_2	12.42	100
Principal solar	S_2	12.00	47
Larger lunar elliptic	N_2	12.66	19
Lunar-solar semi-diurnal	K_2	11.97	13
Diurnal:			
Lunar-solar diurnal	K_1	23.93	58
Principal lunar diurnal	O_1	25.82	42
Principal solar diurnal	P_1	24.07	19
Larger lunar elliptic	Q_1	26.87	8
Long period:			
Lunar fortnightly	M_f	327.9	17
Lunisolar synodic fortnightly	M_{sf}	354.37	$\sim$
Lunar monthly	M_m	661.3	9
Solar semi-annual	S_{sa}	4383	8

actually quite small, with a range of about $\sim 6\%$, but this is sufficient to generate the oceanic lunar tide [Pond and Pickard, 2003].

One of the first attempts to describe the ocean tide was Newton's theory of the equilibrium tide. In Newton's model the earth is covered everywhere by an ocean of uniform density and depth. The net force $(F_i - F_c)$, marked with black arrows in Fig. 4.1, is the tide producing force and leads to a tidal bulge at points A and B. After some time an equilibrium would be reached where a pressure gradient force from the slope of the tidal bulge balances the TPF. As a result, at most points on the earth's surface an observer would experience approximately two high and low tides each day (the actual figure is slightly less than 2 lunar tides per day because in the time it takes for the earth to rotate once the moon has rotated also, hence the name semi-diurnal). Newton's equilibrium tide approach was a big leap forward and successfully explains many of the features of the oceanic tide, but its many simplifications mean it is unable to replicate the more complex aspects of local tides.

4.1.2 Dynamical theory of tides

A fundamental limitation of the equilibrium theory is that the tidal bulge's motion across the earth's surface is hindered by the landmasses and its velocity is limited. The tidal wavelength is much larger than ocean depth and hence its velocity is given by the phase velocity of a dispersive wave which is simply $\sqrt{gH}$. About a century after the equilibrium tidal theory was developed, Laplace put forward his dynamical theory of tides. This system of equations, derived by simplifying the fluid dynamic equations, considers the astronomical forcing to be balanced by the pressure gradient force, local and coriolis accelerations.

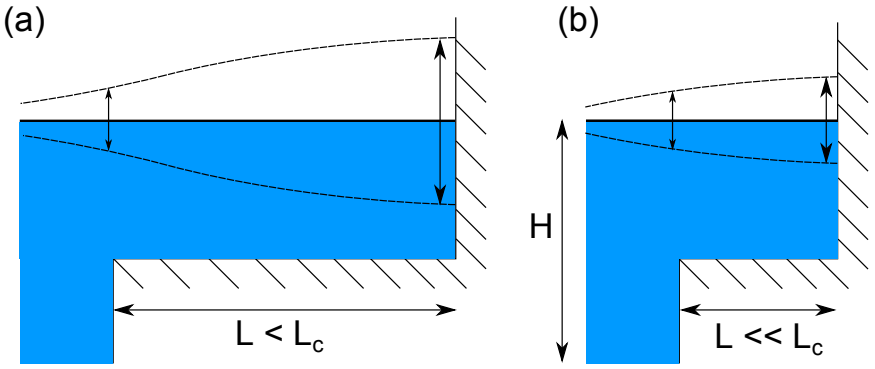

FIGURE 4.2: Tidal resonance for bays of depth H and length L, where L_c is the critical length for a quarter wave oscillator, adapted from Pond and Pickard [2003].

An important aspect of this dynamical theory of tides is tidal resonance which helps account for some of the very large tidal ranges observed in the world's oceans. A simple example of resonance is that of a long narrow body of water which is closed at one end. A wave entering this system causes sea level and velocity to oscillate and will travel to the end of the bay, where it is reflected back. The incoming and reflected wave can constructively interfere, resulting in a set of nodes (no amplitude) and anti-nodes (amplification). In the case of tides, if the bay is long enough compared to the tidal wavelength the resulting amplification at anti-nodes can be very large (as depicted in Fig. 4.2). The dimensions of a quarter wave oscillator have a natural oscillation period (T_f) of

$$T_f = \frac{4L_c}{(gH)^{1/2}} \tag{4.2}$$

where L_c is the length of the bay [Pond and Pickard, 2003]. Although in reality bays do not conform to simple idealised geometries, this formula can still provide a rough estimate given the average depth of a bay. An example of this is the Bay of Fundy, with an average depth of ∼100m and length of ∼300 km, has a natural oscillation period close to that of the semidiurnal tide and this has been used to explain its large tidal range of ∼15m.

An additional important feature of tides that arises from the inclusion of the coriolis affect due to earth's rotation is that the tide travels as a rotary wave in a large basin. Rotation causes moving parcels of water to be deflected to the left in the Southern Hemisphere. In the case of tides, this causes the tidal wave to rotate around the basin in a clockwise direction around a central points with zero tidal amplitude, known as an amphidromic point. Radiating from this central node are co-phase lines (lines along which the tidal phase is equal) and co-range lines (lines of equal tidal amplitude) as shown in Figure 4.3. A basin must be large enough for rotational effects to be important and a commonly used equation gives the Rossby radius:

$$L_R = \frac{(gH)^{1/2}}{f}, \tag{4.3}$$

where f is the latitude dependent coriolis parameter, as the length scale at which rotation becomes as important as buoyancy and gravity effects.

The special case of a standing wave on a rotating earth that gives rise to amphidromic points as outlined above is a form of Kelvin wave. The location of the node around which the Kelvin wave rotates is affected by the relative strength of the incoming and outgoing waves. In the southern hemisphere, a greater dissipation of energy within the channel reduces the strength of the Kelvin wave and shifts the amphidromic point to the right of the direction of the incoming wave ie. towards the area of increased dissipation Taylor [1921].

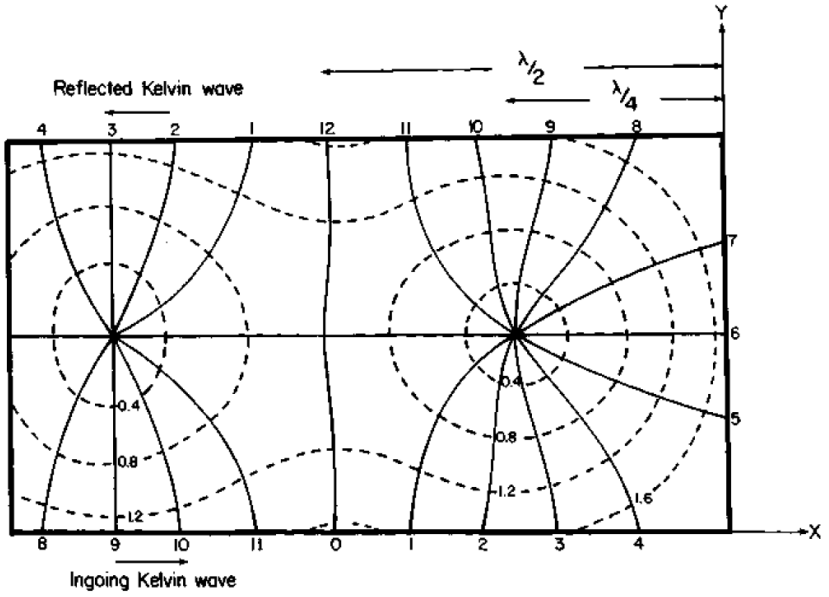

FIGURE 4.3: A kelvin wave entering a channel and reflected with no energy loss. Solid lines are co-phase lines and dashed lines are coamplitude lines. The channel in this case is in the northern hemisphere. Taken from Pugh [1996].

4.1.3 Shallow water equations

The shallow water equations are derived by integrating the Navier-Stokes equations with respect to depth and assuming that the water body is shallow with respect to its horizontal extent. Under these circumstances the u and v velocity components are constant with depth. The water body is bounded by bottom topography at its base and a free surface above. The resulting set of equations, including rotation but neglecting friction, can be written out in full in terms of velocities as

$$\dot{u} + u\partial_x u + v\partial_y u - fv = -g\partial_x S + F_x - F_{xb} \tag{4.4a}$$

$$\dot{v} + u\partial_x v + v\partial_y v + fu = -g\partial_y S + F_y - F_{yb} \tag{4.4b}$$

$$\dot{S} = -\partial_x(u(H+S)) - \partial_y(v(H+S)), \tag{4.4c}$$

where S is the sea level and H is water depth (under no external forcing). Equations (4.4a) and (4.4b) represent the momentum balance in x and y between acceleration, advection, rotation, the pressure gradient force, surface driving stresses (such as the wind) and energy dissipation, e.g. due to bottom stress (respectively,

from left to right). Equation (4.4c) is simply a result of integrating mass conservation over the entire depth. The equations in this form are sometimes termed the non-conservative form because they will not hold across a hydraulic jump (where water of high velocity meets slower moving water).

These equations are used extensively in oceanography in various forms and can often provide a very close approximation of the actual flow. Typically various further simplifications are made, such as ignoring friction or advective terms which can often be computationally expensive and cause numerical difficulties. In recent times many tidal models solve a form of the shallow water equations given above, which are well suited to dealing with the ocean tide which has a long wavelength.

4.2 Tidal modeling

Tidal modeling is conducted to examine the effects of changing ice-shelf configurations on local ocean tides. Two tidal models are discussed and used in this thesis, the Oregon State university Tidal Inversion Software (OTIS) and the Circum Antarctic Tidal Simulation (inverse model version 2008a, CATS2008) model. All the forward modeling is done using OTIS and this model will be discussed in most detail. The CATS2008 inverse model is particularly useful for validating the OTIS model and providing accurate tidal amplitudes near ice-stream grounding lines because it is heavily constrained by data. Incidentally this is the same reason it cannot be used in runs examining perturbations in ice-shelf thickness and extent since the data it is constrained by would no longer be correct under a new tidal regime.

4.2.1 OTIS

The Oregon State University Tidal Inversion Software (OTIS) solves the rotating shallow water equations (Eq. 4.4) subject to tidal forcing only and neglecting nonlinear advection terms and horizontal diffusion. This model has been used

and validated extensively to simulate past, present and future tidal regimes at a variety of scales (e.g. Egbert et al. 2004, Green 2010, Green and Huber 2013, Green and Nycander 2013, Rosier et al. 2014a, Wilmes and Green 2014). The resulting system of equations is

$$\partial_t \mathbf{U} + f \times \mathbf{U} = -gh\nabla(S - S_{SAL} - S_{EQ}) + F \tag{4.5}$$

$$\partial_t S = -\nabla \cdot \mathbf{U} \tag{4.6}$$

where $\mathbf{U} = \mathbf{u}H$, $\mathbf{u}$ is the total velocity vector for all constituents, water depth is H, f is the Coriolis vector, S is tidal elevation, S_{SAL} is the self-attraction and loading elevation (taken from satellite altimetry data, and not changed between the simulations), S_{EQ} is the equilibrium tide, and $F = F_b + \mathbf{F}_w$ parameterizes energy losses due to bed friction (F_b) and tidal conversion ($\mathbf{F}_w$). The first of these terms use a standard quadratic drag law, $F_b = C_d\mathbf{U}|\mathbf{u}|/H$ ($C_d \sim 0.003$ is a drag coefficient) represents bed friction, whereas the conversion is parameterized by the scheme presented by Zaron and Egbert [2006] (see Green and Nycander 2013 for details). The latter is quite crude but computationally efficient, and it allows for conversion polewards of critical latitudes. It must be noted, however, that the conversion is relatively weak in this domain and bed friction dominates the shelf seas under investigation here.

Grid spacing is 1/12 degrees in both longitude and latitude and simulations were undertaken for the M_2, S_2, K_1 and O_1 constituents, with M_4 being an additional part of the output (but not included in the forcing). Note, however, that I focus on M_2, K_1 and M_4 in simulations that use this model. Note that although, as the name suggests, the OTIS model has the ability to perform an inverse step, only the dynamical forward model component was used in the simulations I present later.

The bathymetry is a composite of various datasets described by Padman and Fricker [2005], whereas the water column thickness under the ice shelves and the ice shelf thickness are from BEDMAP [Lythe and Vaughan, 2001]. Forcing at the open

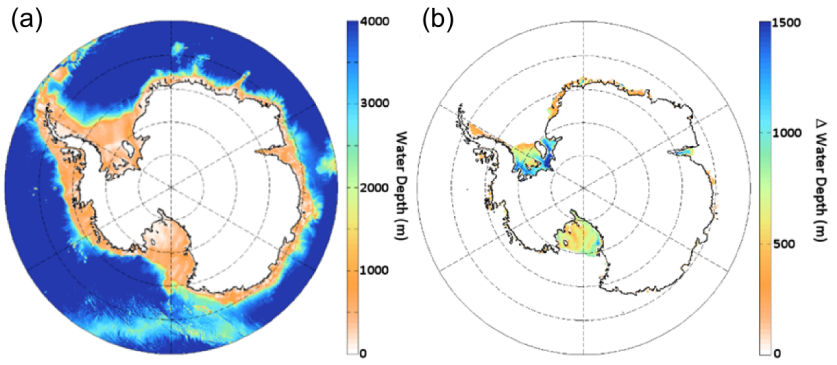

FIGURE 4.4: Bathymetry of the domain used in the tidal model (panel a) along with the difference in water column thickness between the no ice and control simulations (panel b).

boundary at 60°S consisted of elevations from the inverse TPXO7.2 solution (see Egbert and Erofeeva [2002] for the methodology and http://volkov.oce.orst.edu/-tides/global.html for the data). Although the changes in ice shelf configuration outlined in Section 4.2.3 would require considerable perturbation in climate which may lead to changes in sea level, the open boundary is in the deep ocean and therefore is assumed to be largely unaffected by these changes (this is supported by the simulations in Green 2010 and Wilmes and Green 2014). In order to further ensure the location of the open boundary did not affect results, several simulations were done at different latitudinal boundaries (62°S and 65°S) and results remained unchanged.

4.2.2 Dissipation

The tidal dissipation, D, can be computed using the model output as the difference between the work done by the tide producing force (W) and the divergence of the barotropic energy flux ($\nabla \cdot \mathbf{P}$) [Egbert and Ray, 2001]:

$$D = W - \nabla \cdot \mathbf{P} \tag{4.7}$$

W and $\mathbf{P}$ are defined as

$$W = g\rho \langle \mathbf{U} \cdot \nabla (S_{EQ} + S_{SAL}) \rangle \tag{4.8}$$

$$\mathbf{P} = g\rho \langle \mathbf{U} S \rangle \tag{4.9}$$

in which the angular brackets mark time-averages and the small Earth tide has been neglected.

4.2.3 Ice-shelf configuration

Several representations of the floating ice-shelves were implemented in the model to test the sensitivity of the tides around Antarctica to changes in ice sheet geometry. The control run used water column thickness from the databases and a doubled bed friction under the ice shelves to simulate the enhanced drag under the shelves [MacAyeal, 1984, Padman et al., 2002]. Where present, the floating ice shelf is treated as a purely passive object and elastic forces near the grounding line are not considered. Simulations of removal of the Ronne-Filchner and Ross ice shelves (henceforth denoted "no ice") added the ice draft given by BEDMAP to water thickness beneath the shelf in order to provide a total water depth, H, under ice free conditions. Figure 4.4a shows bathymetry used in the control simulation and Fig. 4.4b shows the difference in water column thickness between the control and no ice simulations.

Runs were also undertaken in which the ice shelf thickness was halved ("HT"), in which both the Ronne-Filchner and Ross ice-shelf extents were halved with no change to the remaining shelf thickness ("HE"), and in which both extents and thicknesses were halved ("HTE"). In HE and HTE runs the extent was halved by removing the shelf beyond latitudinal lines, resulting in approximately half the original shelf area, and the areas of increased bed friction were also altered to reflect this configuration.

A number of other runs with various combinations of ice-thickness and enhanced drag under the ice were also undertaken to test the sensitivity of the model to parameter values. It was found that increasing the bed friction under ice by a factor of 20 and slightly reducing ice shelf thickness improved accuracy compared to the heavily assimilated CATS2008a model [Padman and Fricker, 2005, Padman

et al., 2008], but I decided that this minor improvement does not justify the alterations to the default parameterization of ice shelves within the model where bed friction is doubled beneath the ice shelf. The increased accuracy resulting from increasing bed friction is not unexpected since the drag coefficient describes a roughness scale and the resolution of the bathymetry used – both at the bed and under the ice – is not fine enough to pick up the inherent roughness of the bed and particularly the underside of the ice.

4.2.4 CATS2008 model

The Circum-Antarctic Tidal Software model (CATS2008, Padman et al. [2002, 2008]) uses data assimilation to greatly improve the accuracy of tidal models in the circum-Antarctic region south of 56°S. The model grid is polar stereographic, with a resolution of ∼4 km and standard latitute of 71°S. Water depth is taken from the 2007 update of the Smith and Sandwell [1997] dataset and water column thickness beneath ice-shelves is taken from a variety of different sources, outlined in Padman et al. [2002]. Grounding line location is taken largely from the MOA feature identification dataset in Scambos et al. [2007], but locally adjusted with ICESat and InSAR derived grounding zone locations around the Ross, FRIS and Larsen ice shelves.

The forward model component of the CATS2008 model solves the linearized shallow water equations (Equation 4.4). The model is forced at the open boundary by astronomical potential and sea surface elevation from the TPX07.1 inverse model. Ten tidal constituents are solved for (M_2, S_2, N_2, K_2, K_1, O_1, P_1, Q_1, M_f and M_m), and each is tuned separately to data using a linear benthic drag coefficient. Ice shelves are treated as in the OTIS model, with a doubling of bed friction where the ice shelf is present. The model is kept intentionally simple but still retains enough accuracy to produce a reasonably accurate a-priori estimate of tidal heights for the assimilation step.

The Cats2008 model uses data assimilation with measurements from a number of sources to improve the accuracy of the tidal model using inverse methods. Where sea ice is not present and the domain is sufficiently far north TOPX/Poseidon altimetry data from the ocean is used. Measurements of the ocean tide taken from ice shelf GPS records, tide gauges and bottom pressure recorders are used where available (a total of approximately 50 around the entire region). Finally ICESat laser altimetry from the FRIS and Ross ice shelf has been included [Padman and Fricker, 2005, Padman et al., 2008].

The resulting model is currently one of the most accurate tidal models in the Antarctic region. A tidal simulation of the Ross Ice shelf found that for K_1, the most energetic tidal constituent in the region, the root mean-square error (RMSE) is reduced from 6.0 to 2.8cm. The combined RMSE for the six most energetic tidal constituents compared to the best available data is 4.8cm [Padman et al., 2008]. A study of model accuracy for the Antarctic region, comparing a number of global and circum-Antarctic tidal models, found that TPXO6.2 had the lowest overall RMSE for the entire region [King and Padman, 2005], however the CATS model version tested in this study did not include assimilation of ICESat data which greatly reduced the RMSE of CATS. Taking this into account, the CATS2008 model is arguably the most accurate circum-Antarctic tidal model available and for this reason I use it in a number of cases in this thesis for model comparison and to provide local tidal heights.

Chapter 5

Results of a 3D ISS model

This chapter is based on parts of a manuscript entitled "Insights into ice-stream dynamics through modeling their response to tidal forcing", published in the Cryosphere on the 25$^{\text{th}}$ of September 2014 [Rosier et al., 2014b].

In this chapter I present results of a FS viscoelastic 3D ISS model and attempt to qualitatively match observed long period modulation of ice-stream flow at M_{sf} frequency. The model used is the un-coupled 3D model, described in detail in Chapter 3, with a different geometry to the coupled 3D model and a sliding law in which $q = 0$. I begin by showing that, in line with previous 2D work [Gudmundsson, 2007, 2011], a nonlinear sliding law where $m > 1$ can produce long period modulation in flow, even with the addition of lateral drag from sidewalls. I then derive expressions for various stress-coupling length scales from a very simple form of the SSA and compare these with the 3D model.

5.1 3D Results

Numerical simulations initially focus on fully 3D FS modeling of the response of an ice stream to tidal forcing. Figure 5.1 shows modeled horizontal displacements along the medial line of the ice stream 11, 21 and 31 km upstream of the grounding

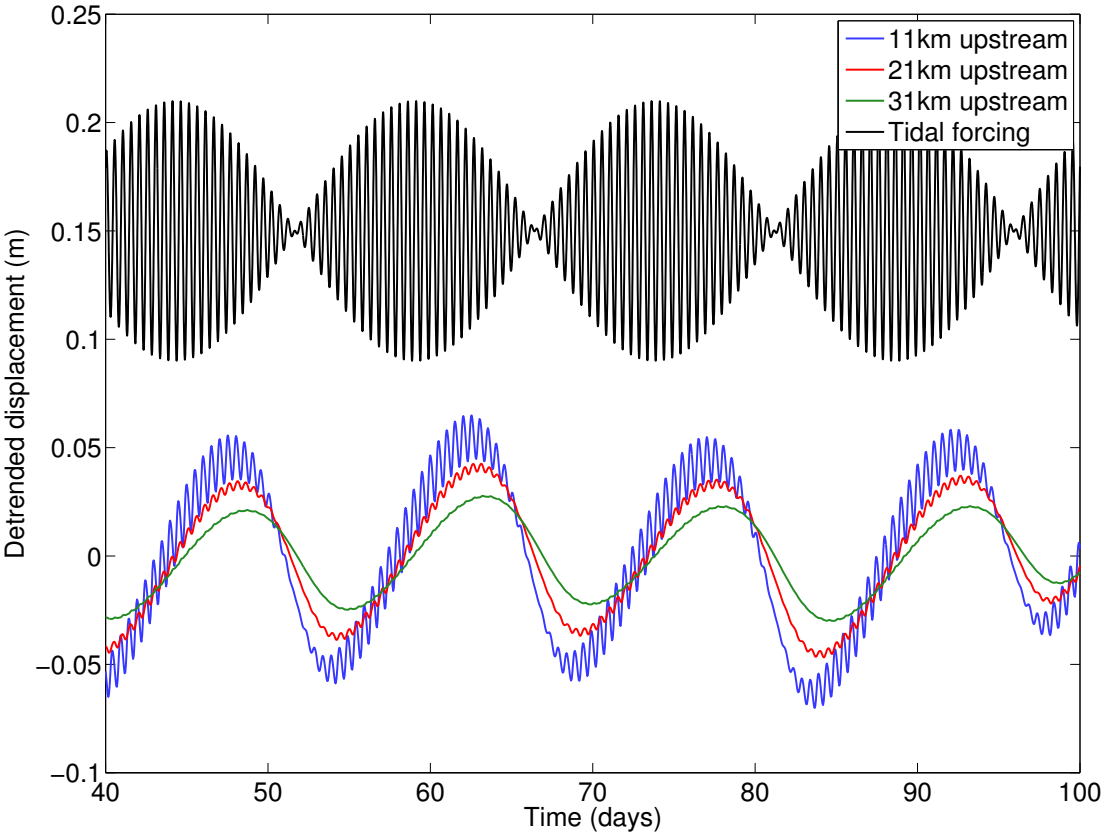

FIGURE 5.1: De-trended in-line displacements at 11, 21 and 31 km upstream of the grounding line for the 3D model run using an idealised Rutford Ice Stream geometry. The tidal forcing is also shown, scaled down by a factor of 50 and shifted vertically.

line. The tidal forcing consists of M_2 and S_2 tidal constituents only, with amplitudes of 2m each, and is plotted alongside the ice stream response (scaled down by a factor of 50 and shifted vertically).

The model geometry that produced these results had a domain as shown in Fig. 3.1 (panels b and d), with ice thicknesses and slopes matching the average of those found on the RIS. As such the geometry does not exactly match that of the RIS, notably it does not vary laterally, but represents an idealised configuration which generally compares to those found on a typical ice stream. A stress exponent of $m = 3$ was used. Following the methods in previous studies, a single value for the basal slipperiness was tuned in order to produce surface velocities of about $1\,\mathrm{m\,d^{-1}}$ [Gudmundsson, 2007, 2011, King et al., 2010, Walker et al., 2012].

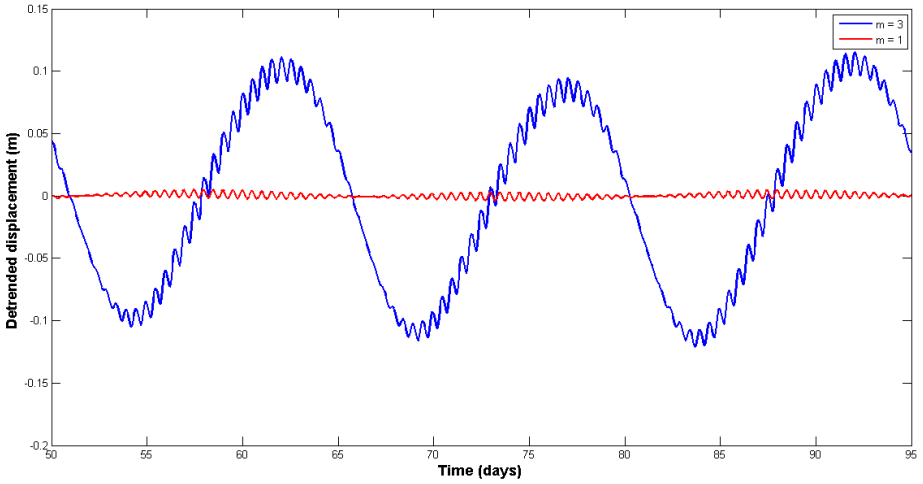

FIGURE 5.2: De-trended in-line displacements 11 km upstream from the grounding line for $m = 1$ (red curve) and $m = 3$ (blue curve) showing absence of any long period modulation in flow for a linear sliding law.

The de-trended horizontal displacements in Fig. 5.1 show that the ice stream response, when forced with semi-diurnal tidal periods, is dominated by the M_{sf} period (Table 4.1). Furthermore, this effect becomes more pronounced higher upstream such that the semi-diurnal modulation of displacements disappears almost completely by 30 km upstream of the grounding line. These results match those of Gudmundsson [2011] and strengthen the hypothesis that the long period modulation of ice stream velocities is a result of a non-linear basal sliding law but in this study including lateral effects for the first time. Figure 5.2 compares de-trended displacements for $m = 1$ and $m = 3$ and clearly demonstrates that when the model is forced with a stress exponent of 1 this long period effect does not occur.

Figure 5.3 shows the results of a similar experiment which used a geometry and tidal forcing similar to those of the Siple coast ice streams rather than the RIS. The tide in this region is dominated by diurnal (K_1 and O_1) rather than semi-diurnal constituents and with lower amplitudes than around the RIS. This time the ice stream responds to diurnal forcing with M_{f} frequency modulation in horizontal de-trended displacements, however it does not dominate as strongly as the M_{sf} did for semi-diurnal forcing. Note that the scale is different and the M_{f} signal 31 km upstream of the grounding line has an amplitude of only ~ 1 cm. This amplitude

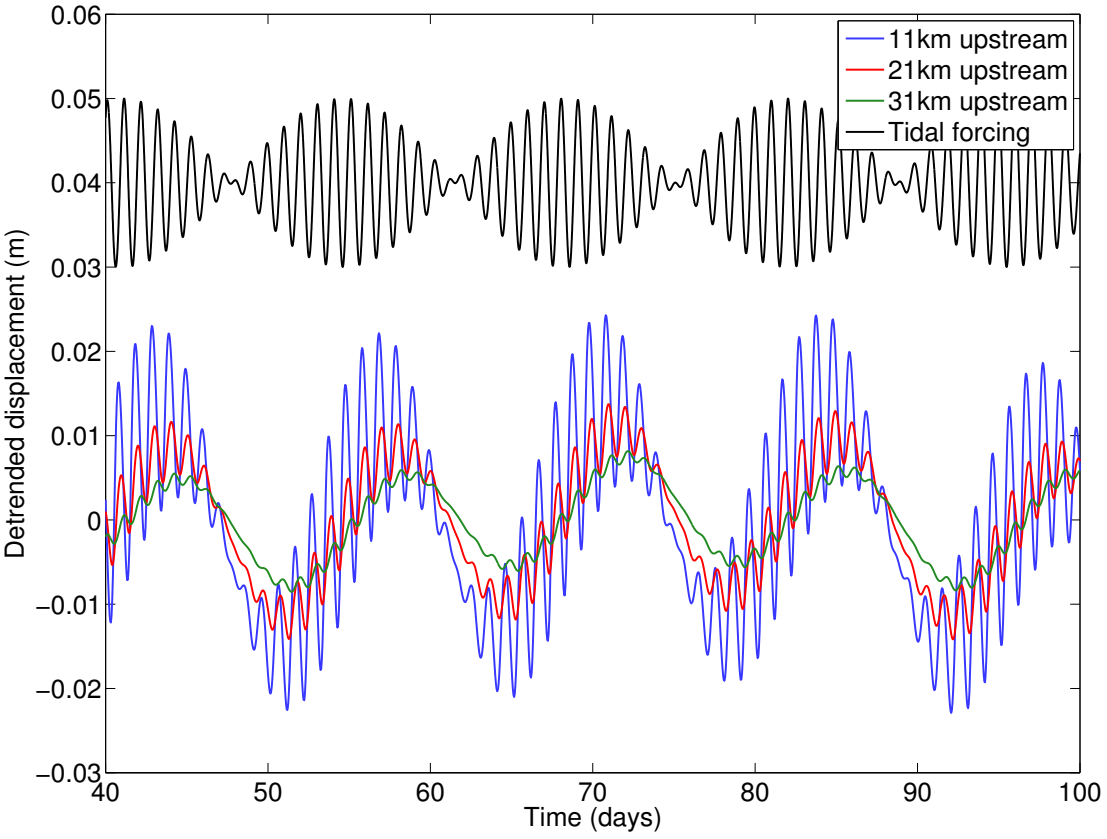

FIGURE 5.3: De-trended in-line displacements at 11, 21 and 31 km upstream of the grounding line for the 3D model run using an idealised Siple coast geometry. The tidal forcing is also shown, scaled down by a factor of 100 and shifted vertically.

is too small to be measureable using current GPS techniques. This suggests that M_{f} amplitudes on the Siple coast ice streams are expected to be small and difficult to measure, and about an order of magnitude less than the M_{sf} signal found on the Filchner-Ronne ice streams. The short period diurnal modulation of ice-stream flow is relatively large in comparison the RIS simulations forced with a diurnal tide. This is a consequence of the time dependant response of the ice stream to a periodic forcing as explained in the next section.

5.2 Tidal Analysis

A run using an identical model geometry and parameters as that shown in Fig. 5.1 was done but including values for all major tidal constituents (those with amplitudes greater than 5% of the M_2) around the RIS with amplitudes obtained from the CATS2008 tidal model [Padman et al., 2008]. Subsequently, tidal analysis was done on these results using the t_tide MATLAB package [Pawlowicz et al., 2002a]. I use this slightly different forcing in order to show that the M_{sf} signal arises from a realistic tidal forcing as well as the more simplified forcings used previously. Figure 5.4 shows the calculated amplitude (panel a) and phase (panel b) of the M_{sf} tidal constituent upstream of the grounding line. The phase is almost constant apart from very close to the clamped side wall whereas amplitude decreases gradually and has not reached an apparent maximum even 30 km away from the boundary.

As with previous studies I find that the nonlinearity of the tidal response leads to a shift in mean velocity [Gudmundsson, 2011, King et al., 2010]. For the simulation described above, forcing the domain with tides increases the mean velocity by about 3% when compared to a run with no tides. This represents a similar or slightly smaller effect than that seen in previous work, a reduction may be expected since the model presented here includes lateral effects and the M_{sf} amplitude produced is smaller.

Since the model being used is fully three-dimensional it is worth examining how the characteristics of the ice stream vary laterally. Velocities do not vary considerably in the lateral direction for the central half of the ice stream but decay rapidly approaching the sidewall, reaching 20% of the medial line value 2 km from the fixed boundary. The diagonal components of the stress tensor vary only slightly laterally however shear stress does change as would be expected. A convenient measure of the shear stress is the maximum principal shear stress which is constant in the middle of the ice stream but then increases linearly towards the boundary, reaching a maximum that is almost double the medial line stress.

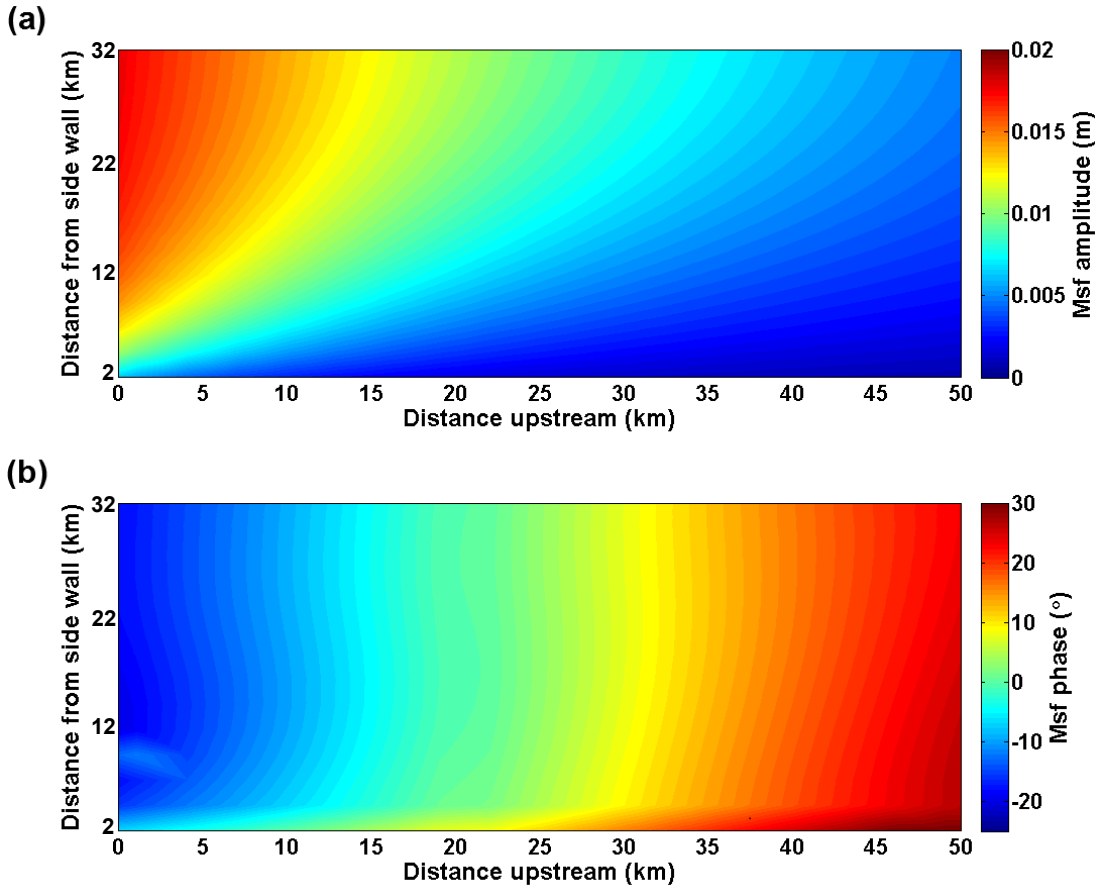

FIGURE 5.4: Plots showing amplitude (panel a) and phase (panel b) of the M_{sf} tidal constituent based on tidal analysis of de-trended horizontal surface displacement.

5.3 Linearized Experiments

The model presented here provides an opportunity to investigate the effects of different forcing frequency on ice stream flow and stress transmission upstream of the grounding line. Figure 5.5 shows the change in amplitude upstream of a grounding line for a simple sinusoidal boundary forcing with a range of frequencies. For these simulations the frequencies used at the boundary were not of a tidal nature, instead the ocean boundary was forced with a systematic spread of periods to get a clearer picture of the effect on an ice stream. In addition, ice rheology and the flow law were linearised in order to make a comparison between model results and the expected response from simplified equations (see section 5.4 for more details). Amplitude is normalised and plotted on a log scale for clarity.

Both amplitude and phase are shown to depend on the frequency of the forcing when the period is small compared to the Maxwell timescale. In all cases the horizontal velocity amplitude response decays exponentially but at short forcing periods the rate of decay is a function of the period while for longer forcing periods the curves converge to one solution. A run was also done with a forcing period of 32 days but it has not been plotted here for the sake of clarity since it lies on top of the curve of $T = 16$.

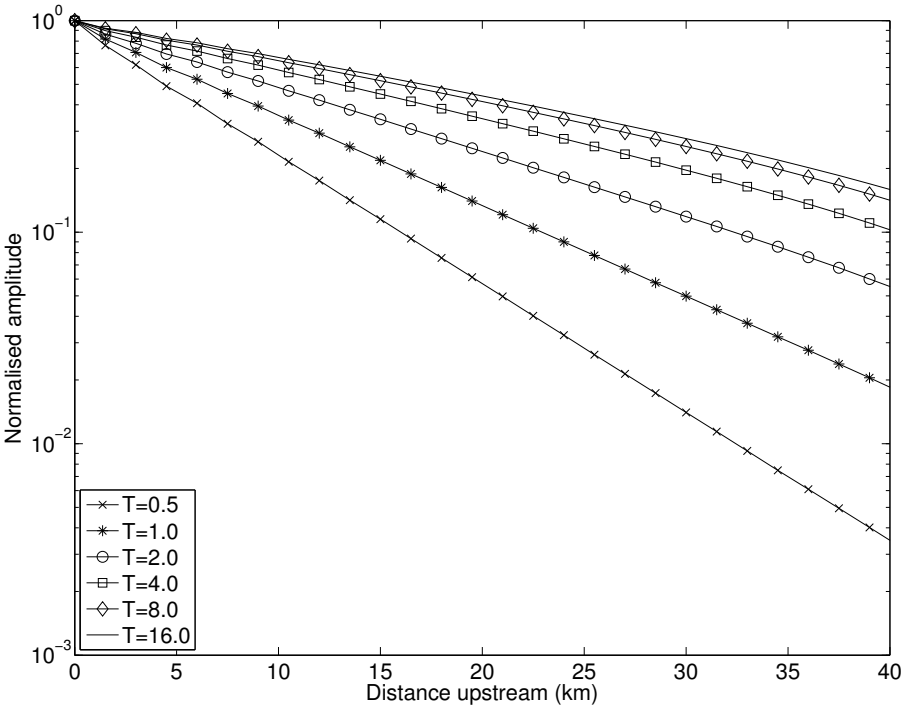

FIGURE 5.5: Normalised amplitude response to various periods (in days) of boundary forcing as a function of distance upstream as calculated by the model. Model parameters used were: A = $4.0^{-7}\mathrm{d}^{-1}\mathrm{kPa}^{-1}$, m = 1, n = 1, E = 3GPa, ν = 0.45 and a value for the rate factor in the till to produce surface velocities of $\sim 1\,\mathrm{md}^{-1}$. Note that amplitude is plotted on a log scale.

5.4 Stress-coupling length scale

Based on the results of the linearised model shown in Fig. 5.5, it is clear that the different responses at semi-diurnal, diurnal, M_{sf} and M_{f} frequencies are expected. When the model is forced systematically with a range of different periods,

a clear relationship appears between the stress-coupling length scale of the signal amplitude upstream of the grounding line and the ocean boundary condition period. Deviations from the mean horizontal flow decay exponentially for periods of a few days. For longer periods, this relationship breaks down and appears to be approaching a limit at $T = 16$ days. The cause of this lies in the viscoelastic rheology of the model; at short loading periods the ice behaves purely elastically but at longer periods the ice is dominantly viscous, at which point loading period has no effect. This transition from dominantly viscous to elastic can be related to the effective relaxation time of the Maxwell model λ (Eq. 2.18). Since $n = 1$ in these linearised runs, this is easily solved and gives a timescale of 1.2 days which matches well with the model results described above.

It is also possible to estimate the expected stress-coupling length scale in order to compare it with our results. I follow a similar method to Walters [1989], who adds small variations in velocity to the SSA (Eq. 2.13) to derive a length scale, but carry this further by making velocity a function of period. In these analytical expressions lateral effects are neglected.

The SSA (Eq. 2.13) can be written in terms of deviatoric stresses for the linearised homogenous case as

$$2\partial_x(h\tau_{xx}) - \tau_b + \rho g h \alpha = 0. \tag{5.1}$$

Assuming that h is not a function of x and using a basal drag relation of the form given in Eq. (2.23), but with $q = 0$ and $m = 1$, this becomes

$$2h\partial_x(\tau_{xx}) - \frac{u}{c} + \rho g h \alpha = 0, \tag{5.2}$$

assuming that the slip ratio is very high and thus basal sliding velocity is approximately equal to total ice-stream velocity. Along with this equation, Eq. (2.17) which contains both the viscous and elastic components of deformation, must be used to relate stresses and velocities.

The tidal component of this solution enters through u and τ_{xx}, which can be expanded so that they are formed of a mean ($\bar{u}$, $\bar{\tau}_{xx}$) and periodic perturbations

of amplitude $\hat{u}$, and $\hat{\tau}_{xx}$ respectively, giving

$$u = \bar{u} + \hat{u}e^{i(kx-\omega t)} \tag{5.3}$$

and

$$\tau_{xx} = \bar{\tau}_{xx} + \hat{\tau}_{xx}e^{i(kx-\omega t)}. \tag{5.4}$$

Note that the mean values $\bar{u}$ and $\bar{\tau}_{xx}$ are not functions of t or x, but constants. I will begin by deriving an equation for the simple purely viscous and purely elastic cases and then derive a full viscoelastic equation which reduces to these two when the forcing period is taken to its two limits.

5.4.1 Purely viscous length scale

Considering first the purely viscous case, Eq. (2.16) reduces to

$$\dot{e}_{xx} = \frac{1}{2\eta}\tau_{xx} \tag{5.5}$$

for $n = 1$, or in terms of the stresses

$$\tau_{xx} = 2\eta\dot{e}_{xx}. \tag{5.6}$$

Inserting this into Eq. (5.2) gives

$$4h\eta\partial_{xx}u = \frac{u}{c} \tag{5.7}$$

since $\dot{e}_{xx} = \partial_x u$. Using the expression for u from Eq. (5.3), considering only perturbations by neglecting the mean flow and evaluating the derivative leads to the following expression for k:

$$-4h\eta k^2 = \frac{1}{c} \tag{5.8}$$

The length scale of velocity perturbations is given by the inverse of k, thus

$$L_v = \sqrt{4h\eta c} \tag{5.9}$$

is the decay length scale of periodic perturbations in velocity for a purely viscous ice-stream.

5.4.2 Purely elastic length scale

The same approach can be used for a purely elastic ice-stream, whose rheology is described by

$$\dot{e}_{xx} = \frac{\dot{\tau}_{xx}}{2G}. \tag{5.10}$$

Evaluating the derivative on the RHS using the relation given by Eq. (5.4) gives

$$\dot{e}_{xx} = \frac{-i\omega\hat{\tau}_{xx}^{i(kx-\omega t)}}{2G}. \tag{5.11}$$

Rearranging and putting this back in terms of the total deviatoric stress results in

$$2G\dot{e}_{xx} = -i\omega(\tau_{xx} - \bar{\tau}_{xx}) \tag{5.12}$$

and thus

$$\tau_{xx} = \bar{\tau}_{xx} - \frac{2G\dot{e}_{xx}}{i\omega}. \tag{5.13}$$

Inserting this relation for the deviatoric stress into Eq. (5.2) results in

$$2h\partial_x\left(\bar{\tau}_{xx} - \frac{2G\partial_x u}{i\omega}\right) = \frac{u}{c}, \tag{5.14}$$

which simplifies to

$$4hG\left(\frac{\partial_{xx} u}{i\omega}\right) = \frac{u}{c} \tag{5.15}$$

since $\partial_x \bar{\tau}_{xx} = 0$. Now following steps identical to those used in deriving L_v ends in the following relation for k:

$$k = \sqrt{\frac{-i\omega}{4hGc}}, \tag{5.16}$$

Which for convenience I rearrange to give

$$k = \sqrt{\frac{1}{4hGc}}\sqrt{-i\omega} \tag{5.17}$$

Since $i\omega$ is a complex number of the form $a + ib$ (in this case with $a = 0$) its roots can be expressed as $\pm(\gamma + \delta i)$, where

$$\gamma = \sqrt{\frac{a + \sqrt{a^2 + b^2}}{2}} \tag{5.18}$$

and

$$\delta = sgn(b)\sqrt{\frac{-a + \sqrt{a^2 + b^2}}{2}}. \tag{5.19}$$

For $a = 0$ the roots are therefore

$$\gamma = \sqrt{\frac{|\omega|}{8hGc}} \tag{5.20}$$

and

$$\delta = -\sqrt{\frac{|\omega|}{8hGc}}. \tag{5.21}$$

Now substituting this complex expression for k into Eq. (5.3) gives

$$\hat{u}e^{i[(\gamma+i\delta)x-\omega t]} \tag{5.22}$$

which can be split up into a complex wave part $e^{i(-\gamma x-\omega t)}$ and a real decay part $e^{-\delta x}$. The length scale is given by $1/\delta$ and thus

$$L_e = \sqrt{\frac{8hGc}{|\omega|}}, \tag{5.23}$$

whereby the sign is positive due to the i^2 term arising in Eq. (5.22).

5.4.3 Viscoelastic length scale

Now I use the full Maxwell equation (2.17) including viscous and elastic terms which, after rearranging and evaluating the time derivative in the elastic term, becomes:

$$2\eta\dot{e}_{xx} = -i\omega\lambda\hat{\tau}_{xx}e^{i(kx-\omega t)} + \tau_{xx}. \tag{5.24}$$

Once again I use Eq. (5.4) to express τ_{xx} as the total and mean component, and factoring out I get

$$2\eta\dot{e}_{xx} = \tau_{xx}(1 - i\omega\lambda) + \bar{\tau}_{xx}i\omega\lambda, \tag{5.25}$$

or in terms of τ_{xx}:

$$\tau_{xx} = \frac{2\eta\dot{e}_{xx}}{(1 - i\omega\lambda)} - \frac{\bar{\tau}_{xx}i\omega\lambda}{(1 - i\omega\lambda)}. \tag{5.26}$$

Once again this is plugged into Eq. (5.2), giving

$$2h\partial_x\left[\frac{2\eta\dot{e}_{xx}}{(1 - i\omega\lambda)} - \frac{\bar{\tau}_{xx}i\omega\lambda}{(1 - i\omega\lambda)}\right] = \frac{u}{c}, \tag{5.27}$$

and since the second term of Eq. (5.26) does not depend on x, evaluating the derivative leads to another complex expression for k:

$$k^2 = \frac{(i\omega\lambda - 1)}{4h\eta c}. \tag{5.28}$$

Following the method already used to derive the elastic length scale, I find the roots of k to be

$$\gamma = \sqrt{\frac{-1 + \sqrt{1 + (\omega\lambda)^2)}}{2}} \tag{5.29}$$

and

$$\delta = \sqrt{\frac{1 + \sqrt{1 + (\omega\lambda)^2)}}{2}}. \tag{5.30}$$

Thus, the viscoelastic length scale in terms of E is given by

$$L_{ve} = \sqrt{\frac{8h\eta c}{1 + \sqrt{1 + (\omega\lambda)^2)}}}, \tag{5.31}$$

and the phase velocity is

$$\nu_p = \frac{\omega}{\gamma}. \tag{5.32}$$

The two limiting cases appear in Eq. (5.31) such that as $\omega \to 0$ (for very long periods), it simplifies to the purely viscous length scale (Eq. 5.9), and for $\omega \gg 1$ the dependance on viscosity disappears to give the purely elastic length scale (Eq. 5.23). The derivations of these stress-coupling length scales are simple for a Maxwell rheology because elastic and viscous strains can be related by $\epsilon_{\text{total}} = \epsilon_{\text{viscous}} + \epsilon_{\text{elastic}}$.

The length scale L determines how a perturbation in any of the field variables (i.e. velocity, strain, stress) decays with distance. This effect is due to transmission of stresses within the viscoelastic body, which in our model is instantaneous (in reality limited by the seismic velocity of ice and till). The length scale is, hence, not related to mass redistribution of ice with time that gives rise to a number of further length scales (e.g. Gudmundsson, 2003). I will refer to L_{ve} as the (viscoelastic) stress-coupling length scale.

Crucially, a time derivative only appears in the elastic contribution to deviatoric strain; it is from this that the stress-coupling length scale becomes a function of period whereas, for a purely viscous material, there is no dependence on forcing period.

A plot comparing forcing period with the three linearised length scales calculated above, along with the modeled length scale, is shown in Fig. 5.6a (black lines). This shows that the modeled length scale agrees well with the elastic solution at short forcing periods, then deviates at longer periods approaching an asymptote for $T \gg \lambda$. The derived full viscoelastic solution provides a good fit with the modeled results.

Walters [1989] fitted data from an Alaskan tidewater glacier on amplitude decay with distance from grounding line to a purely viscous version of the stress-coupling scale similar in form to Eq. (5.9). While the comparison made in that study provided a good agreement to observations, the author effectively chooses a value of

η that produced best fit to data, and since the decay is known to be exponential, it is not unexpected that a good fit is obtained. Regardless, the same method cannot be used for forcing periods similar to or smaller than the Maxwell timescale. As has been shown, the stress-coupling length scale at these periods strongly depends on the period and either the purely elastic or full viscoelastic stress-coupling length scale should be used.

A length scale can also be calculated for a nonlinear sliding law where $m \neq 1$. In this case, the basal stress term in Eq. (5.2) is raised to the power of $\frac{1}{m}$. This does not add any additional complication to the equations, and the length scale becomes

$$L = \sqrt{\frac{8\,h\eta m\,c^{1/m}\,\bar{u}^{1-1/m}}{1+\sqrt{1+(\omega\lambda)^2}}}. \tag{5.33}$$

It is easy to see that this equation reduces to the linear length scale equation for $m = 1$, but for $m = 3$ the effect is an increase in the stress-coupling length scale compared to the linearised case. The model was run again with the same range of forcing periods as discussed above for two new scenarios: (a) a nonlinear sliding law but retaining the assumption of linear homogeneous rheology ($m = 3, n = 1$) and (b) a nonlinear sliding law and nonlinear rheology ($m = 3, n = 3$). Model results for the two new scenarios are plotted in red and blue for cases (a) and (b) respectively in Fig. 5.6 along with the derived nonlinear stress-coupling length scale given in Eq. (5.33).

As expected, the length scales for the case where $m = 3$ and $n = 1$ are considerably longer than the fully linearised runs and agree well with the derived nonlinear stress-coupling length scale. For the range of parameters explored, the change in length scale from $m = 1$ to $m = 3$ is much greater than the change from $n = 1$ to $n = 3$, suggesting that the assumption of linear rheology in Eq. (5.33) does not have a large effect. Note that a similar study by Thompson et al. [2014], looking at stress transmission for a narrower ice stream configuration than the one presented in this chapter, showed much smaller length scales and proposes an alternative mechanism for stress transmission which I will discuss in chapter 6.

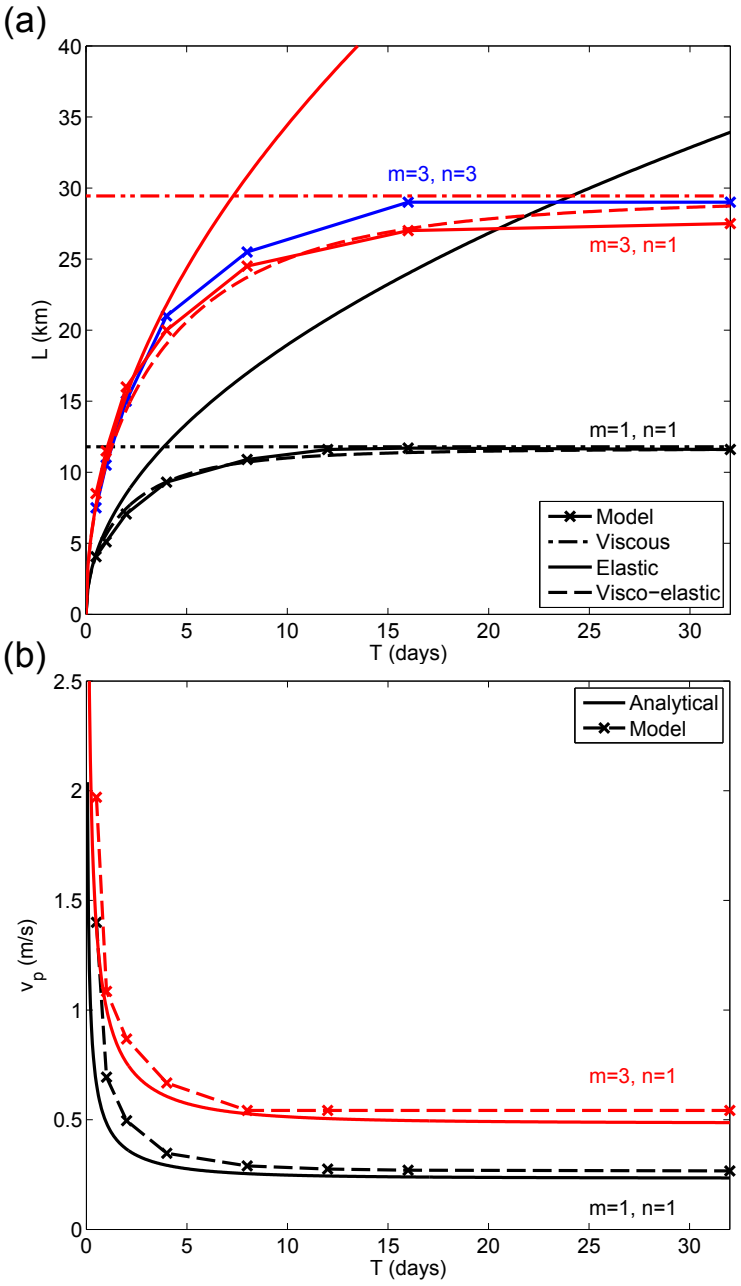

FIGURE 5.6: Comparison of analytical solutions for stress-coupling length scale (panel **a**) and phase velocity (panel **b**) with model results. Solutions and results for linearised runs are shown in black, semi-nonlinear runs in red and fully nonlinear runs in blue. In panel **(a)** the solid and dot-dashed lines are the purely viscous and elastic length scales respectively as derived from the linearised SSA, and the dashed line is the combined viscoelastic response. The modelled length scales are the solid lines marked with crosses representing a model run for that given loading period. In panel **(b)** the phase velocity in the model (dashed line) was calculated by a least squares fit and compared to the analytical solutions.

Phase velocities were calculated for each forcing period for linearised (black line) and semi-nonlinear (red line) cases using the t_tide package to give the phase

of each constituent at each point on the surface of the ice and the change in phase was used to calculate phase speed. The results are compared with the analytical solutions in Fig. 5.6b. The phase velocities calculated from the model agree reasonably well with the analytical solutions, although they appear to be slightly overestimated particularly at short forcing periods. Some difference might be expected however since the equations have been derived from the SSA and the model is solving the full Stokes solution. As with the stress-coupling length scale, the phase velocities for $m = 3$ are increased compared to $m = 1$.

5.5 Discussion

Previous modelling studies have successfully reproduced long-period modulation of ice stream flow by forcing their models with only semi-diurnal and diurnal tidal constituents and using a nonlinear basal sliding law [Gudmundsson, 2007, 2011, King et al., 2010, Walker et al., 2012]. A strong criticism of this previous work is that they neglect lateral effects and therefore are missing a key dampening process that would alter this result. Work in this chapter demonstrates that extending to 3D and including lateral effects does not alter this result and that the effect on ice stream flow is qualitatively the same, strengthening the hypothesis that a sliding law with $m > 1$ is required.

For an idealised geometry of a typical ice-stream and semi-diurnal forcing, the model produces a clear M_{sf} frequency (Fig. 5.1) matching observations made in this area. When forcing the model with a geometry more typical of the Siple coast and diurnal tides, the long-period modulation remains but some features of the response are quite different (see Fig. 5.3). Firstly, the long-period response is at M_{f} frequency, as would be expected from a combination of K_1 and O_1 tidal constituents. In addition, the diurnal signal remains relatively strong even far upstream of the grounding line, but the overall amplitudes for both long and short-period motion are much smaller than the previous case. The amplitude of only $\sim 1\,\mathrm{cm}$ is too small to be measurable using current GPS techniques. We

therefore conclude that M_{f} amplitudes on the Siple coast ice streams are expected to be small and difficult to measure, and about an order of magnitude less than the M_{sf} signal found on the Filchner–Ronne ice streams.

Previous studies cite a single value for the phase velocity of tidal forcing travelling upstream of an ice stream grounding line, but these results show that phase velocity strongly depends on the forcing period up to a limit where $T \gg \lambda$. The semidiurnal tidal constituents have periods of approximately half a day and based on these results have a phase velocity of $1.45\,\mathrm{ms}^{-1}$ whereas the longer-period *Mf* and *Msf* constituents have periods of around a fortnight and would have a phase velocity of $0.27\,\mathrm{ms}^{-1}$. The range of values for phase velocity calculated here agree with the range of values typically found in the literature (e.g. Gudmundsson [2007], Murray et al. [2007]); however, since most of these studies make it unclear how it has been calculated or which constituent they are considering, it is difficult to make a direct comparison.

The fact that the results shown in Fig. 5.5 match the derived analytical stress-coupling length scale helps to verify the numerical model and gives increased confidence in the accuracy of these numerical results. The analytical solution also shows, for the first time, directly how phase and amplitude of the tidal response vary with distance upstream from the grounding line. This result also emphasises once again the importance of a correct value for m in getting realistic stress transmission along an ice stream.

5.6 Chapter Summary

1. The MSC.Marc model is used to try and produce a modulation in ice-stream flow at M_{sf} frequency arising from a forcing at M_2 and S_2 period as has been observed in Antarctica.

2. In agreement with previous 2D work, the model successfully reproduces long period modulation as a result of nonlinearity arising from using $m > 1$ in the sliding law.

3. Further analysis of modeled ice stream flow shows a varying stress-coupling length scale of boundary effects upstream of the grounding line.

4. I derive a viscoelastic stress-coupling length scale from ice stream equations that depends on the forcing period and closely agrees with model output.

Chapter 6

3D coupled model results

This chapter is based on a manuscript entitled "Temporal variations in the flow of a large Antarctic ice-stream controlled by tidally induced changes in the subglacial water system", submitted to the Cryosphere and published online in the Cryosphere Discussions on 14$^{\text{th}}$ of April 2015 [Rosier et al., 2015].

6.1 Introduction

To date no model has been presented that matches the RIS tidal observations. Admittedly, most models have focused on trying to identify the mechanism responsible for the striking observation that the response of the ice-stream is concentrated at tidal frequencies absent in the forcing. However, it would be expected that if the mechanism has been correctly identified, and is the primary cause for the velocity fluctuations, modeled amplitudes would be close to those measured. In fact modeling work presented so far has always produced too small a response at the M_{sf} tidal period, and too strong at both diurnal and semi-diurnal periods. The model presented in chapter 5 succeeds in reproducing qualitative aspects of the observed M_{sf} effect, but the amplitude of $\sim$ 0.05m near the grounding line (Fig. 5.1) is far less than the observed amplitude of $\sim$ 0.3m (Fig. 1.2).

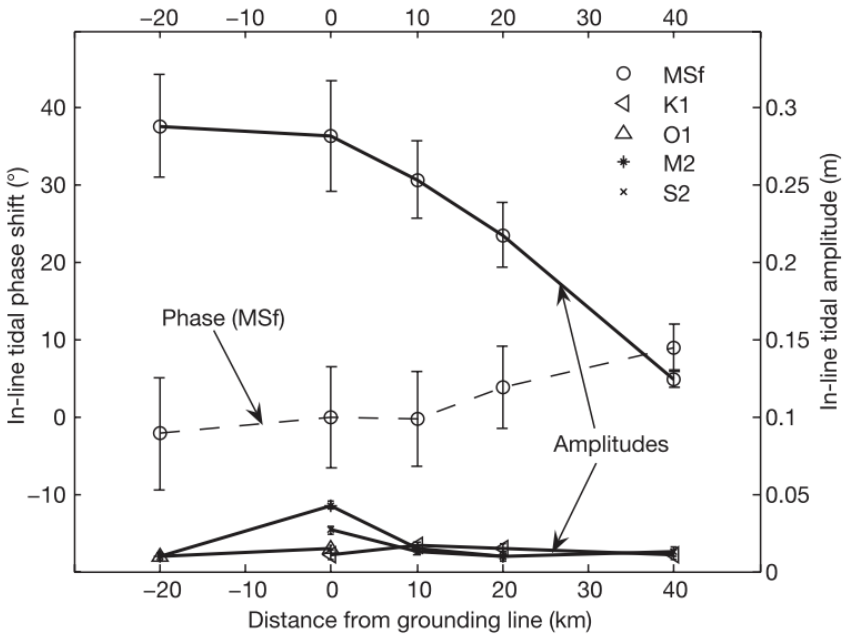

FIGURE 6.1: Amplitude and phase of various tidal constituents as observed from detrended GPS measurements made on the surface of RIS. The error bars show 95% confidence intervals calculated in t_tide. Taken from Gudmundsson [2007].

In this chapter, I begin by conducting a parameter study of the 3D model presented in chapter 5, to determine whether there is any way to produce the desired amplitudes through the nonlinear basal stress relation mechanism set out in that chapter and previous work by Gudmundsson [2007, 2011]. Subsequently I add a coupling to tidally induced perturbations in basal water pressure, as described in Section 3.4 and first proposed by Thompson et al. [2014]. The tidal forcing for all simulations in this chapter is the full forcing which includes the constituents and amplitudes set out in Table 3.1.

Since the goal of this chapter is to match the observations made on the RIS, it is worth reviewing those measurements. Figure 6.1 shows measured amplitude and phases of the main tidal constituents observed on the RIS taken from detrended GPS measurements on the surface [Gudmundsson, 2007]. The main aim is to match the large amplitude and slow decay of the M_{sf} signal upstream from the grounding line, but also the relatively small amplitude of the semidiurnal tidal constituents upstream. At the grounding line the M_{sf} amplitude is ~ 0.28m and

the M_2 amplitude is ~ 0.05m while 40km upstream these decay to ~ 0.12m and ~ 0.01m respectively.

6.2 3D ISS model parameter study

To address the open question of whether RIS observations can be replicated through stress transmission alone, my first modeling aim in this chapter is to establish an upper bound on the possible M_{sf} amplitude in the absence of any temporal changes in bed conditions, i.e. other than those resulting from direct stress transmission through the ice due to the flexing of the ice in response to tides. In the context of the modeling methodology described in chapter 3 this is equivalent to setting the effective pressure exponent, q, of the sliding law (see Eq. 2.23) to zero. In effect I repeat the fully 3D simulations conducted in chapter 5 but with a broader range of parameters, an ice-stream geometry closer to that of RIS and a basal slipperiness distribution ($c'(x)$) determined through a formal inversion of surface velocities. The tunable model parameters with no subglacial hydrological coupling are: the Poisson's ratio (ν), the Young's modulus (E), and the stress exponent (m). I set the stress exponent (n) in Glen's flow law to $n = 3$, and determine the rate factor A from a static temperature distribution defined in the model using the commonly used temperature relation given in Section 2.3.

I performed an extensive parameter study. For every value of the basal sliding-law stress exponent m, I first determined the maximum a posteriori distribution of basal slipperiness (c') using the inversion approach outlined in Section 3.7. In the surface-to-bed inversion the long-term average flow in the absence of tidal forcing was matched to the observed velocity, and a (purely) viscous flow model was therefore used in the forward step. I then forced the visco-elastic time-dependent model by tides. For each given value of m and the associated basal slipperiness distribution, tidal response was calculated for a range of elastic rheology parameters. From modeled horizontal displacements curves, I then calculated tidal amplitudes

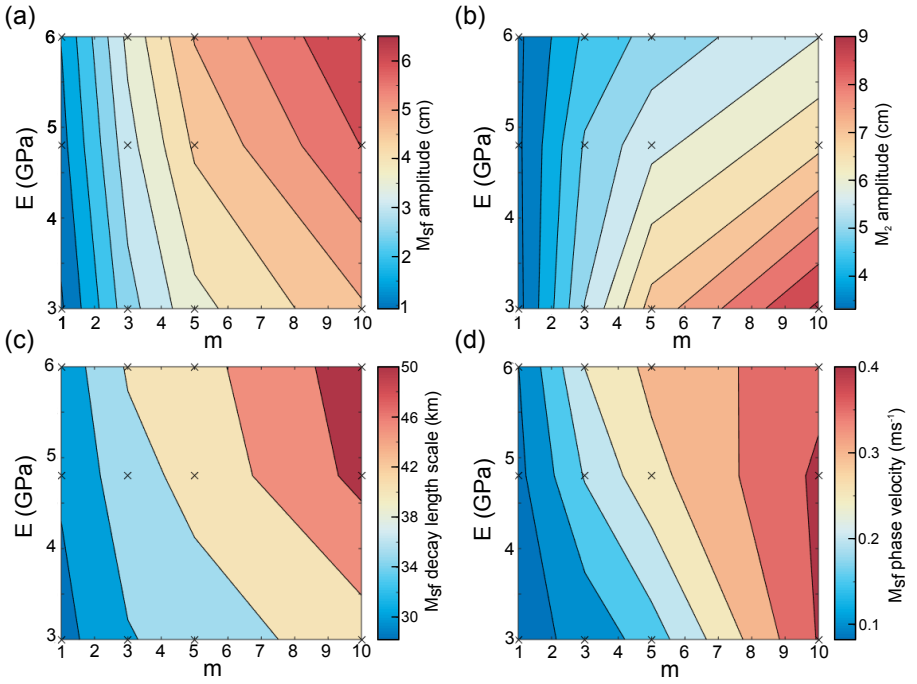

FIGURE 6.2: Modelled M_{sf} and M_2 tidal amplitudes 10 km upstream from the grounding line (panels a and b, respectively), and M_{sf} decay length scales and phase velocities (panels c and d, respectively) as a funciton of the basal sliding law stress exponent m and the elastic Young's modulus (E) of ice. Here the potential effects of subglacial water pressure variations in response to tides on sliding were not included, i.e. in the sliding law (Eq. 2.22), $q = 0$. Crosses indicate model simulations. The contour plot is based on interpolation of model results.

and phases as a function of distance along the medial line. By fitting an exponential curve to the spatial variation in tidal amplitudes, I then determined decay length scales for each tidal component, as well as phase velocities. I varied the stress exponent m from 1 to 10, and the Young's modulus from 1 to 6 GPa. The Poisson's ratio was varied between 0.3 to 0.45, but was found to have almost no effect on the modeled tidal response and I do not discuss those results further.

The results of the parameter study are summarized in Fig. 6.2. In panel (a) of Fig. 6.2 the amplitude of the M_{sf} frequency 10 km upstream from the grounding line is shown. The modeled M_{sf} amplitudes are never larger than a few centimeters. The largest values are found for high m and high E values. Although somewhat higher M_{sf} amplitudes could be obtained by increasing m even further, the modeled results show that this increase is sub-linear as a function of m. Furthermore, for $m > 10$ other model outputs that must match observations such as phase velocity,

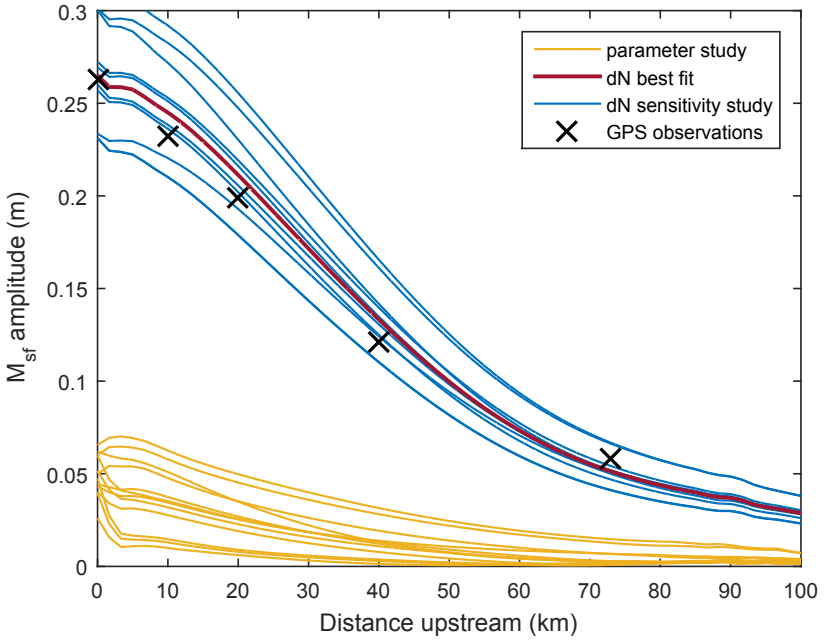

FIGURE 6.3: M_{sf} amplitude as a function of distance upstream for parameter study simulations with no hydrology (yellow), compared with GPS measurements (crosses), all results from the coupled model sensitivity study (blue) and the coupled model best fit to GPS data (red).

decay length scale and notably M_2 amplitude, would also increase beyond the range of desired values. The model is, thus, not able to reproduce the observed magnitude of the M_{sf} tidal amplitude.

Both the decay length scale (Fig 6.2c) and phase velocity (Fig 6.2d) increase with increasing m, in agreement with the analytical solution derived in Section 5.4.

The amount of buttressing needed to match observed velocities increases as m is increased and varied from 650KPa to 850KPa for $m = 1$ to 10. Note that the inversion procedure, in minimising the cost function, tries to find a solution that does not vary significantly from the a-priori estimates of slipperiness and buttressing, and therefore this buttressing value may be to some extent artificial if the a-priori buttressing estimate and error are poorly chosen. For this reason a large value (1000kPa) is chosen for the error estimate of buttressing used in the inversion.

Decay of the M_{sf} amplitude upstream of the grounding line for all parameter

study simulations is plotted in Fig. 6.3 (blue lines) and compared with the observed amplitudes (crosses). This clearly shows the disparity between desired amplitude and the range of possible amplitudes using the mechanism described above. The conclusion from this parameter study, in agreement with Thompson et al. [2014], is that stress transmission alone cannot explain the large amplitude of M_{sf} modulation, with maximum amplitudes 10 km upstream approaching ~ 0.05 m, considerably smaller than the desired 0.3 m. Clearly an additional nonlinear effect is needed to match observations. Although stress-transmission can reproduce the qualitative aspects of the data, in particular the generation of M_{sf} response, the effects are (at the most) about an order-of magnitude smaller than revealed by measurements.

6.3 3D coupled model results

In this section I couple the hydrological model (section 3.4) to the 3D full-Stokes model by using values of $q > 0$ in order to investigate whether this can explain measurements made on the RIS.

Coupled model results obtained through optimization of hydrological parameters are shown in Fig 6.4. An informal optimization was done, whereby the values were changed iteratively until the model response agreed well with the observed tidal effects. These results provide a much better agreement with GPS measurements than any previous combination of parameters for the model with no subglacial water pressure coupling. Notably, the M_{sf} amplitude and decay length scale are both large and match very closely with data (Fig 6.3). The hydrological model used a mean effective pressure ($\overline{N}$) of 105kPa, pressure exponent (q) of 10 and diffusivity (K) of $7 \cdot 10^9 m^2 d^{-1}$. Other model parameters were $E = 4.8$GPa, $\nu = 0.41$ (both in accordance with the optimum Maxwell rheology given by Gudmundsson [2011]) and $m = 3$.

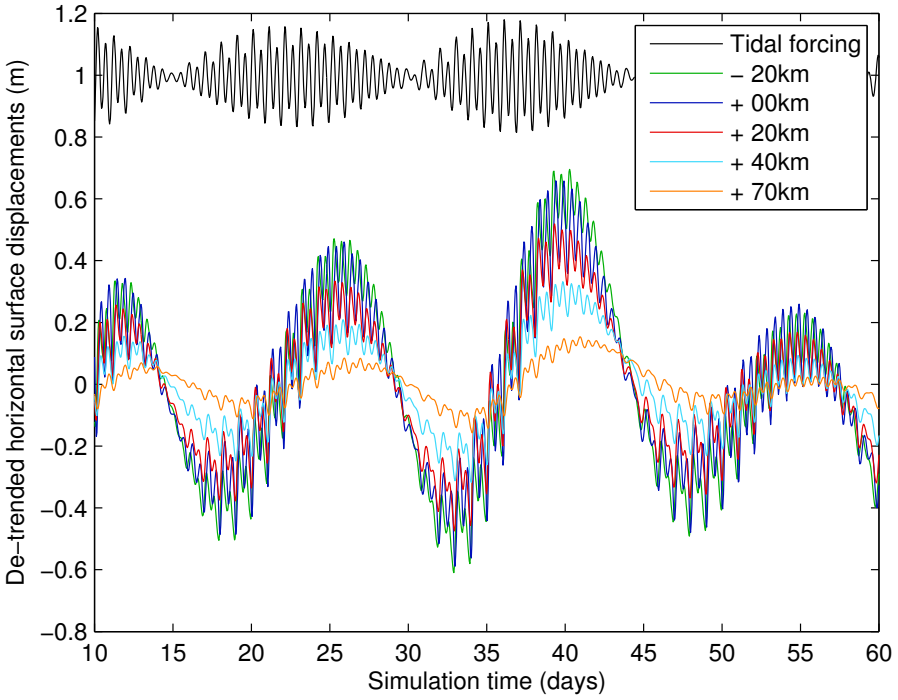

FIGURE 6.4: Modelled detrended horizontal surface displacements taken along the ice-stream medial at 20 km downstream (-20 km), at the grounding line (+00 km) and distances of 20, 40 and 70 km upstream of the grounding line (+20, +40 and +70 km respectively). The model was forced with $\bar{N} = 105$ kPa, K $= 7 \times 10^9 m^2 d^{-1}$, q $= 10$, m $= 3$, E $= 4.8$ GPa and $\nu = 0.41$

Figure 6.5 shows snapshots of the hydraulic head upstream of the grounding line at various points in the tidal cycle for the diffusivity used in Fig. 6.4. This demonstrates the high diffusivity being used in this simulation and how far upstream perturbations in water pressure must travel. Note that the subglacial drainage system domain is 200 km long, and so a further 100km further than shown in this plot which only shows the portion of the drainage system beneath the modeled ice-stream.

The only feature of these results that is arguably not in agreement with observations is the amplitude of the semidiurnal tidal constituent de-trended displacements. Comparison between Figs. 1.2 & 6.4 shows a modeled M_2 amplitude that is approximately twice as large at the grounding line as the amplitude determined by tidal analysis of the data. Possible explanations for this are that the M_2 amplitude may be too small to be sufficiently resolved by the GPS receivers that originally made the measurements or limitations of the simple Maxwell rheology. Errors

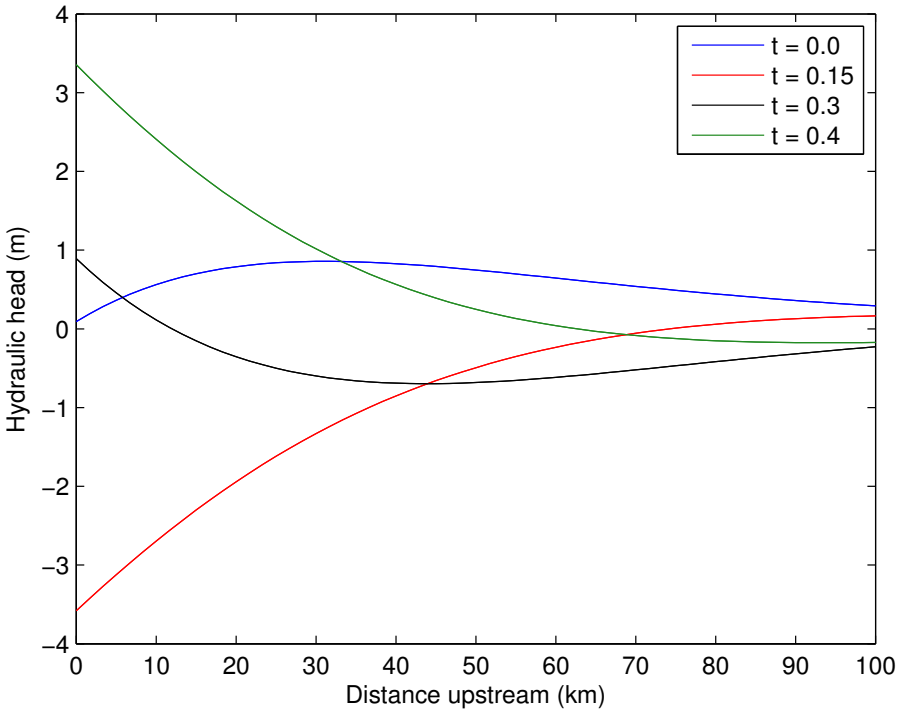

FIGURE 6.5: Hydraulic head (m) beneath the modeled ice-stream as a function of distance upstream of the grounding line, at selected points in the tidal cycle (t in days).

in the GPS measurements are of the order of centimeters; more details of the original dataset can be found in Gudmundsson [2006] and a description of similar processing in Dach et al. [2009].

I perform a sensitivity analysis to determine whether the M_{sf} response is robust or highly sensitive to certain parameters. Figure 6.6 shows change in M_{sf} amplitude (panel a), M_2 amplitude (panel b), M_{sf} decay length scale (panel c) and M_{sf} phase velocity (panel d) compared to the optimised model for a $\pm 10\%$ change in each parameter.

Comparison of panels a & b in Fig. 6.6 suggest that the calculated M_{sf} and M_2 amplitudes are closely correlated and thus, for the parameters tested here, there is no clear modification of the model that would decrease the semidiurnal (M_2) amplitude without also reducing the M_{sf} response. Softening the ice by reducing E may be one possible route, since this appears to increase M_{sf} amplitude more than M_2 amplitude, however this parameter is more tightly constrained than others since the rheology of ice is not entirely unknown and the sensitivity is too

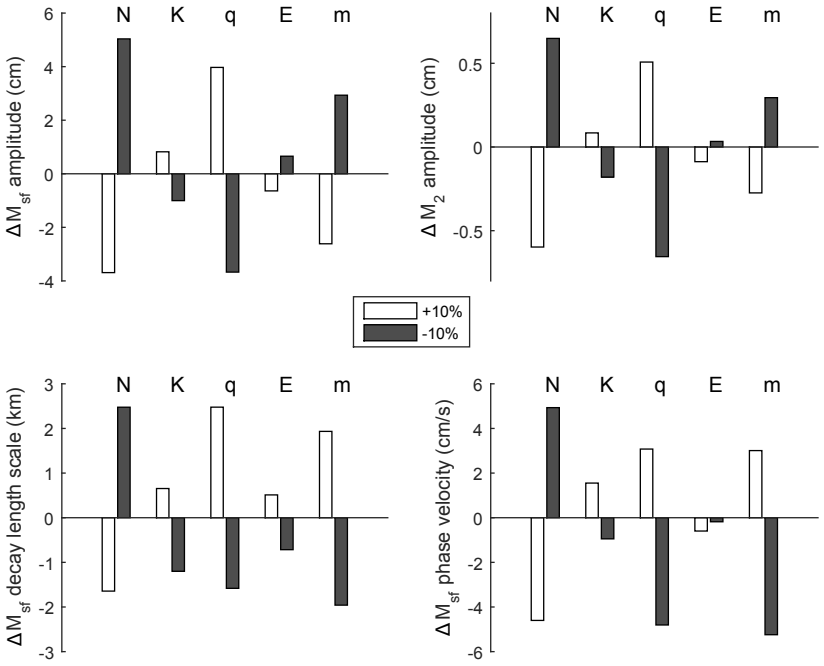

FIGURE 6.6: Sensitivity analysis of model parameters (N, K, q, E and m), showing change in M_{sf} and M_2 amplitudes (panels a & b), M_{sf} decay length scale (panel c) and M_{sf} phase velocity (panel d) for +10% (white bar) and -10% (grey bar) changes in each parameter. Model outputs were compared to the simulation presented in Fig. 6.4 and all other parameters were kept at the values defined in that plot.

small to solve the issue. M_{sf} amplitude is most sensitive to normalized changes in $\overline{N}$ and q, as might be expected since it is the nonlinearity here that drives the majority of the long period modulation in flow.

A reduction in m decreases the M_{sf} amplitude of the modeled ice stream, the reverse of the response with no hydrological coupling, but increases the M_{sf} length scale and phase velocity. Overall, all model outputs are most sensitive to the choice in $\overline{N}$. This is not surprising, since ΔN is small then as $\overline{N}$ gets large the dimensionless number ξ will drop out and that source of nonlinearity disappears.

The large difference in M_{sf} amplitude between the parameter study simulations and those that include tidally-induced subglacial pressure variation poses an important question; is a nonlinear sliding law where $m > 1$ required at all, given that the M_{sf} modulation appears to be largely generated by water pressure changes.

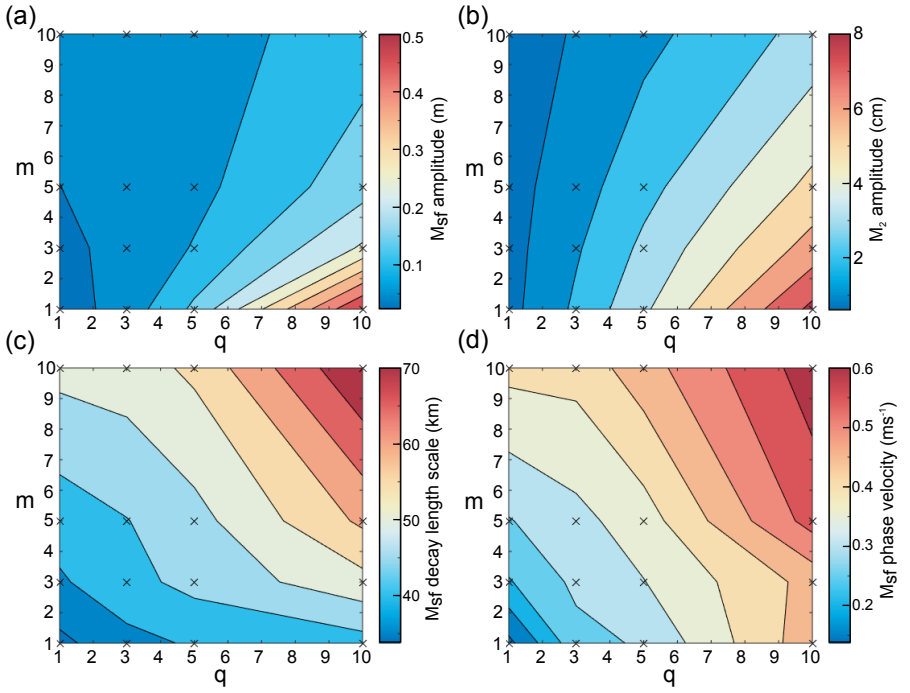

FIGURE 6.7: Response of M_{sf} amplitude (panel a), M_2 amplitude (panel b), M_{sf} decay length scale (panel c) and M_{sf} phase velocity (panel d) to choice of stress exponent (m) and hydrological exponent (q). Crosses indicate model simulations. M_{sf} and M_2 amplitudes were taken at 10 km upstream from the grounding line.

Results from the sensitivity analysis suggest that the stress exponent m remains a crucial parameter in altering characteristics of the M_{sf} response. To look at this in more detail, the model was rerun with varying exponents q and m, with the aim of examining the characteristics of the M_{sf} response given changes in the dominance of the two mechanisms.

The four characteristics of the model's tidal response are plotted against exponents q and m, each varying between 1 and 10, in Fig. 6.7. These results show that reducing m leads to an increase in amplitude of both tidal frequencies investigated, but a decrease in the length scale and phase velocity. An M_{sf} decay length scale of $\sim 50km$ is observed on the RIS but panel c shows that for $m = 1$ the length scale is smaller up to $q = 10$ and in fact appears to have reached an asymptote. Increasing m for any given value of q however leads to a large increase in the length scale. The mechanism by which increasing m reduces M_{sf} amplitude but increases length scale is discussed later but suggests that a flow low with $m > 1$ is still required to reproduce the RIS tidal response.

6.4 Discussion

I find that stress transmission alone cannot fully explain the observed M_{sf} modulation of surface velocities on the RIS. An additional mechanism whereby a tidally-induced pressure wave travels up a subglacial drainage system, altering the effective pressure at the base of the ice stream, is required to produce a sufficiently large M_{sf} amplitude. The drainage system must be highly conductive and sufficiently nonlinear, such that a small change in basal water pressure leads to a large change in surface velocity.

The darcian approach that is used should not be interepreted as a reflection that water is actually flowing through the porous till layer. The diffusivity (K), defined in Equation 3.9, is comprised of specific storage and hydraulic conductivity terms. Fountain and Walder [1998] give a review of till properties and from the values given it is possible to make a rough estimate of the range of possible diffusivities that might exist for a variety of till fabrics. Using a specific storage of $S_s \approx 10^{-4} m^{-1}$ and hydraulic conductivity of between 10^{-12} and 10^{-4} gives a diffusivity that is many orders of magnitude smaller than would be necessary to transmit a tidal signal far upstream of the grounding line, even if these values are themselves wrong by several orders of magnitude. It is for this reason that flow through the till is discounted as a mechanism and that the drainage system is described as highly conductive.

This nonlinearity arises largely in two of the parameters: $\overline{N}$ and q. The model does not take into account feedbacks between ice flexure and water pressure. Tidal flexure causes changes in normal stress which would perturb the subglacial water pressure and it has been suggested that this mechanism could 'pump' brackish water upstream [Sayag and Worster, 2013, Walker et al., 2013]. This flexure may have the additional effect of opening crevasses beneath the ice or dilating the subglacial till, leading to changes in local water storage and thereby altering the distribution of water. Our justification in ignoring these additional processes is that ice flexure is limited to within several ice thicknesses of the grounding line and the M_{sf} modulation is observed to travel much further upstream.

Spatial variations in $\overline{N}$ are accounted for in the inverted c' and cannot be separated from spatial variability in c. In reality if $\overline{N}$ varied spatially this would affect the nonlinearity in ξ. Ultimately we ignore this additional complication and the decay in ξ is only a function of the spatially uniform diffusivity, K. In doing so several processes are combined to provide a more general picture of the subglacial drainage characteristics. A fit to observations could to some extent still be obtained if $\overline{N}$ was altered by compensating with a change in q since the two parameters are correlated. In general though, a relatively low value of effective pressure with no large gradient going upstream from the grounding line is needed, since a gradient would cause the nonlinearity to be rapidly reduced in the upstream direction.

6.4.1 Measurements of effective pressure beneath ice streams

The results of the coupled 3D ISS model require generally low values of effective pressure beneath the ice-stream in order to perturb mean velocities sufficiently as a result of tidally induced subglacial pressure variations. As a result of this finding, it is worth briefly considering the likelihood of these values existing beneath an ice-stream based on available measurements of subglacial water pressure.

Measurements of effective pressure (N) beneath Antarctic ice streams are relatively sparse due to the challenging nature of accessing the bed of ice-streams that are several kilometers thick. Alley et al. [1986] inferred that the Whillans ice stream rests on an unconsolidated sediment in which the effective pressure is only 50kPa and suggested that deformation of this layer accounted for the majority the ice stream's motion. Boreholes drilled to the base of the same ice stream revealed the basal water pressure to be within 160kPa of the ice overburden pressure [Engelhardt et al., 1990].

The first observations in Antarctica that hinted at a possible link between the ocean tides, subglacial water pressure and ice stream velocity were made on the Whillans ice stream [Harrison, 1993]. Diurnal variations in strain rate and borehole water pressure were discovered $\sim$ 300km upstream of the grounding line which

could not attributed to changes in air temperature or atmospheric affects, and the tides under the Ross sea were put forward as a possible explanation.

A second set of borehole measurements on Whillans ice stream also found diurnal variation in the subglacial water pressure but the authors were reluctant to attribute this to the tides. They conclude that, since the signal seems to appear and disappear randomly and there is an apparent absence of M_f period modulation that is present in the tidal forcing, tides were unlikely to be driving the pressure changes, but no better alternative mechanism was proposed.

On the RIS, seismic surveys revealed potential changes in subglacial hydrology over short time scales inferred from changes in the acoustic impedance of bed material [Smith et al., 2007]. Unfortunately the three surveys included in the study were conducted several years apart and therefore it is not possible to say whether changes in the drainage system are occuring over the tidal time scales that we focus on here.

A possible analogy can be drawn between Antarctic ice streams and smaller tidewater glaciers where observations are generally easier, particularly for borehole measurements needed to investigate changes in subglacial pressure. Recent borehole measurements of a Patagonian tidewater glacier by Sugiyama et al. [2011] found that changes in basal water pressure of a few percent resulted in almost 40% of the measured variation in ice flow speed. Although the change in basal water pressure appears to be caused by fluctuations in air temperature rather than a tidal pressure wave the fact that small changes in pressure at daily timescales can have such a dramatic change on velocity is notable. The measurements suggest a highly plastic process where the ice is close to some threshold ($N \approx 0.95P_i$) and very sensitive to any pressure variation.

6.4.2 The form of the basal sliding law

In order to understand the interaction between the hydrology and stress transmission mechanisms it is important to consider the relative timing with which they act

on the ice-stream. As explained previously, an exponent $m > 1$ causes an increase in ice velocity during low tide and decrease at high tide. Conversely, at high tide near the grounding line the water pressure within the subglacial drainage system will be at its highest, lowering the effective pressure and increasing ice velocity. The two effects are therefore opposite in phase at the grounding line (although in both cases the peak velocities are still during the spring tide, so there is no phase shift in the M_{sf} frequency that they generate at this point). Since the subglacial pressure effect is larger (in this model, due to the low $\bar{N}$) it dominates at the grounding line and the reduction in M_{sf} amplitude at this point for $m > 1$ is a result of the stress transmission effect being 180° out of phase with the subglacial pressure variations, thereby dampening the velocity modulation.

Results from Fig. 6.7 suggest that, while it may be possible to reproduce the observed M_{sf} response of the RIS for $m = 1$, this would necessitate an almost infinite diffusivity in order to transmit the signal far enough upstream. With the set of model parameters presented, the effect of subglacial pressure variations dominates at the grounding line and can produce very large M_{sf} amplitudes, but what is much more difficult is to reproduce the long decay length scale of this frequency. The key parameter then becomes m, which can substantially increase the decay length scale given values $m > 1$. Any reduction in the M_{sf} amplitude from using a high value of m can be compensated for by increasing the nonlinearity of the drainage system (reducing $\bar{N}$ or increasing q).

None of the other parameters within the model had such a large effect on the length scale and the implication is that a nonlinear sliding law is required in addition to any nonlinear response to subglacial pressure variations. Matching the observed long period modulation of ice-stream flow requires a balance between large M_{sf} amplitude and decay length scale. A choice of m that is too small means the M_{sf} signal will decay too rapidly upstream of the grounding line, but too large and the generation of the signal due to subglacial hydrology becomes hindered.

An explanation for this increase in length scale with $m > 1$ can be thought of intuitively as follows. Consider the propogation of nonlinear M_{sf} period up the

RIS as two waves, generated by the upper and lower terms on the right of Eq. 2.23. These two waves clearly have the same frequency but since they propogate up the ice-stream by different mechanisms it is reasonable to assume they have different phase velocities. At x_{gl} they are 180° out of phase but with different phase speeds this destructive interference becomes constructive interference as you move away from the source. As a consequence the M_{sf} amplitude is reduced at the grounding line but it's decay may be slowed as a result of constructive interference upstream.

The requirement of high diffusivity in order to transmit the tidal signal far enough upstream to match observations suggests that there must be a channelized drainage system beneath the RIS. This could consist of a few large channels that transmit the tidal pressure wave far upstream which then permeates through the till on either side of the channel, leading to changes in effective pressure over large portions of the ice-stream base. Recent seismic observations of the RIS potentially support this hypothesis, finding that changes in aseismic dilatant till are responsible for most of the temporal variation in surface velocity and 'sticky spots' of stiffer till do not play a major role [Smith et al., 2015].

Gudmundsson [2011] demonstrated that the nonlinearity described above leads to an increase in the RIS mean velocity of $\sim$ 5% due to the presence of the tides. A simulation with identical model setup to that used in Fig 6.4 but with tidal amplitude set to zero everywhere was done to examine this process with the larger M_{sf} amplitudes presented in this work. The result with this new model, that successfully replicates the amplitude of long period modulation, is that mean surface velocity at the grounding line is increased by $\sim$ 12% due to the presence of the tides. This is a considerable increase on the previous value which is expected since the M_{sf} amplitudes in that model were smaller.

As an extension to this, I run the model with M_2 and S_2 tidal constituents only, and amplitudes ranging from 0.5 to 4. These results, shown in Fig. 6.8, demonstrate that as might be expected this increase in mean flow speed is also nonlinear and large tides have the potential to almost double the mean velocity of an ice-stream near its grounding line. This demonstrates that tidal forcing can not

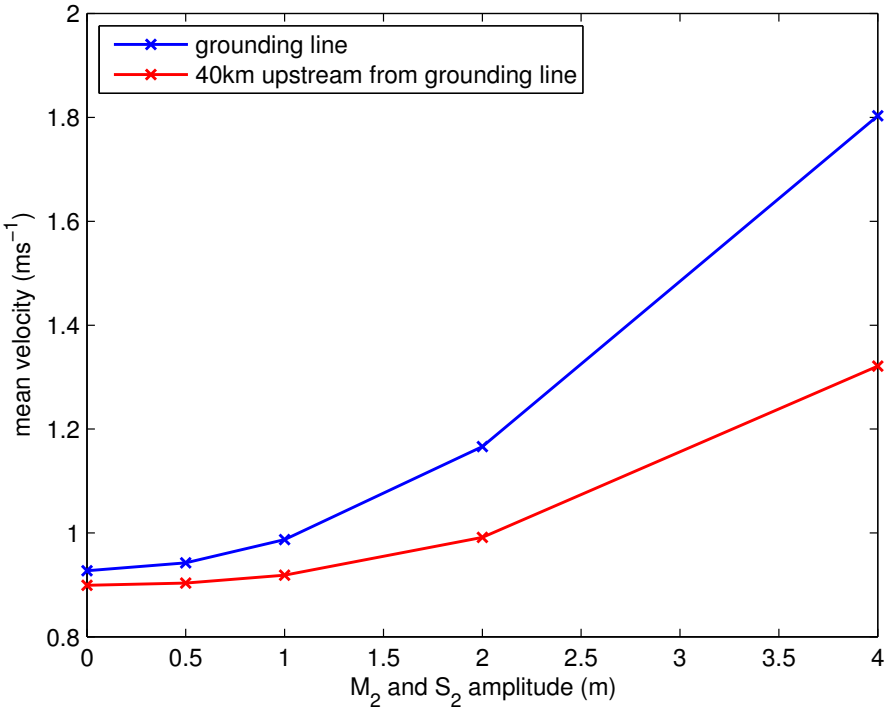

FIGURE 6.8: Change in temporal mean ice-stream surface velocity as a function of semi-diurnal tidal amplitude at the grounding line (blue line) and 40 km upstream from the grounding line (red line). All model parameters apart form the tidal forcing were the same as in Fig. 6.4, including c' whose inversion does not take into account any effect of tidal forcing on mean flow.

necessarily be ignored over longer time scales. Future changes in ice-shelf thickness and extent could lead to interesting feedbacks between tidal amplitudes and ice-stream velocities [Arbic et al., 2008, Rosier et al., 2014a].

6.5 Chapter Summary

1. The MSC.Marc model is used to try and quantitatively match observed M_{sf} modulation of the RIS with the ISS model presented in Chapter 3.

2. A range of free parameters is tested but no combination is found that can match the large observed M_{sf} amplitudes and decay length scales.

3. Adding tidally induced subglacial pressure variations can produce a qualitative match with observations, but only for a highly conductive drainage system at low effective pressure far upstream of the grounding line.

4. These results help constrain the type of drainage system that must exist beneath the RIS and demonstrate the importance of including a dynamic hydrological component to ice-stream models.

5. Coupled model results show the presence of tides result in a $\sim$12% increase in mean surface ice velocity.

Chapter 7

2D modelling of grounding line migration

Parts of this chapter are based on a manuscript entitled "Insights into ice-stream dynamics through modeling their response to tidal forcing", published for the Cryosphere on the 25$^{\text{th}}$ of September 2014 [Rosier et al., 2014b].

In this chapter I will present modeling results that consider grounding line migration. Two particular aspects of grounding line migration are investigated; the expected assymetry discussed in Section 2.5 and the generation of long period modulation in flow at M_{sf} period.

7.1 Elastic modeling of grounding line migration

The modeling approach used in Tsai and Gudmundsson [2015] was to treat grounding line migration as a crack propagation problem whereby the crack tip is the location of the grounding line. They assume that ice is purely elastic and grounding line migration is sufficiently asymmetric that considering only upstream migration captures the majority of overall migration.

I choose to approach this with a 2D FS elastic model of an ice-stream/ice-shelf that treats the location of the grounding line as a contact problem. The finite element mesh uses quadratic triangular elements (Fig. 3.3c) with grid refinement in the grounding zone. Grid refinement in the region of interest is 25m at the base and 125m at the surface compared to a typical resolution of ∼1 km elsewhere. The tide is implemented as in previous versions of the model as a uniform change in water pressure across the base of the ice shelf.

Solving the time varying position of the grounding line in this way has a clear advantage over the crack propogation approach because the geometry forms a crucial part of the problem which is not fully considered in the previous approach. The idealised geometry described by Tsai and Gudmundsson [2015], whereby surface and bed slope are both constant, results in a discontinuity or 'kink' in the ice geometry at the grounding line. When solving grounding line position as a contact problem the 'kink' in the basal function at the grounding line forms an obstacle to downstream migration. When this geometry is used in a contact model the ice inevitably rests on this 'kink' and requires large tidal amplitudes to migrate down beyond this point.

Since the geometry of the grounding line plays a central role in its tidal migration, using such a simple geometry is helpful but not necessarily indicative of realistic migration. I propose a similar geometry, where $\partial_x s$ is constant, but with a smoother transition in the grounding zone to avoid a discontinuous thickness gradient and arguably unrealistically severe 'kink' in the basal ice profile. A similar geometry but constant $\partial_x h$ is also used. This second test case is predicted by hydrostatic theory to exhibit perfectly symmetrical migration about the grounding line. The smooth transition takes the form of a quadratic basal function with a width of 8 km. Either side of this the slopes are constant as in previous studies. For the $\partial_x s$ geometry b is solved for downstream of the GL based on the a hydrostatic assumption, whereas s is solved for across the entire domain for the $\partial_x h$ geometry using the same approach. These two geometries are plotted in Fig. 7.1.

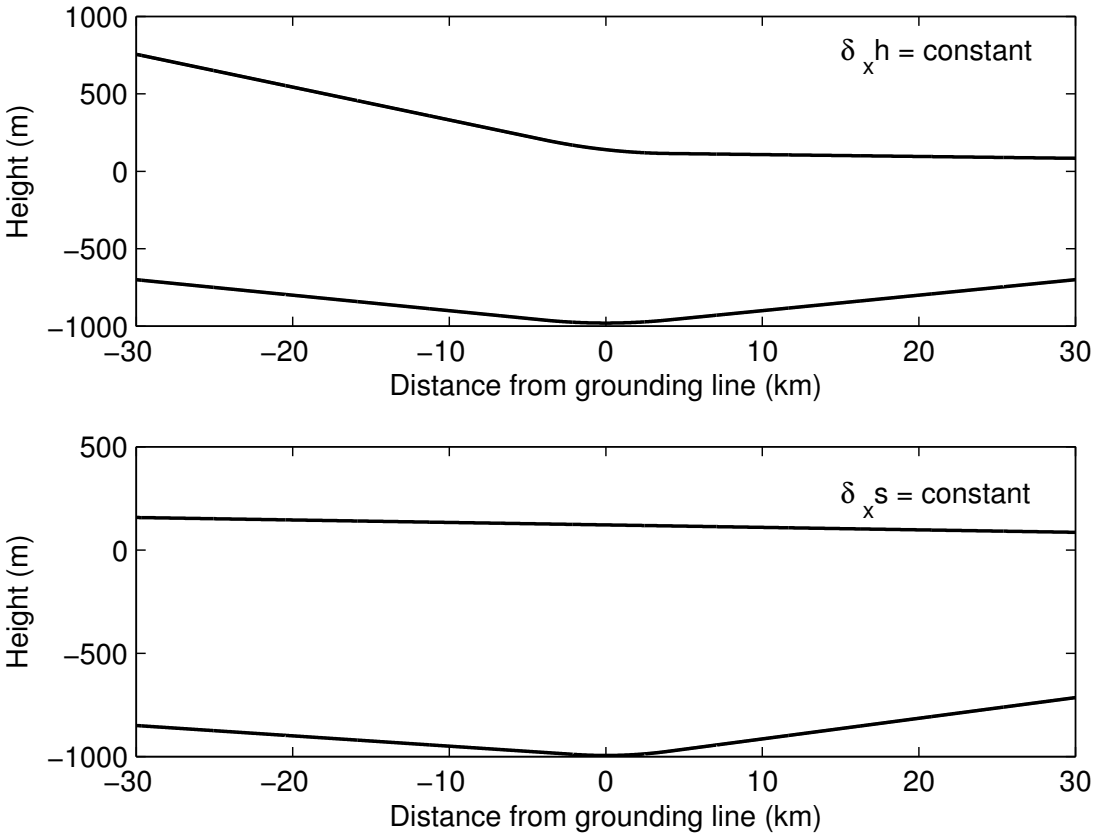

FIGURE 7.1: Model geometries for elastic FS GL migration studies, using a constant thickness gradient (upper panel) and constant surface slope (bottom panel). The grounding zone consists of a quadratic basal function with a width of 8 km.

A comparison can be made with the hydrostatic assumption by crudely discretizing Eq. (2.27). In order to avoid unrealistically large migration, small timesteps must be used to reduce each incremental ΔS and a further limit is put on the ΔL to avoid numerical issues in regions where $\partial_x b \to 0$. Results of tidal GL migration for the $\partial_x s$ geometry are shown in Fig. 7.2 and compared to the discretized hydrostatic case. This shows reasonably good agreement with the hydrostatic assumption and replicates the predicted asymmetry but both upstream and downstream migration distances are less in the elastic FS case. A geometry of this form produces a less acute asymmetry than the geometry which had a severe discontinuity in $\partial_x h$ at the grounding line. The upstream migration is ∼4200m compared to a downstream migration of ∼750m, giving an asymmetry ratio of ∼5.6, compared to a ratio of ∼9 predicted using the hydrostatic relation in Eq. (2.34).

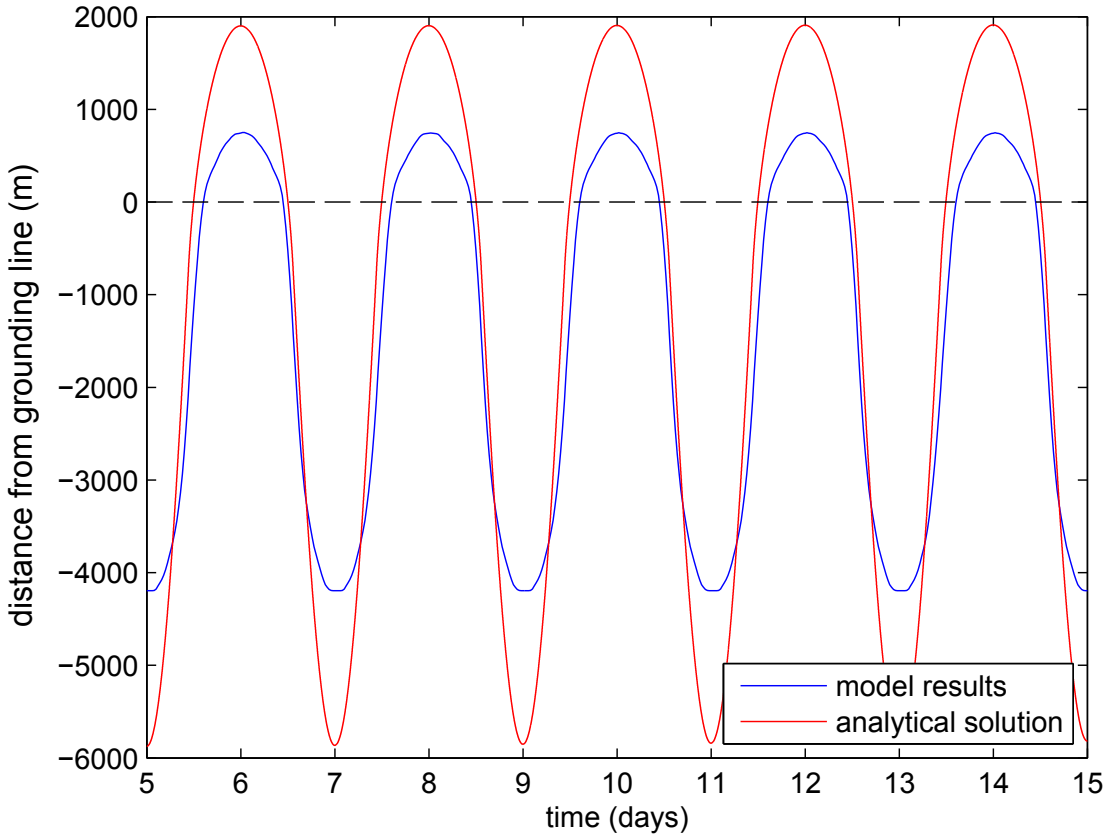

FIGURE 7.2: Comparison between the FS elastic GL migration (blue line, for the $\partial_x s$ geometry shown in the lower panel of Fig. 7.1) and the discretized hydrostatic GL migration (red line).

The same simulation was done for a $\partial_x h$ geometry (Fig. 7.3). Once again this agrees qualitatively with the hydrostatic approach, producing a periodic migration that is almost perfectly symmetric about the mean GL position. In both cases the preferred grounding line location was upstream of its starting point at $x = 0$. A large part of this is that, as a result of the smoothing of the basal profile, the ice is thinner at the GL. In addition it is expected that the FS GL position will lie upstream of a GL position calculated using the hydrostatic assumption [Tsai and Gudmundsson, 2015].

Results from these simulations confirm that tidally induced grounding line migration might be expected to be asymmetric about the mean GL position, in line with

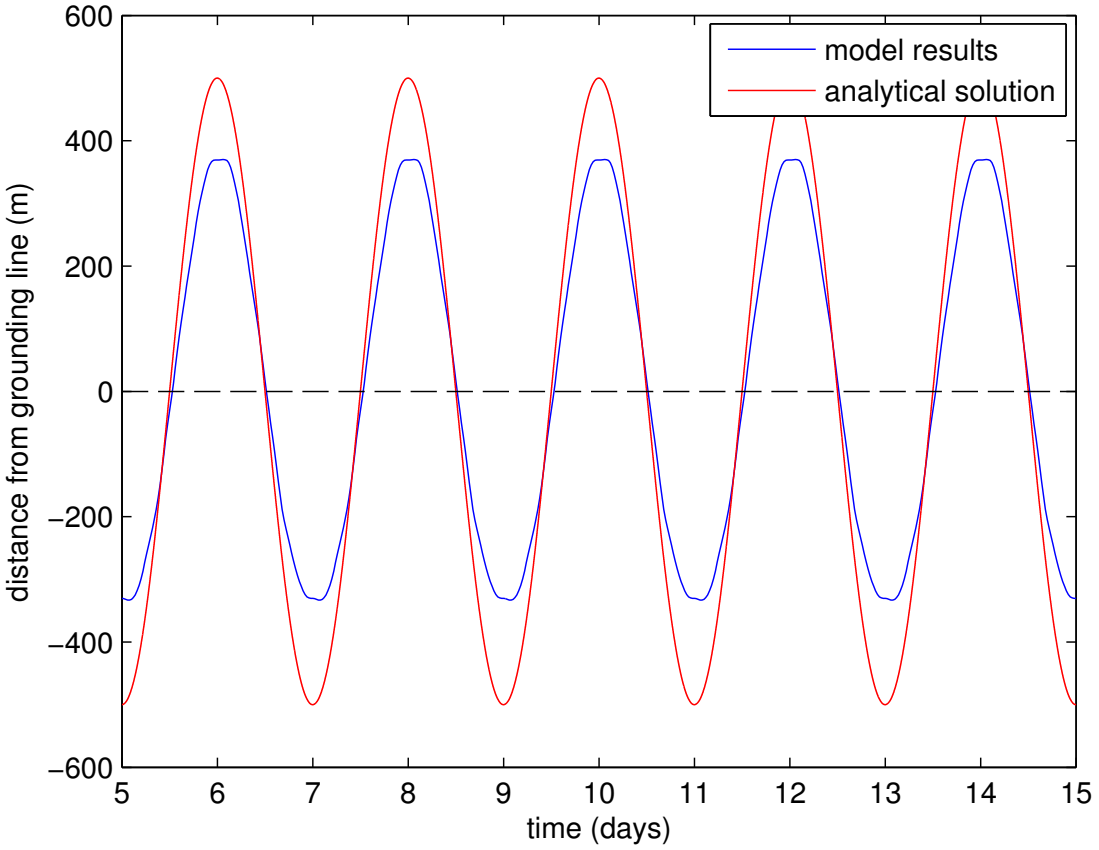

FIGURE 7.3: Comparison between the FS elastic GL migration (blue line, for the $\partial_x h$ geometry shown in the upper panel of Fig. 7.1) and the discretized hydrostatic GL migration (red line).

both the hydrostatic and crack propagation approaches outlined in Tsai and Gudmundsson [2015]. This asymmetry is an important feature which has previously been neglected for example when using grounding line migration to calculate bed slopes. Of particular interest to this work however, is the potential for an asymmetric GL migration to act as an additional non-linear response to tidal forcing. Specifically, if upstream migration is larger than downstream migration then one would expect a larger reduction in basal resistive stress during high tide than the equivalent increase at low tide. This process would act in phase with the hydrological effect outlined in Chapter 6.

7.2 Grounding line migration and the M_{sf} response

In order to investigate the effect of a migrating grounding line on an ice stream's long period flow modulation at M_{sf} period, a 2D geometry was used with refinement near the grounding line as depicted in Fig. 3.1c. The model setup was the same as in Chapter 5, with no hydrological coupling ($q = 0$) and no inversion. The aim of this section is purely to examine the effect of GL migration on the M_{sf} response of an ice-stream. Qualitative comparison with data is not attempted because the model is limited (due to computational considerations) to 2D and so is plane strain and does not include the crucial side drag that limits M_{sf} amplitude.

An initial control run used the same ice thickness and slopes as the 3D case, but with a slightly smaller domain extending 80 km upstream and 40 km downstream of the grounding line respectively. In this initial simulation the two contact bodies were not allowed to separate and thus the grounding line would not migrate, as in the 3D case. Since grounding line migration depends on the slope of the bed at the grounding line, with smaller slopes leading to larger migration distances (assuming surface slope is not changed), simulations with a migrating grounding line were done for various bed slopes ($\beta = 0.00375$, $\beta = 0.0075$ and $\beta = 0.01$) and compared with the non migrating case. To keep other properties as similar as possible the slope was only changed in a region near the grounding line and the majority of the bed had the same slope as other simulations.

Grounding line migration for the different slopes is asymmetrical as demonstrated in Fig. 7.4. Due to the difficult nature of the grounding line problem, at some points in the simulation isolated nodes or groups of nodes occasionally change in or out of contact some distance away from the expected grounding line position. As a result of this complication, grounding line position as plotted in Fig. 7.4 is defined as the point along the base of the ice where, traveling upstream, the ice makes contact with the bed for at least five consecutive nodes.

The comparison between tidal forcing and grounding line position in Fig 7.4 shows that at high tide the grounding line retreats considerably further than during low

tide, and the assymetry is slightly stronger for steeper slopes. Since the distance by which the grounding line migrates is so sensitive to geometry, which is represented here by a constant shallow slope but in reality is probably much more complex, these results should not be considered as an exact study of the tidally-modulated grounding line migration of an ice stream. In spite of this, the asymmetrical nature of the migration is expected, as shown in Sections 2.5 & 7.1, and so is a possible additional source of non-linearity that could help produce the large M_{sf} modulation observed on a number of ice streams.

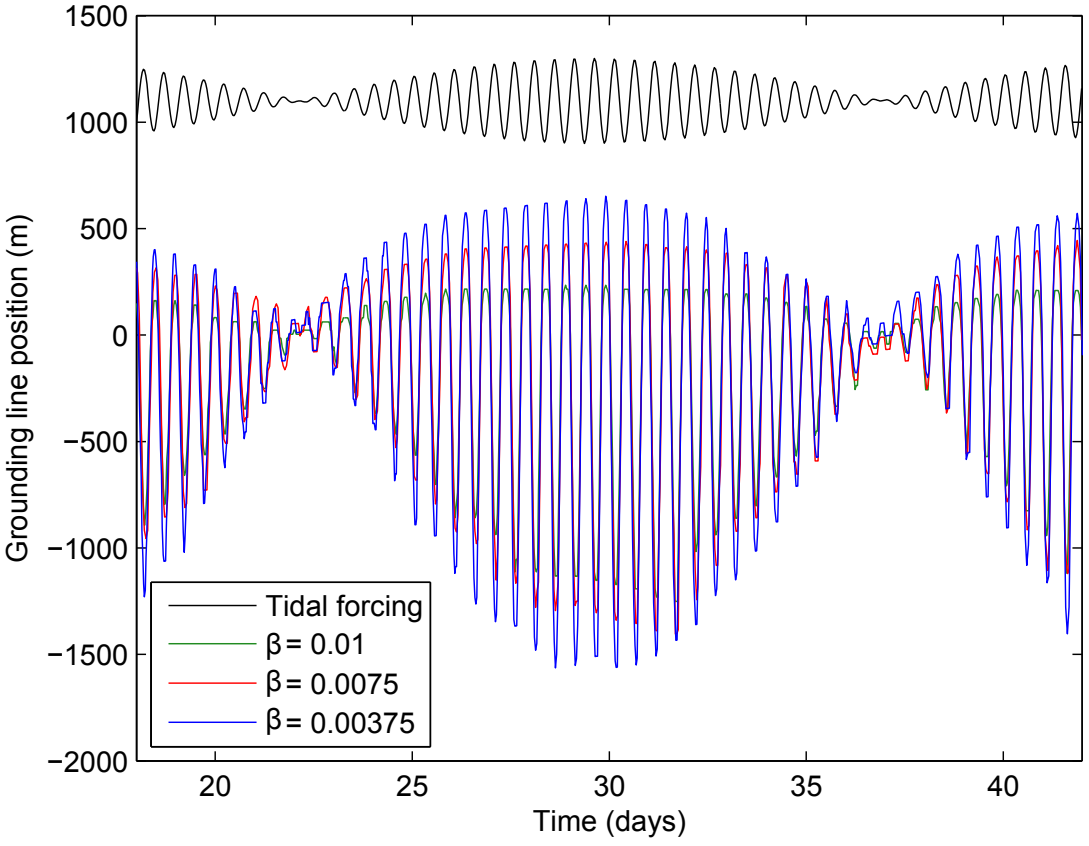

FIGURE 7.4: Comparison of change in grounding line position from the mean location, for various slopes (β) as a function of time. The tidal forcing is also shown (solid black line), scaled up and shifted vertically.

Results showing de-trended horizontal displacements for different migrating cases and the fixed grounding line run are shown in Fig. 7.5. The uppermost curve is the semi-diurnal forcing scaled down and shifted vertically. Beneath this are four curves showing de-trended horizontal surface displacement 10 km upstream of the

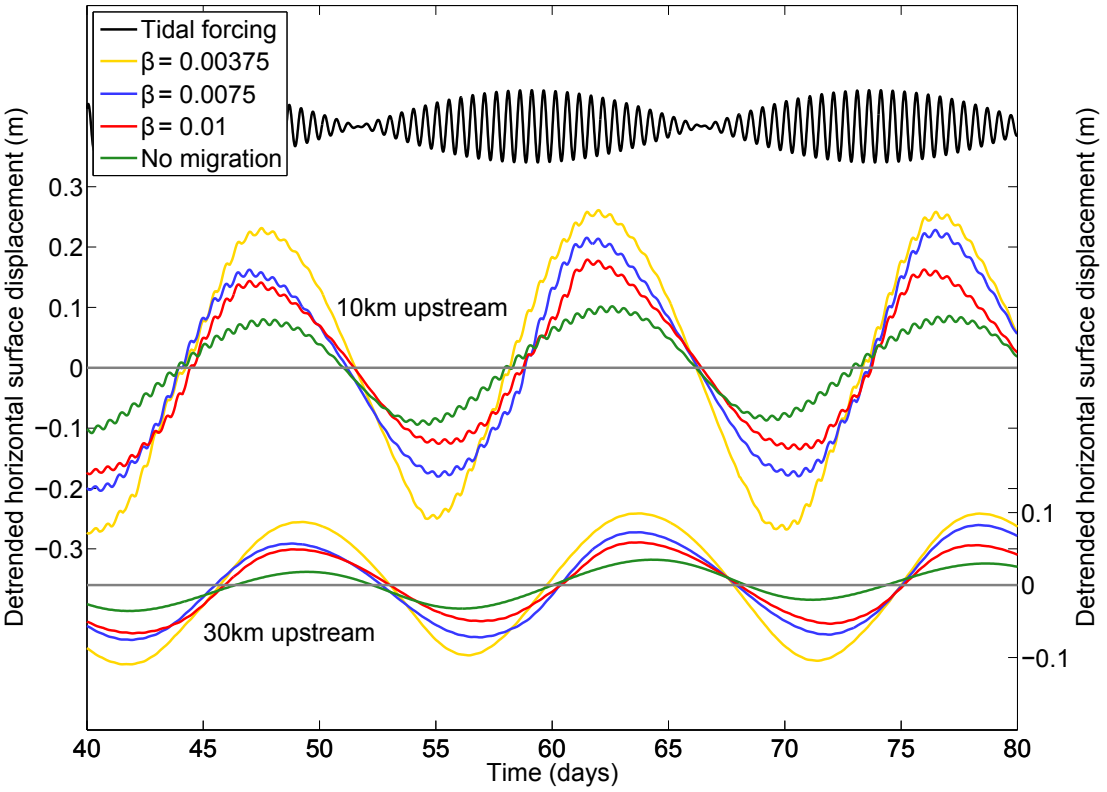

FIGURE 7.5: Comparison of de-trended in-line displacements for geometries with different slopes. The upper plot shows the tidal forcing (scaled down by a factor of 100 and shifted vertically for clarity). The middle plot shows in line displacements 10 km upstream of the grounding line with and without migration and the lower plot shows the same 30 km upstream.

grounding line for the no breaking case and slopes ranging from $\beta = 0.00375$ to 0.01. The final lowermost set of curves show the same but 30 km upstream. These results show that adding a migrating grounding line does not affect the main results demonstrated in previous chapters and qualitatively the long period modulation is the same as for a non-migrating case. Runs with smaller slopes and hence larger migration distances produce a stronger M_{sf} signal upstream of the grounding line, with the smallest slope producing displacements more than twice as large as in the fixed grounding line run. This is a result of the added non-linearity that arises due to the assymmetry of the grounding line migration.

7.3 Discussion

Purely elastic FS simulations find, in agreement with both the hydrostatic assumption and the fracture growth approach, that tidal GL migration can be strongly asymmetric depending on the ice-stream geometry in the grounding zone. Previous work has used simplified geometries with discontinuous basal profiles at the GL. I argue that in reality the transition from grounded to floating ice is smoother and results in different migration. The difference is largely due to the absence of a 'kink' which the ice will preferentially rest on before migrating downstream, but also because a smoother thickness profile will reduce the asymmetry unless the up and downstream migration both go beyond this transition region. As a result of these two effects, if the same change in thickness gradient is smoothed over a region of several kilometers then the resulting asymmetry will always be less than predicted with the hydrostatic approach.

If asymmetry is not as large as predicted by the hydrostatic approach then assuming that modeling upstream migration only will account for the majority of total migration distance is no longer particularly valid and so care must be taken to examine the geometry being considered before making this simplification.

An additional problem with the hydrostatic assumption (and the SSA which uses this assumption) is that the GL location does not match with the FS solution because stresses in this region play an important role. In order to produce a meaningful comparison, the FS GL location was used when calculating the GL migration using the hydrostatic approach. If the GL location as calculated using the hydrostatic assumption had been used instead, migration results would have differed even more between the two approaches since the point around which migration occured would have been in a region of different basal slope.

Viscoelastic simulations in 2D investigated the effect of GL migration on the generation of M_{sf} period modulation in ice-stream flow. I find that the ice-stream will still produce long period modulation that is qualitatively the same as when migration is not included in the model. Reducing the slope of the bed in the grounding

zone alters both the degree of asymmetry and the extent of migration and leads to larger M_{sf} amplitudes. Transmission of semi-diurnal forcing upstream from the grounding line appears to be unaffected.

Migrational asymmetry is less for shallower slopes, as would be expected since the discontinuous jump in thickness gradient at the GL is smaller. It might be expected therefore that M_{sf} amplitudes would be smaller than for steeper slopes, since this asymmetry helps generate the M_{sf} response, however it seems that the increased migration distance (and hence tidal stress penetration upstream) more than offsets this affect.

Unfortunately 3D simulations of grounding line migration were computationally too demanding to attempt, and provide a quantitative comparison with data as was done in Chapter 6. This means that no definitive statements can be made regarding the importance of GL migration in generating long period modulation in flow of ice-streams such as the RIS. Certainly there seems to be some potential to explain the larger observed M_{sf} amplitudes through tidally induced GL migration. Whether the RIS migrates the types of long distances upstream that have been modeled in this chapter is open to debate, as it could be resting on a pinning point that prevents almost any migration from taking place. The most likely scenario is that a combination of processes is occuring in tandem in order to produce these striking observations.

7.4 Chapter Summary

1. Purely elastic FS simulations are done using contact detection to solve for GL position and find tidal migration can be asymmetric in line with previous studies.

2. These elastic simulations agree reasonably well with a discretized form of the hydrostatic assumption.

3. A 2D FS viscoelastic simulation using the same geometry as in Chapter 5 also shows asymmetrical migration.

4. An ice-stream that includes GL migration still produces long period modulation in flow.

5. In cases where migration was greatest the resulting M_{sf} response is of greater amplitude than for the non migrating case.

Chapter 8

Ice-shelf tidal feedbacks

This chapter is based on a manuscript entitled "Modeling Antarctic tides in response to ice-shelf thinning and retreat", first published online in the Journal of Geophysical Research: Oceans on the 7$^{\text{th}}$ of January 2014 [Rosier et al., 2014a].

8.1 Introduction

Since the collapse of the Larsen B Ice Shelf in 2002 there has been a growing realization of the vulnerability of ice shelves in a warming environment [Glasser and Scambos, 2008]. Whilst current trends do not suggest that the Ross or Ronne-Filchner ice shelves are reducing in mass [Pritchard et al., 2012, Shepherd et al., 2010], recent work has shown potential mechanisms for reductions in thickness of the Ronne-Filchner [Hellmer and Rae, 2012], and other ice shelves are known to have collapsed in the past [Ó Cofaigh, 2011] indicating that the Larsen B collapse was not an isolated event.

If an ice shelf is perturbed in such a way as to reduce its extent and/or thickness or the position of the grounding line this would in turn affect the tide by changing local water column thickness or the position of the coastline. Ice shelf-tide feedbacks have been invoked to explain major catastrophic ice sheet collapse in the past, such as Heinrich events (eg. Arbic et al. [2004b]), but our understanding of

these feedback mechanisms is limited. Changes in tidal amplitudes following ice shelf collapse may thus have far reaching consequences for the dynamics of the ice sheets and global sea level [Fluckiger et al., 2006, Hemming, 2004].

The mechanism by which changes in ice shelf/stream geometry could alter local tides was explored by Griffiths and Peltier [2009] for the polar regions during the Last Glacial Maximum (LGM). While the extent of the changes in ice topography were greater than those we are considering here, their results highlight the potentially large shifts in tidal regime that may have occurred in the past and the potential sensitivity of Antarctic tides to changes in the position of the grounding line. The nonlinear interaction shown by Gudmundsson [2011] to exist between tides and ice streams suggests that a change in tidal amplitudes will modify mean ice stream flow. Due to tidal sensitivity to bathymetry and coastal topography it is to be expected that removal of floating ice will significantly alter tides across the Antarctic region. Here, we investigate the response of Antarctic tides to hypothetical reduction or removal of the Ronne-Filchner and Ross ice shelves. This work may be considered a sensitivity study of the Antarctic tidal regime and aims to reveal any areas of particular vulnerability warranting further investigation. The numerical simulations presented in this chapter demonstrate that hypothetical reductions in the extent of the Ross or Ronne-Filchner ice shelves could significantly alter tides in these regions, with implications for ice stream velocity and ice shelf stability which could lead to both positive and negative feedback situations depending on location.

8.2 Control

The control run results were compared to the CATS2008a model and shown to accurately reproduce the tidal amplitudes (Fig. 8.1). We use the convention of Arbic et al. [2004a] to evaluate the agreement between the two models by calculating a

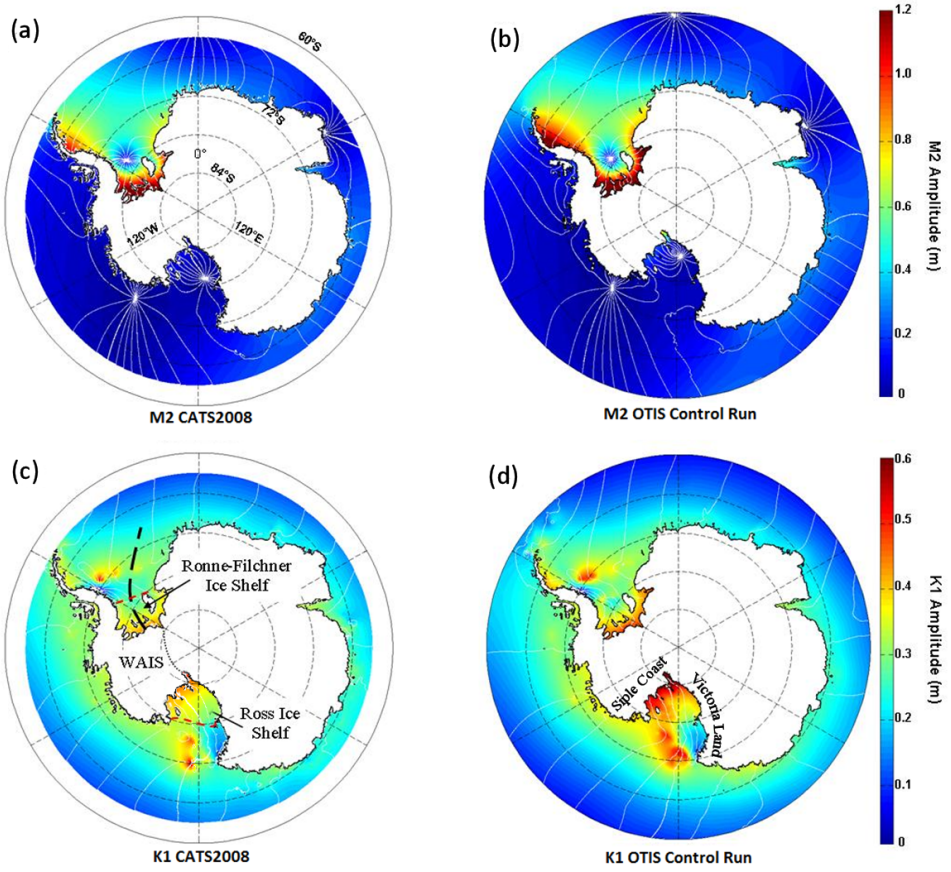

FIGURE 8.1: Tidal amplitudes (in meters) from the CATS model output (left) and from the present OTIS simulation (right). Panels a and b show M_2 amplitudes, whereas panels c and d show K_1 amplitudes. The white contours mark relative phases with 20° separation. Dashed red lines in panel c indicate the extent of the Ross and Ronne-Filchner Ice Shelves and the Antarctic Peninsula is the protruding region west of the Ronne Ice Shelf. The transect used for the response curve in Fig. 8.4 is marked as a dashed line in panel c.

root-mean square difference (RMS):

$$RMS = \sqrt{\frac{\left\langle \iint (S - S_{CATS})^2 \right\rangle dA}{\iint dA}} \tag{8.1}$$

where indicates the CATS2008a model output. From the CATS2008a model we also compute a signal, $\hat{S}$:

$$\hat{S} = \sqrt{\frac{\left\langle \iint (S_{CATS})^2 \right\rangle dA}{\iint dA}} \tag{8.2}$$

and finally the percentage of sea surface height variance (SSHV) captured by the model as:

$$SSHV = 100 \times [1 - (RMS/\hat{S})^2]. \tag{8.3}$$

There is good agreement between the two models, with a root-mean-square difference of 7.8 cm and 4.4 cm capturing 94% and 97% of the variance for M2 and K1 respectively over the entire domain up to 62°S. Since a large part of the domain is in the deep ocean with small amplitude tides, values were also calculated for only shallow regions (h<1000m) which gave RMS values of 10.3 cm and 7.2cm for M2 and K1 respectively. While these values are considerably larger the main trend in the results can still be considered robust as discussed below. The M_2 constituent has a reasonable amplitude in and around the Weddell Sea, whereas K_1 dominates the Ross Sea. Both the M_2 and K_1 amplitudes are generally overestimated in the control run (Fig. 8.1) compared to the CATS2008a results. Of course, an assimilated model such as CATS2008a obtains better agreement with observations, but any perturbation experiments with an assimilated model are dubious at best. Because our model reproduces all the major tidal features in the region with reasonable accuracy we have confidence in our results.

8.3 Sensitivity simulations

The M_2 tide in the region is dominated by a large amphidromic point centered in the Weddell Sea which results in significantly lower tidal amplitudes beneath the centre of the adjacent Ronne-Filchner Ice Shelf than would otherwise be the case. All perturbation runs show considerable amplification of the M_2 tide under the main body of the Ronne-Filchner ice shelf, with a stronger response when more of the ice shelves are removed (Fig. 8.2). Halving the extent of the ice shelves (Fig. 8.2a) is found to produce less amplification than halving the thickness (Fig. 8.2b) and sets up an additional bimodal response between the Filchner and Ronne ice shelves. Further amplification arises in the HTE run (Fig. 8.2c) and the no ice run (Fig. 8.2d) shows reduction in M_2 amplitude along the eastern

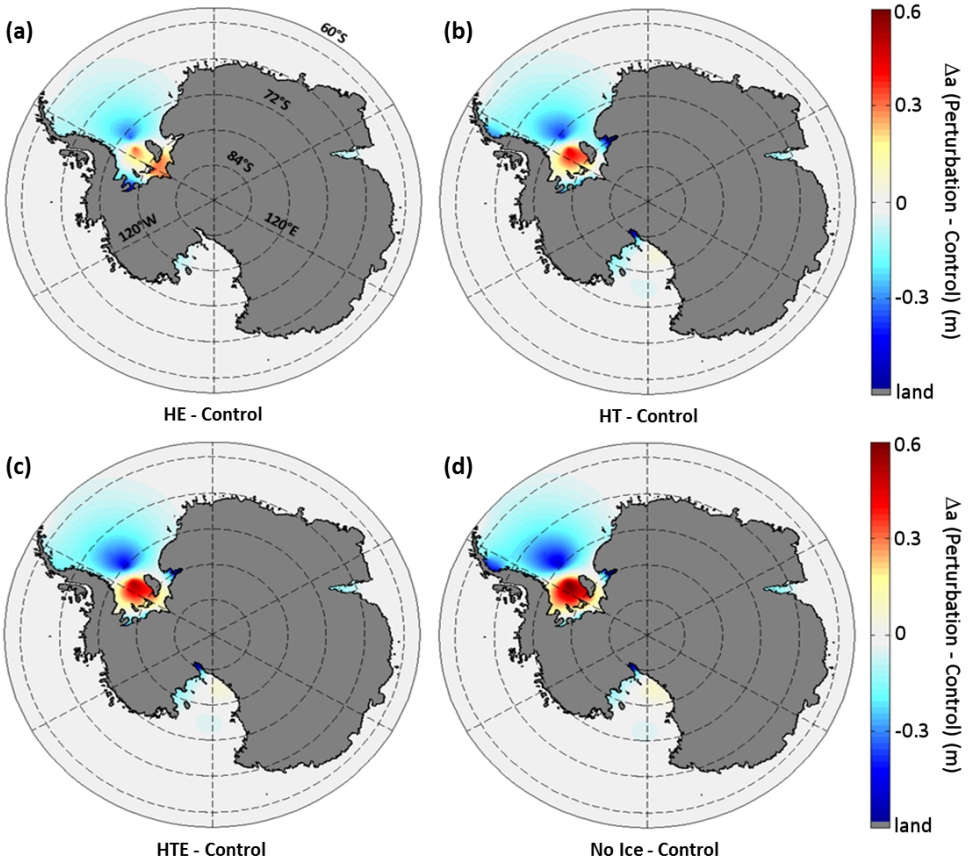

FIGURE 8.2: Change in M_2 tidal amplitude (compared to the control run) – where positive values indicate an increase in the perturbation run– resulting from removal of ice shelves for cases HT (panel a), HE (b), HTE (c) and no ice (panel d). Note that M_2 amplitude changes under the Ross Ice Shelf are negligible but the M_2 tide in this region is very small in the control.

.

side of the Antarctic Peninsula. Because the K_1 tidal signal is not dominated by one amphidromic system but rather contains several features, the removal of ice shelves results in a less clear effect than for the M_2 constituent (Fig. 8.3). The K_1 amplitude under the western Ross Ice Shelf is decreased by approximately 10 cm (17%) in all perturbation scenarios, and removing more ice increases the extent of the affected area. An additional response to the reduction of ice shelves is an increase in amplitude along the Victoria Land coastline, close to the ice front. In contrast, the tides in the Ronne-Filchner embayment show some decrease in K_1 amplitude along the grounding line once most of the ice has been removed. Overall the changes in the K_1 constituent are of a much lower magnitude than the M_2 tide and whereas the largest effects on M_2 tend to be found centered under

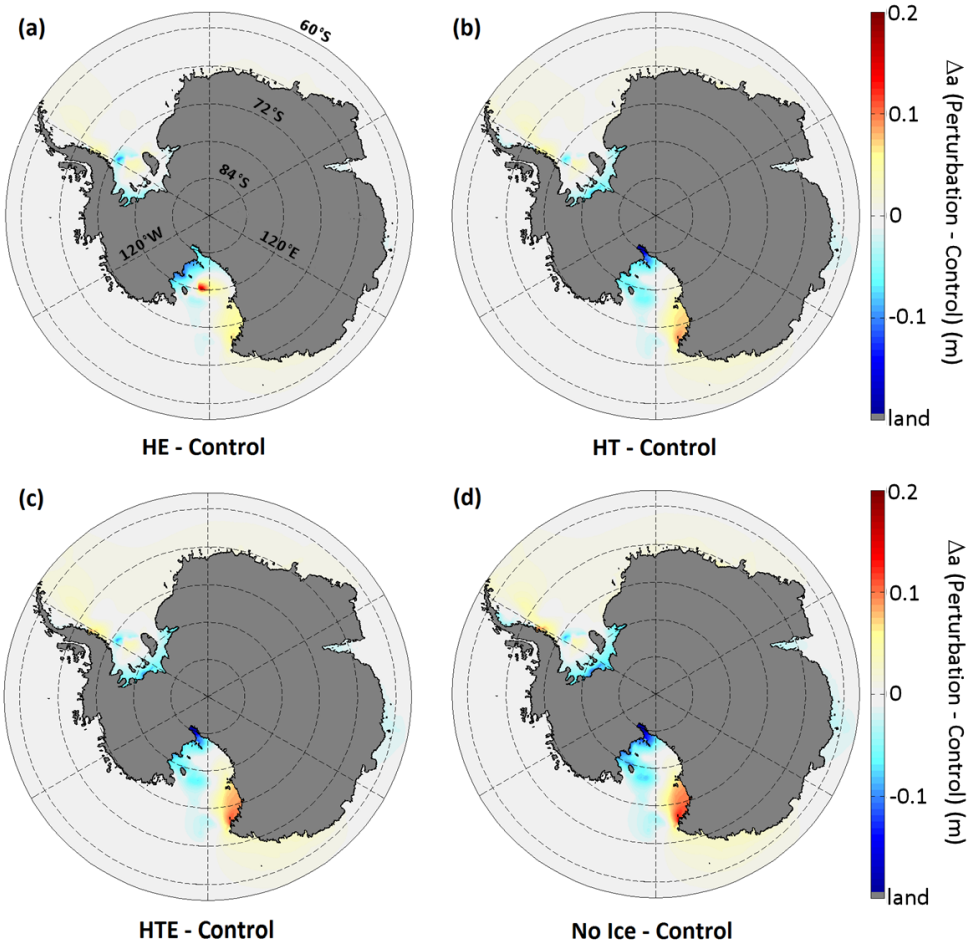

FIGURE 8.3: Change in K_1 tidal amplitude (compared to the control run where positive values indicate an increase in the perturbation run) resulting from removal of ice shelves for cases HT (panel a), HE (b), HTE (c) and no ice (panel d).

.

the Ronne Ice Shelf, K_1 effects tend to be most prominent closer to the coast.

To further highlight the response, a transect of the M2 tidal amplitude for the different simulations was plotted through the Ronne Ice Shelf (Fig. 8.4a) along with the difference in perturbation amplitudes to the control (Fig. 8.4b). Maximum amplification in the Weddell Sea is found with complete removal of the ice shelves at 77.5°S, with the M_2 amplitude more than doubling in this region. The M_2 amphidromic point moves away from the ice front in all the perturbation runs, not only due to the retreat of ice but also as a response to the changing water column thickness. Overall, the transect reveals M_2 amplification under the bulk of the Ronne Ice Shelf with amplitude under the centre more than doubling.

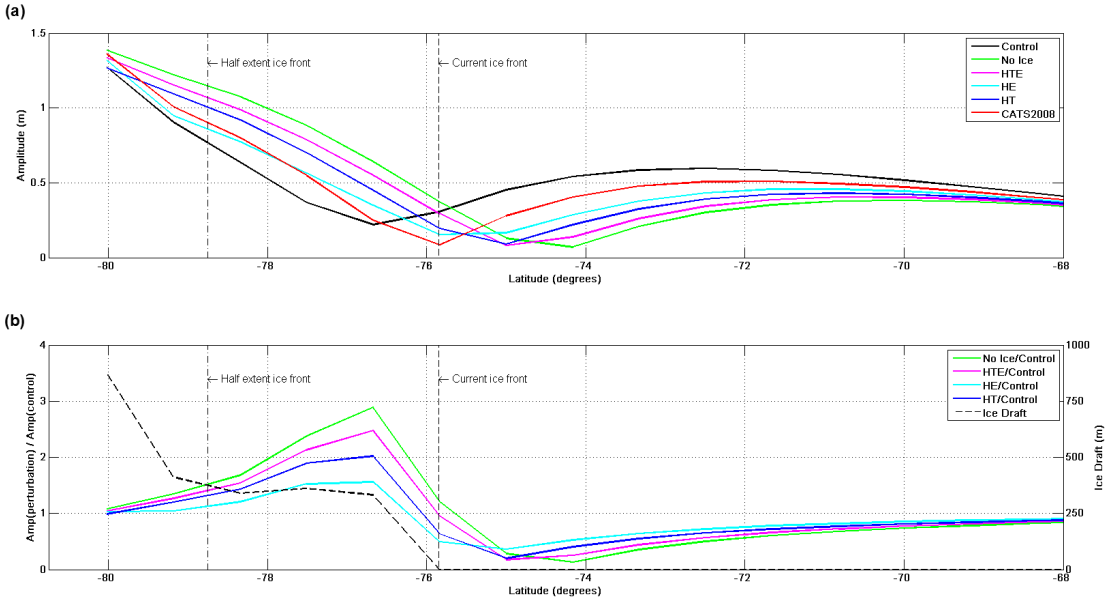

FIGURE 8.4: Response curve of M_2 amplitudes across transects (marked in Fig. 8.1c) of the Ronne Ice Shelf to changes in ice cover. The submerged portion of ice thickness along the same transect is also shown (panel b) along with the locations of the ice fronts for the present and HTE runs (dashed lines).

.

Tidal dissipation for the HT, HTE and No Ice sensitivity simulations are compared to dissipation from Eqs. (4.7–4.9) from the control run for the M_2 (Fig. 8.5) and K_1 (Fig. 8.6) tidal constituents. The dissipation estimates were split into total (i.e., for the whole domain), deep (i.e., the energy losses in water where h >1000 m), and shallow (i.e., in water where h<1000m). Note that shallow and deep regions were defined for each run separately to accommodate for changes in water depths. Changes in dissipation as a percent compared to the control are presented in Table 8.1.

TABLE 8.1: Changes in M_2 and K_1 Dissipation rates (GW) compared to the control run for shallow water (h < 1000 m), deep ocean (h > 1000 m), and total (percent change in brackets).

Run Name	Shallow	Deep	Total
	M_2 Dissipation Change (GW)		
HT	4.8 (14.7)	-1.4 (-7.3)	3.5 (6.8)
HTE	9.4 (28.6)	0.7 (4.3)	10.2 (19.8)
No Ice	14.1 (43.0)	7.5 (40.8)	21.7 (42.2)
	K_1 Dissipation Change (GW)		
HT	-6.9 (-19.2)	-2.3 (-8.7)	-9.2 (-14.8)
HTE	-8.4 (-23.4)	-2.5 (-9.5)	-10.9 (-17.5)
No Ice	-9.0 (-25.4)	-2.5 (-9.5)	-11.5 (-18.6)

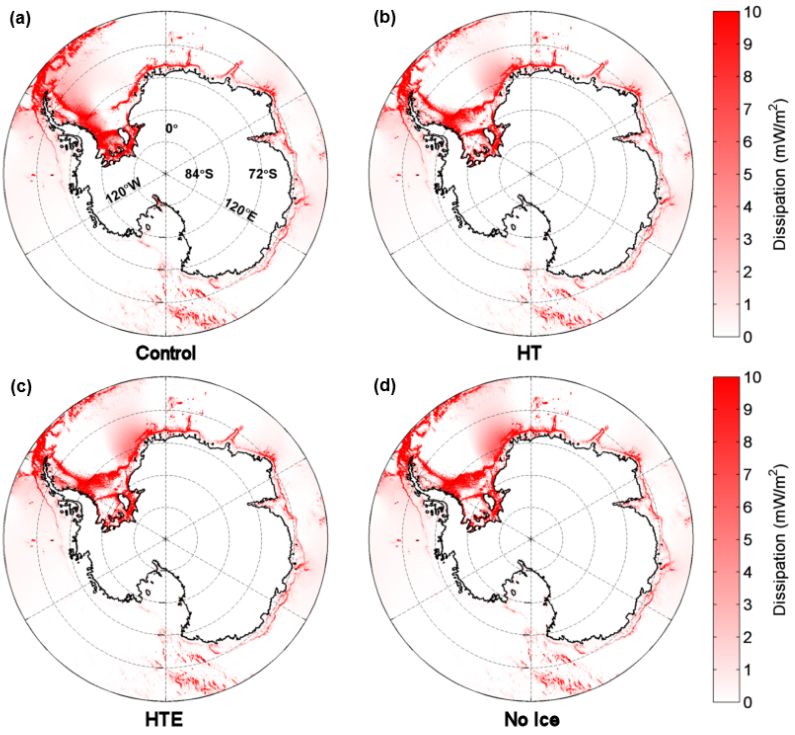

FIGURE 8.5: M_2 tidal dissipation for the control run (panel a) and the HT (b), HTE (c) and No Ice (d) perturbation runs.

.

The M_2 tidal dissipation generally increases as the ice shelf is removed (Fig. 8.5 and Table 8.1), with changes in total dissipation compared to the control of 42.2% for the No Ice run. Most of the change in dissipation occurs on the continental shelf, while the deep ocean dissipation initially decreased slightly for the HT run and increased for the HTE and No Ice runs. In contrast to this, K_1 dissipation decreases by 18.6% for the No Ice sensitivity run. Once again the change in shelf dissipation accounts for the majority of these changes and deep sea dissipation is only slightly reduced for all the runs.

8.4 PISM-PIK simulations

As an extension to the sensitivity scenarios outlined above, tidal runs were performed for an Antarctic bathymetry derived from projections of ice extent by the Potsdam Parallel Ice Sheet Model (PISM-PIK) [Martin et al., 2011, Winkelmann

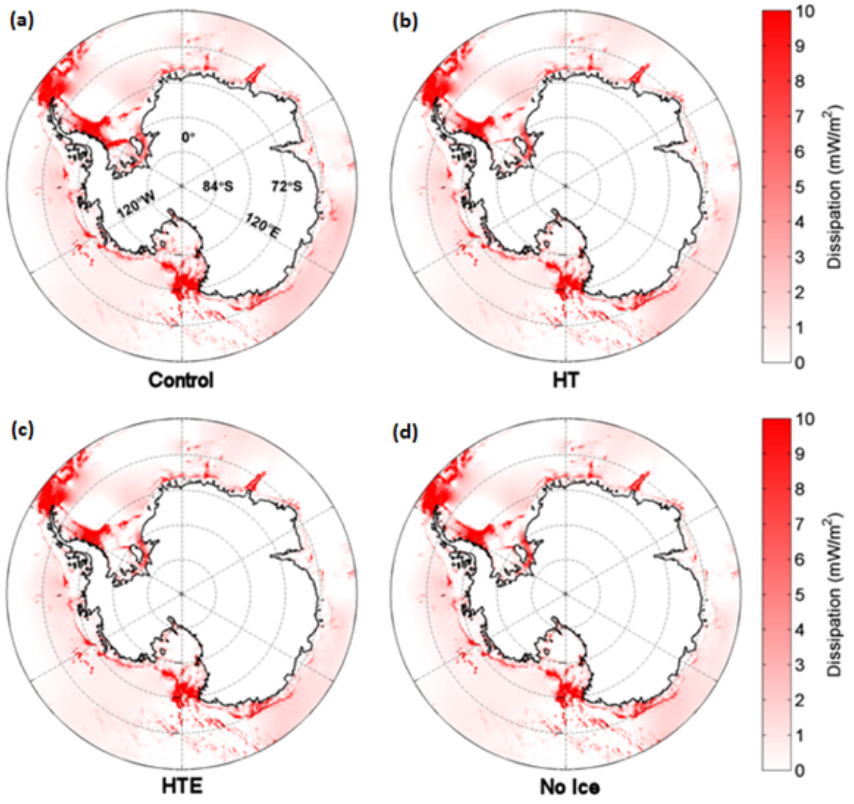

FIGURE 8.6: K_1 tidal dissipation for the control run (panel a) and the HT (b), HTE (c) and No Ice (d) perturbation runs.

.

et al., 2011, 2012] up to the year 2500. The PISM-PIK results were produced by forcing from the Extended Concentration Pathways (ECP) 8.5 climate scenario, in which greenhouse gas emissions continue to rise until the year 2250 at which point they begin to decline [Meinshausen et al., 2011]. Results from the PISM-PIK run were provided as anomalies in ice thickness and a shelf mask, in 100 year time slices, from which the new tidal bathymetries were produced. These were then introduced into OTIS using the control settings in terms of friction.

The changes in ice sheet extent and thickness from the ECP run for PISM-PIK can be broadly divided into three tidally relevant parts: minor grounding line retreat along much of the Antarctic coastline, significant grounding line retreat along the Siple Ice Coast and a partial collapse of the Ross Ice Shelf to a new, much reduced extent that appears to stabilize at around year 2350. Overall the changes are focused around the Ross Sea area and this might explain why the

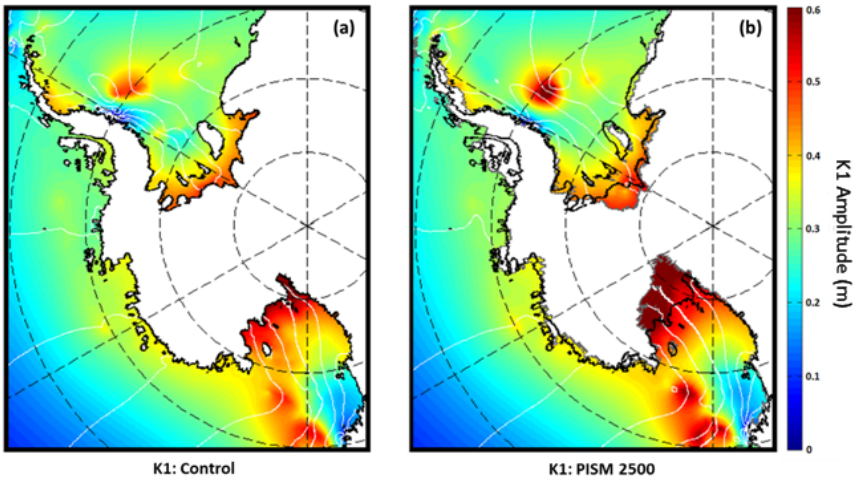

FIGURE 8.7: Comparison of K_1 amplitude resulting from ice anomalies output by the ECP-8.5 scenario PISM-PIK run [panel b; data from Winkelmann et al., 2012] with the control run (panel a). The present day grounding line position is indicated by the thick black line and the new PISM-PIK grounding line in year 2500 is marked in grey in panel b. The white contours mark relative phases with 20° separation

.

modeled changes in the M_2 tidal constituent are very minor since the present day M_2 tide is very weak in this region. The changes in the Ross Sea, from year 2500 in the PISM-PIK model, result in considerable changes in the K_1 tidal constituent which are compared to the K_1 control run in Fig. 8.7. While the general pattern of the tide remains the same, K_1 amplitudes across the entire region are generally increased by over 100%, leading to almost a 1m K_1 tidal amplitude along the Siple Ice Coast. K_1 amplitudes are also increased somewhat in the Weddell Sea, suggesting that the K_1 tidal constituent in this region is more sensitive to the position of the grounding line than the M_2 tide for this grounding line retreat scenario.

8.5 Discussion

In this chapter I have undertaken studies of the sensitivity of M_2 and K_1 tides to the reduction in extent and thickness of Antarctic ice shelves. This is motivated by the known interactions between tides and ice shelves, and the possibility that these

TABLE 8.2: Horizontally Averaged Amplitudes (A) (m) and Dissipation Rates (D) (μW m^{-2}) From the Weddell and Ross Seas From the Resonance Analysis

	Period (h)									
	6.21		12		12.42		23.9		25.82	
Run	A	D	A	D	A	D	A	D	A	D
					Weddel Sea region					
Control	0.0191	0.0171	0.6907	6.5212	0.9565	13.2868	0.3566	0.7373	0.3511	0.6524
HT	0.8871	623.6119	0.5558	10.8296	0.8871	28.2164	0.3441	0.9127	0.3398	0.7812
HTE	0.9338	673.8912	0.5705	12.503	0.9338	34.0886	0.3392	0.9322	0.3337	0.7918
No Ice	0.968	917.6976	0.5755	17.3798	0.968	48.9239	0.3355	1.1181	0.3319	0.9708
					Ross Sea region					
Control	0.0029	0.0004	0.1355	1.437	0.0755	0.2402	0.392	1.8454	0.3175	0.9036
HT	0.0528	1.2323	0.0513	0.139	0.0527	0.1257	0.3768	1.7882	0.3078	0.9695
HTE	0.0566	1.405	0.0537	0.1632	0.0565	0.1572	0.3786	1.7792	0.3088	0.9596
No Ice	0.0666	3.4386	0.0595	0.1916	0.0665	0.2116	0.3702	1.7999	0.3032	1.0011

interactions may change in a warming world. Tidal response in amplitudes and dissipation rates are shown in Table 8.2 to verify the resonance characteristics of the study areas for M_4, S_2, M_2 , K_1 and O_1 tides. The results shown are horizontal averages of the amplitudes and dissipation from each area and chosen somewhat arbitrarily but such that the full response is covered. To further elucidate the

mechanisms behind the results, we also look at the amplitudes and dissipation rates in a simple damped harmonic oscillator (see also Egbert et al. 2004, Green 2010 and Arbic and Garret 2009). In its simplest form, we thus solve

$$\partial_{tt}u + \gamma\partial_t u + u = sin(\omega t), \tag{8.4}$$

where ω is the forcing frequency, γ is the damping coefficient, and subscripts denote derivation. It is easily shown that the amplitude of the oscillation is

$$A = \frac{1}{\sqrt{(1-\omega^2)^2 + (\gamma\omega)^2}} \tag{8.5}$$

and the dissipation comes out as

$$D = 0.5\Re|i\omega/(1 + i\gamma\omega - \omega^2)| \tag{8.6}$$

(see Fig. 8.8 for the results). Note that the solution in Fig. 8.8 has arbitrary units, and rather than obtain a quantitative result for each of the ice shelves, the oscillator is introduced as a concept to provide qualitative arguments for why we see the responses we do in the simulations. Also note that our sensitivity runs effectively have a reduced damping because the ice is removed, leading to reduced frictional effects.

In the Weddell Sea the M_2 amphidromic point moves further off shelf as the ice shelf bathymetry changes, and there is consequently an increase in the tidal amplitude near the coast (Fig. 8.2). However, the overall tidal amplitudes decrease in the Weddell Sea in the perturbation runs (Table 8.2), but the dissipation increases. This is because of an enhanced dissipation further off shelf in the Weddell Sea (near the shelf break; see Fig. 8.1) which shifts the amphidromic point in the area and provides an enhanced amplitude closer to the coastline. In (non-resonant) tidal systems large enough to be influenced by rotation, amphidromic points will shift towards an area of increased dissipation (e.g. Pelling et al. 2013, Taylor 1921). This is the picture we see here for M_2 , with an enhanced tidal dissipation in the

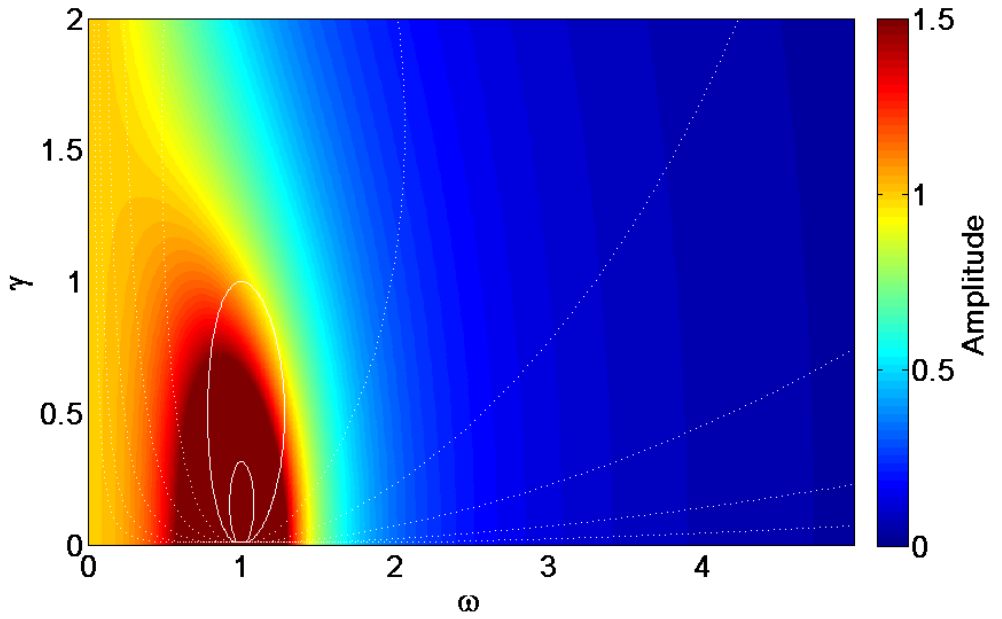

FIGURE 8.8: Amplitude (in color) and $\log_{10}$ dissipation (white lines) for a damped harmonic oscillator for different values of damping (γ) and forcing frequency (ω). Note that the units are arbitrary.

.

outer part of the Weddell Sea due to the removal of the ice-shelves, and a shift outwards of the amphidromic point (Figs. 8.1 and 8.2).

Table 8.2 also shows that the Weddell Sea becomes resonant for M_4 in the sensitivity runs. The decrease in semi-diurnal amplitudes in the perturbation runs is associated with an increased dissipation rate, however, suggesting that the Weddell Sea experiences a shift in its natural frequency when the damping is reduced (see Fig. 8.8; with only a reduced damping it is not possible in this set-up to have both increased dissipation and a decreased amplitude). The real surprise lies in the quarter-diurnal band, which has been neglected previously in the area because the (control) amplitudes are very small. In the sensitivity simulations, however, the M_4 tide becomes very energetic and is almost as large as the M_2 tide in the Weddell Sea. There is consequently a significantly enhanced dissipation of M_4 energy, which – since the damping is reduced in the sensitivity runs – must signify that the Weddell Sea has become resonant for the quarter diurnal period.

The Ross Sea results (Table 8.2) show only minor changes for the longer period tides, again with a general decrease as part of the damping (i.e. the ice shelf)

is reduced or removed. The exception is again in M_4, which is characterized by a very large increase in dissipation. The reason for this is most likely that the Ross Sea, like the Weddell Sea, becomes resonant for M_4 when the ice/damping is removed. The changes in dissipation between the control and sensitivity runs are also of interest, particularly since these could affect basal melt rates beneath the ice shelves. The increase in M_2 dissipation of up to 40% is due to the tide becoming more energetic as more ice shelf is removed. The dissipation is generally reduced beneath the Ronne-Filchner Ice Shelf but increases at the shelf edge of the Weddell Sea and around the tip of the Antarctic Peninsula. Changes in spatial distribution of dissipation do not necessarily match those in amplitude because the dissipation depends on the cube of velocity which in turn is controlled by water depth and the surface slope.

The K_1 dissipation responds differently to the ice extent changes than does M_2 : the K_1 tide decreases compared to the control run in our sensitivity runs. Here we see the areas of most reduction at the shelf break of the Ross and Weddell Seas, particularly along the western boundary where the tidal wave enters the embayment. Unlike the changes in M_2 dissipation, there is no notable change beneath either ice shelf and in fact almost all change is negative, typically around -20% over the entire domain, with no large regions of increased dissipation.

Some caution should be used when interpreting these results since the present day model overestimates tidal amplitudes to some extent. We are not proposing a realistic future scenario but rather a sensitivity study; however, since the amplitudes in the perturbation runs are also most likely overestimated the difference between the two can still be considered a valid signal. Better parameterization of the ocean/ice shelf interaction in future studies, particularly in the hinging zone, since this is the main missing process in the region, along with higher resolution bathymetry, may go some way to improving this. It is also important to note that changes in tides resulting from altering ice shelf geometry are likely to be accompanied by changes in the exchange of water masses from the ice shelf cavity to the open ocean; this is not modeled here.

Major thinning and/or retreat of ice from the Ronne-Filchner Ice Shelf is very likely to produce feedbacks arising from increased M2 tidal amplitudes. Since the pattern of changes are not all in the same direction these feedbacks may be positive or negative, but generally amplitudes are found to increase. Because of the nature of the relationships between tidal amplitudes and ice shelves and ice streams, these feedbacks are considered dominantly positive. The Ross Ice Shelf shows a similar response to the K1 tide but only when grounding line retreat is included as in the tidal runs arising from the PISM-PIK results. The asymmetry in surface velocities resulting from the non-linear response to the inclusion of tides in the ice stream model presented by Gudmundsson [2011] leads to increases in mean velocity of about 5%. More recent modeling work suggests this effect could be as large as 12% in the vicinity of the grounding line [Rosier et al., 2015]. Extrapolating these results to estimate the effect of the increase in tides on ice stream velocities is not trivial due to the non-linearity inherent in this relationship. While the impacts of the changes in M_2 and K_1 amplitudes on ice shelf or ice sheet dynamics are not modeled directly here, a doubling of tidal amplitude under the Ronne-Filchner Ice Shelf cannot be ignored as a feedback on both ice shelf stability and ice stream velocity. The ice streams draining the WAIS sector of the Ronne-Filchner Ice Shelf would appear to be particularly vulnerable, including the Evans, Carlson, Rutford, Institute, Foundation and Support-Force systems [Rignot and Thomas, 2002]. In addition, the changes in dissipation calculated for our sensitivity simulations suggest that this is another important factor to consider when evaluating the effects on ice dynamics through changes in basal melting. There is therefore a requirement to investigate both the impact of tidal motion on calving and ice stream processes and rates, and to couple ice sheet models with tidal models to further constrain this hitherto neglected Earth system feedback that has potentially significant implications for our understanding of past and possible future major ice sheet collapse.

8.6 Chapter Summary

1. The OTIS tidal model is used to investigate the response of Antarctic tides to the thinning and retreat of the FRIS and Ross ice-shelf.

2. Results of a control simulation with no changes to ice-shelf geometry compare favorably with the CATS2008 model.

3. Reduction in the extent and thickness of the FRIS leads to a shift in the Weddel Sea amphidromic point and an increase in M_2 amplitude beneath the FRIS.

4. In the Ross Sea the effects are largely seen in the K_1 tide, where amplitude is decreased along the Siple coast and increased along the Victoria land coastline.

5. There is a large increase in M_2 shelf dissipation and a slight decrease in the K_1 dissipation as ice-shelves are removed.

6. The M_4 tidal constituent appears to become resonant in the Weddel Sea as the ice-shelf thickness is reduced, leading to much larger amplitudes and dissipation than in the control.

Chapter 9

Summary and Outlook

9.1 Summary

In this thesis I present model results from both ISS and tidal models to investigate the interactions between tides and ice-streams.

Much of the work presented here focuses on the fascinating M_{sf} modulation of ice-stream flow, observed on the RIS, that is both large in amplitude and travels far upstream of the GL. Previous flow line studies suggested that this effect might arise as a result of the stress exponent m in the sliding law being greater than one, resulting in a source of nonlinearity that would explain this response. I extended this previous study to include lateral drag from sidewalls and find that the mechanism is still valid, but only attempt to match RIS data qualitatively.

As a next step I seek to match the RIS observation quantitatively, conducting a parameter study to determine if some combination of free parameters might be the key to producing the large amplitudes needed to agree with GPS measurements. The outcome of this parameter study is that the amplitude of the M_{sf} response cannot be produced through stress transmission alone, and in fact it is clear that an important process is missing since the model produces an M_{sf} amplitude that is an order of magnitude too small.

Addition of coupling between the ISS model and a subglacial hydrological model turns out to be the key ingredient needed. Tidally induced pressure variations in the subglacial drainage system alter effective pressure and hence the ice-stream flow. In order for this effect to be large enough to explain observations a number of criteria must be met.

1. The drainage system must be highly conductive to allow pressure perturbations to be transmitted far upstream from the GL.
2. The region upstream of the GL must be near flotation, such that the effective pressure is low enough that relatively small changes in sea level of a few meters produce relatively large changes in ice-stream velocity.
3. A nonlinear stress exponent is still required in order to transmit this effect far enough upstream.

These results, although obtained through modeling of the RIS only, are arguably relevant to many other ice streams in this area draining large portions of the WAIS. The ability to constrain the basal sliding law in this way is unique and has implications for the way ice streams respond to an external forcing. An ice stream with a strongly nonlinear sliding law would be expected to respond more rapidly to any climatic changes occuring on the Antarctic continent. Antarctic ice-stream modeling tends to ignore the effects of subglacial hydrology as this is bundled into a slipperiness term that is inverted for using present day flow conditions. The problem with this is that when the ice sheet is perturbed considerably under a future or past climate scenario the hydrology will evolve but this cannot be accounted for in a slipperiness term that varies spatially but does not evolve with time. If other ice streams are as sensitive to changes in the drainage system as the RIS this is a factor that must be considered when making long term predictions of the evolution of the AIS.

An important consequence of an ice-streams nonlinear response to tidal forcing is that mean flow velocity is increased due to the presence of the tides. Previous

work suggested that this effect accounted for a ∼5% increase in mean flow for tidal amplitudes similar to the RIS. In my coupled model presented here I find this value to be up to ∼12% near the grounding line. This effect could lead to interesting feedbacks between tides and ice-streams if the ocean tide was to change.

The effect of changes in ice-shelf geometry and/or extent on regional ocean tides is investigated using the OTIS tidal model. I first compare present day OTIS simulations of the Antarctic region with the CATS2008 model and find that there is generally good agreement between the two models. I then introduce a number of simple ice-shelf perturbation scenarios which reduce the Ross and Filchner-Ronne ice-shelves and examine the tidal response. A key result of these experiments is that the semidiurnal tide beneath the FRIS is altered considerably as reducing the ice-shelf causes the large Weddel Sea amphidromic point to shift. The cause in this shift is an increase in tidal dissipation on the Weddel Sea shelf break . Diurnal tides are generally found to be less sensitive although some large changes occur in Ross sea sector when a grounding line retreat scenario derived from PISM-PIK is used.

9.2 Future Work

Although the model results presented in this thesis attempt to answer some of the open questions regarding tidal interactions with ice-shelves and ice-streams, there remains much scope for improvement both in terms of more complete data acquisition of these processes and more advanced models to tackle the questions raised in the data.

9.2.1 Observational work

Much of the work in this thesis is based on trying to understand an affect from fairly limited observations. To date the only published data showing M_{sf} modulation in ice-stream flow is from the RIS. Observations were made on the nearby Evans

ice-stream with a similar deployment of GPS stations and analysis of these data shows a similar M_{sf} response but this work remains unpublished [Gudmundsson]. More measurements are needed to further constrain certain key features of the M_{sf} response that are not sufficiently clear in the existing data.

One of the most interesting aspects of the RIS GPS measurements is that the semidiurnal tidal constituents, which are large at the GL, decay rapidly upstream. The existing data arguably does not have sufficient accuracy or spatial resolution to produce a clear picture of the decay length scale of semidiurnal constituents. In particular, being able to precisely pick out the phase of the semidiurnal component of horizontal ice-stream motion would immediately shine light on which processes dominate at the GL. Interpretation of the existing data is complicated by the fact that the RIS GL wraps around near the local GPS sites leading to ambiguity when it is compared to the idealised model with a straight GL. If hydrology (and possibly to some extent GL migration) dominate, as predicted by work in Chapter 6, then ice-stream velocities at the GL would be highest at high tide when effective pressure is lowest. Conversely, if a nonlinear relation to basal stress is the primary cause of long period modulation ice-stream velocities would be highest at low tide.

The clearest answer as to whether or not tidal perturbations in basal hydrology are sufficiently large, and effective pressure sufficiently low, to explain the M_{sf} response would be to drill to the base of the RIS. Drilling to this depth and making measurements of basal water pressure would be technically and logistically challenging, but has been successfully carried out in the past on the Siple coast [Engelhardt et al., 1990], and would be of great interest to a wide variety of fields. Based on the modeling work presented here, fluctuations in basal water pressure at tidal frequencies should be observed tens of kilometers inland of the GL. The only caveat to this is that it is not clear whether these are transmitted through a small number of channels or a more distributed network and thus if the former is the case boreholes could potentially be drilled into regions where there is very little hydrological activity.

Data from the RIS shows a possible amplification of the M_{sf} modulation occurring downstream of the GL, although the error bars in the data are too large to say this for certain. If this were the case an additional effect would be needed, since none of the mechanisms I have presented could explain an increase in M_{sf} response on the ice-shelf. Even for an infinitely wide ice-shelf with no side drag, which is certainly not the case in either the 3D model or the RIS itself, the M_{sf} response would be expected to remain constant downstream rather than increase. One possible explanation is that the nonlinear rheology of the ice-shelf could lead to a nonlinear response in flow of sufficient amplitude to be visible in the data. In a similar way to the production of M_{sf} modulation as a result of interaction at the bed with a sliding law using $m > 3$, in the downstream case it would be generated by sidewall friction using $n > 1$. More measurements of ice-shelf flow downstream of the grounding line where ice-streams are subjected to large semidiurnal tides would be necessary to determine whether this amplification exists or not.

9.2.2 Model improvements

In terms of modeling efforts, there is plenty of scope for improving the existing models outlined in this thesis. All ice modeling results presented use a highly idealised ice-stream geometry with constant bed and surface slopes and no transverse variation in geometry. It is possible that features such as an over-deepening could play a role in both stress transmission or in acting as a barrier to water pressure changes generated at the GL. In addition, all results in which the GL was allowed to migrate were limited to idealised 2D geometries. This prevents any real conclusions being drawn about the role that GL migration actually play in generating M_{sf} modulation in flow, since the actual RIS geometry may not be conducive to large migration and important processes such as lateral drag are missing.

The next step, to provide the closest possible comparison with data, would be a 3D FS visco-elastic model with migrating grounding line, real ice-stream geometry and inversion of basal slipperiness. This would enable firm statements to be made

about precisely what mechanism best matches the observations for a given ice-stream. A long term goal might be to use this type of model to infer details about the subglacial hydrology such as the type of drainage network for a given ice-stream. Even before future observational work is carried, a more complete model of this form could be used to make a detailed investigation of expected phase characteristics for the various tidal frequencies, providing useful information on where to place GPS sites to gain the most useful diagnostic information on the tidal modulation in flow.

One feature of the observations that all versions of the model presented have struggled to replicate is the very rapid decay of semidiurnal constituents upstream of the GL. The most obvious explanation is that the simple Maxwell rheology is the problem and using a more complex rheological model might improve this aspect of the results. In addition, many other formulations exist to relate viscous stress and strain rate and it may be that using an alternative relation than the simple Glen's flow law might also solve this issue.

An interesting model study would be to investigate the role that tides play in weakening ice in the grounding zone through flexure, thus potentially promoting calving further downstream. The MSC Marc model is capable of modeling material crack formation and growth and could be a valuable tool to determine the importance of this effect which has never been quantified and how it might change if the local tide is altered.

Tidal modeling in this region also has room for improvement, due to the complication of the presence of ice-shelves. There remain large gaps in data for bathymetry beneath ice-shelves, leading to uncertainties in the tidal model which is highly sensitive to these types of error. Ice-shelf flexure is also not included in tidal models, and is likely to contribute somewhat to dissipation of tidal energy in this region. While the CATS2008 model compensates for these uncertainties with inverse methods, this type of approach would not work when investigating perturbations in the ice-shelf geometry. An advanced model including solid-fluid interactions is needed to fully capture the tidal processes beneath larger Antarctic ice-shelves.

9.3 Closing comments

The Antarctic ice-sheet is sensitive to changes in the oceanic forcing at its boundaries. The most obvious and extensively studied of these processes is long term changes in sub ice-shelf temperatures causing enhanced melting and accelerating ice loss from the continent. Ocean tides are also an important forcing to consider, affecting both short and long term ice flow. I have chosen to investigate two aspects of this forcing.

Firstly I investigate the M_{sf} modulation of ice-stream flow. The primary goal of this work is to gain an insight into the basal sliding processes that must occurring to produce this effect, rather than understanding the effect itself. In this context, the work presented here is relevant to all ice flow modeling, for which the basal sliding law is a source of uncertainty. Constraining the basal sliding law is not a simple case of providing a catch-all number for m and q that can be applied to all Antarctic ice-streams. A very general sliding law of this form is unlikely to be developed in the near future, however the tides can act as a natural experiment to provide a unique insight into basal processes which are still largely unknown.

The second portion of work attempts to predict how tides might change in response to perturbations in the two largest Antarctic ice-shelves. Ocean megatides have been cited as a possible cause of ice-sheet breakup in the past and, while it would be more than a stretch to suggest that this is likely in present day Antarctica, changing tides certainly could have a role to play in the evolution of the AIS. Changes in ice-shelf geometry have been shown to lead to changes in both tidal amplitude and dissipation, with implications for sub ice-shelf melt rates, ice damage in the flexural zone and the mean flow of ice-streams.

Appendix A

3D coupled model stresses

Contained within this appendix are plan view figures of various deviatoric stress components at high and low tide. The deviatoric stresses are shown seperately at the surface and the bed of the ice to highlight the differences between the two. Bending stresses dominate the longitudinal deviatoric stress signal at both the surface and the bed, and the nodes at which these stresses reverse sign are seen up and downstream of the grounding line. Transverse stresses are greatest along the edge of the domain where ice accelerates once it begins floating.

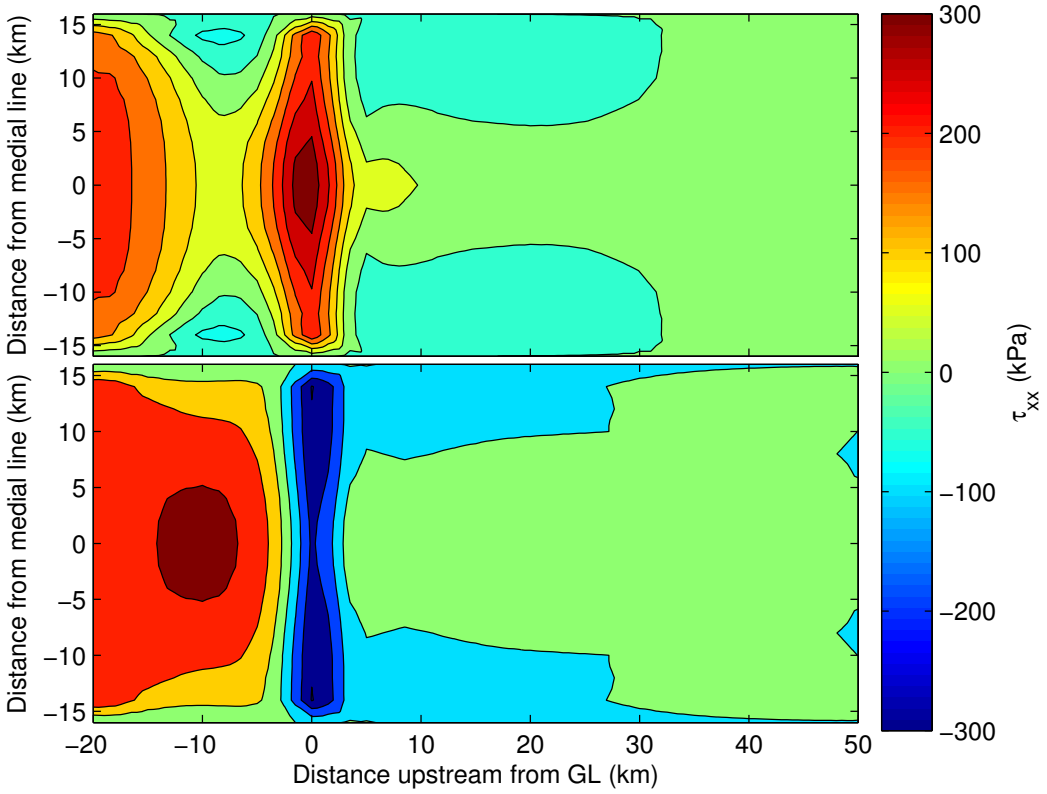

FIGURE A.1: Distribution in modeled surface longitudinal deviatoric stresses τ_{xx} (kPa) for low tide (upper panel) and high tide (lower panel).

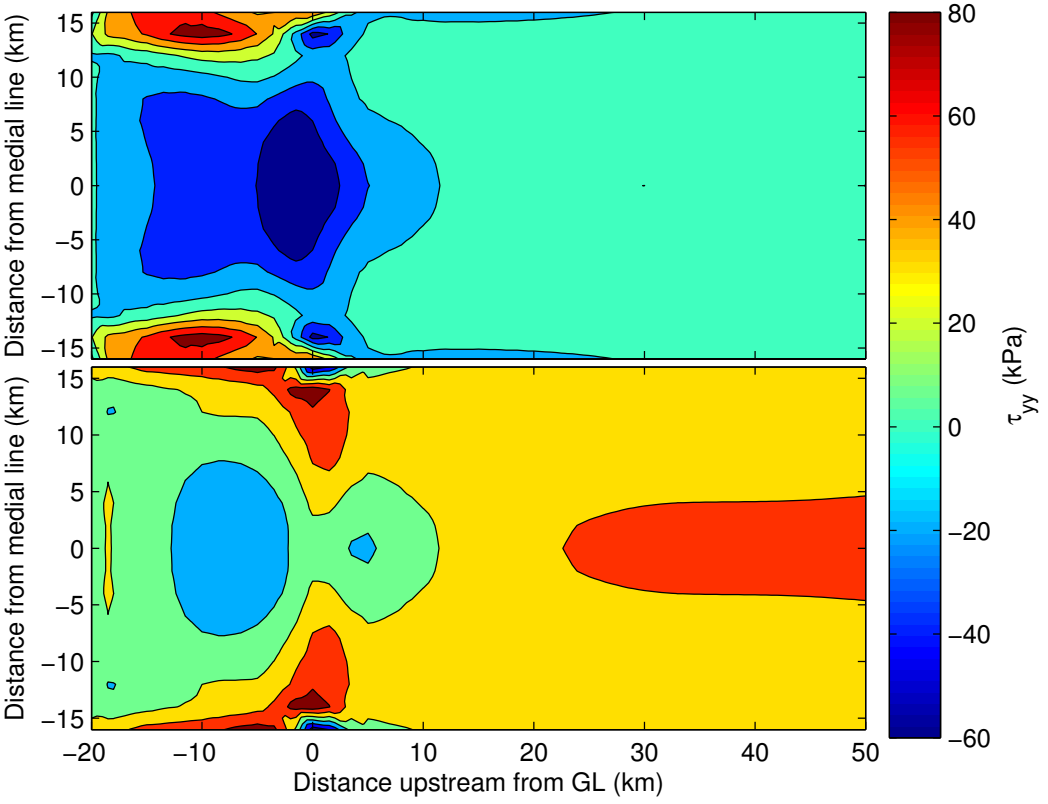

FIGURE A.2: Distribution in modeled surface transverse deviatoric stresses τ_{yy} (kPa) for low tide (upper panel) and high tide (lower panel).

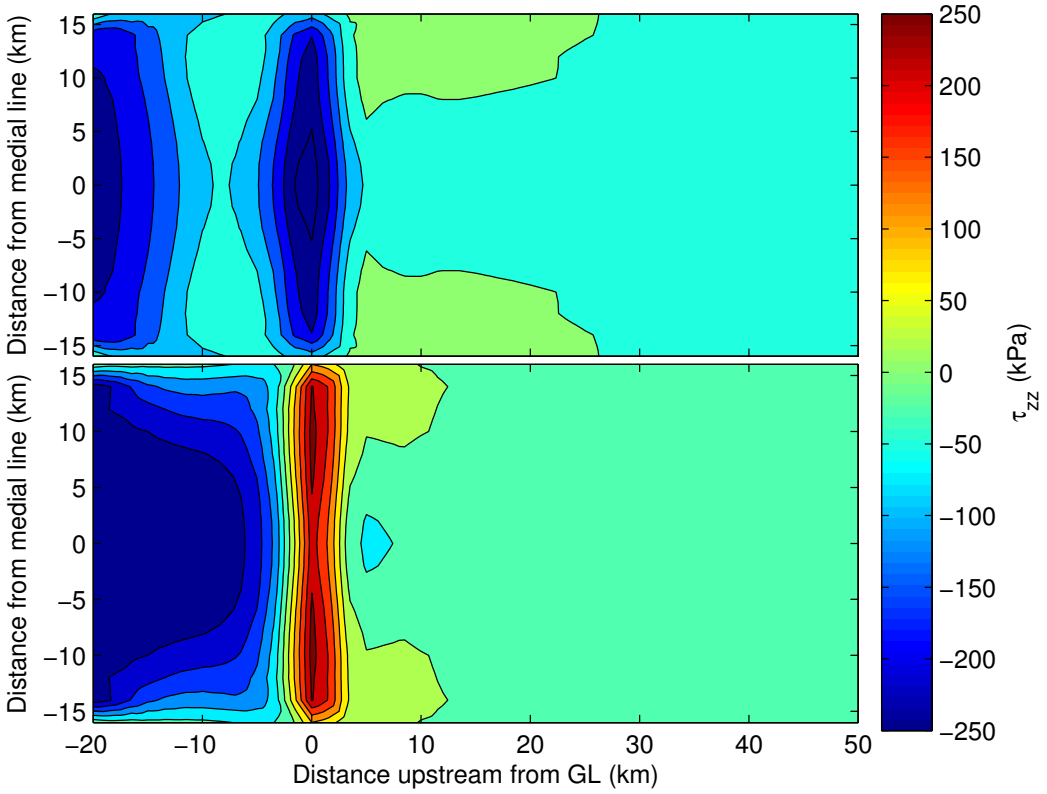

FIGURE A.3: Distribution in modeled surface vertical deviatoric stresses τ_{zz} (kPa) for low tide (upper panel) and high tide (lower panel).

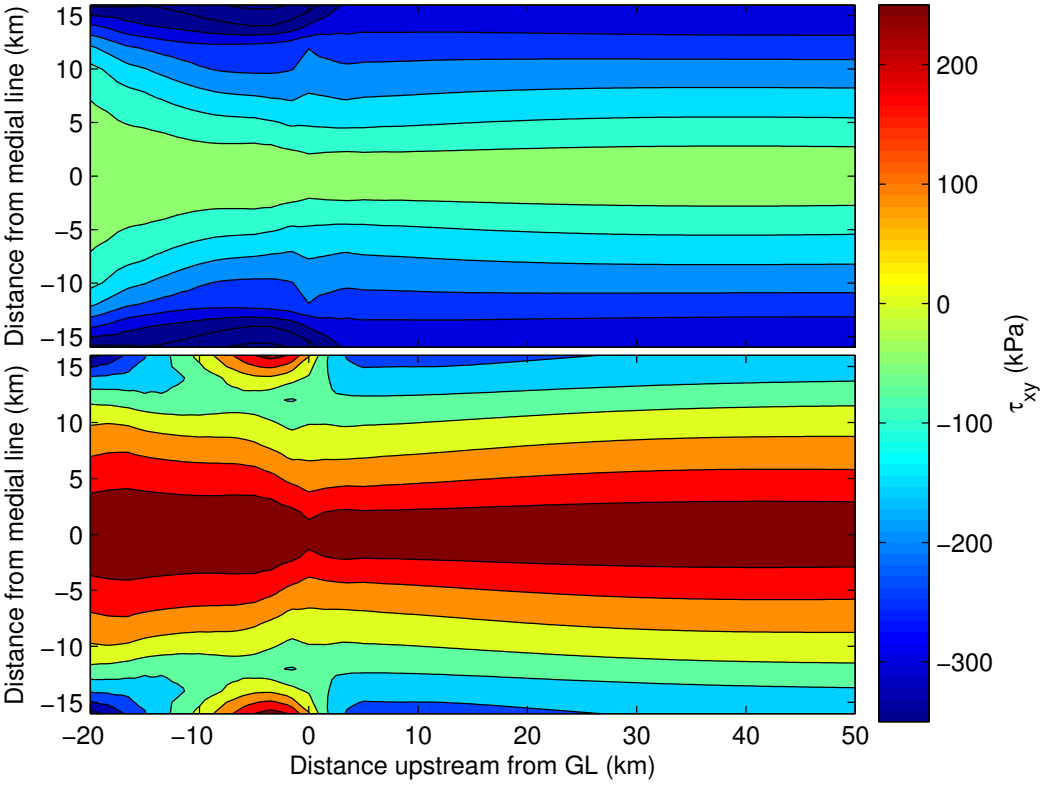

FIGURE A.4: Distribution in modeled surface transverse shear deviatoric stresses τ_{xy} (kPa) for low tide (upper panel) and high tide (lower panel).

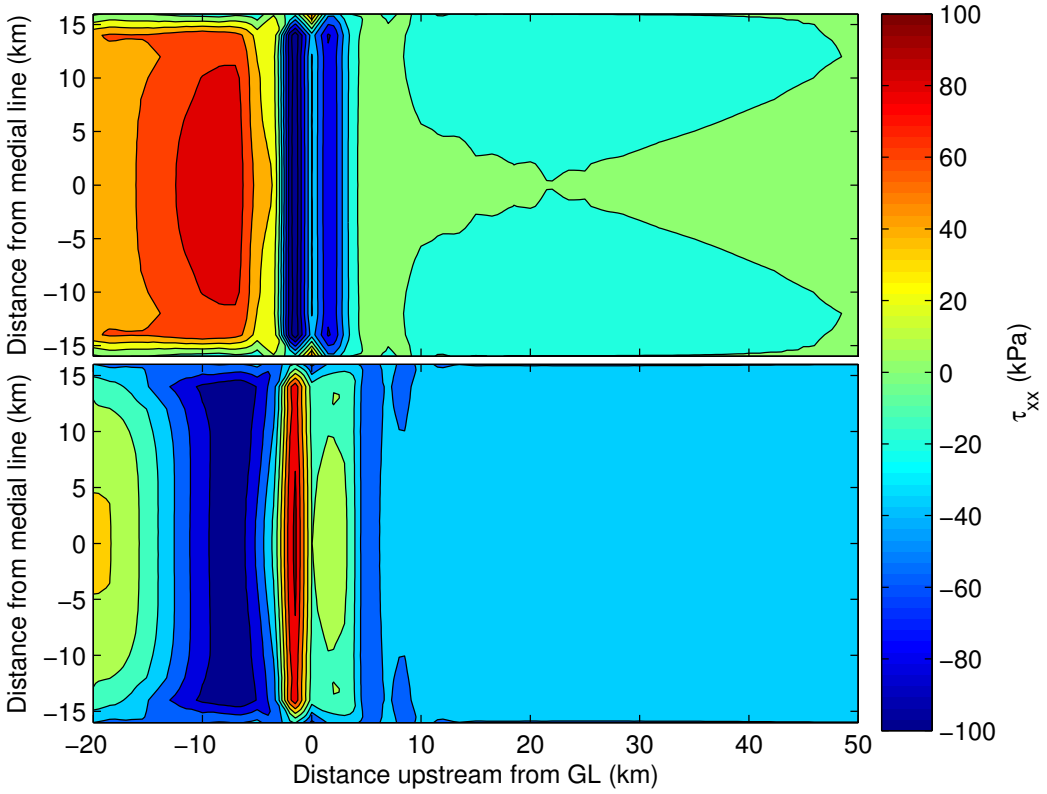

FIGURE A.5: Distribution in modeled basal longitudinal deviatoric stresses τ_{xx} (kPa) for low tide (upper panel) and high tide (lower panel).

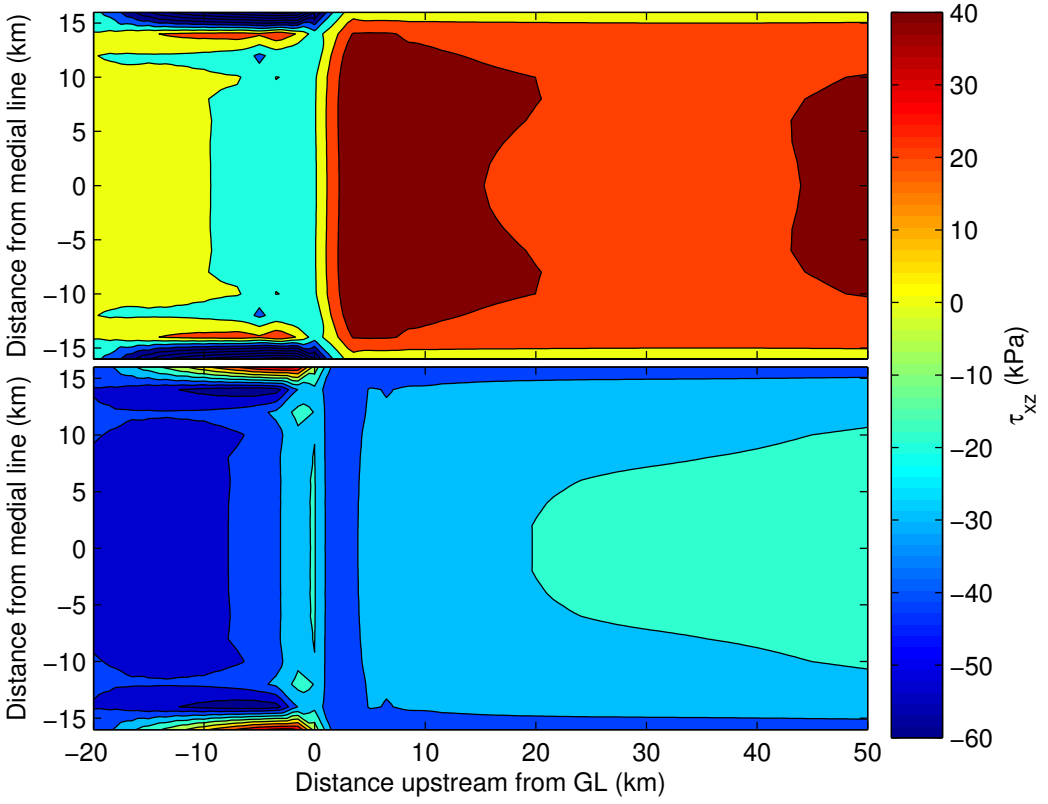

FIGURE A.6: Distribution in modeled basal vertical shear deviatoric stresses τ_{xz} (kPa) for low tide (upper panel) and high tide (lower panel).

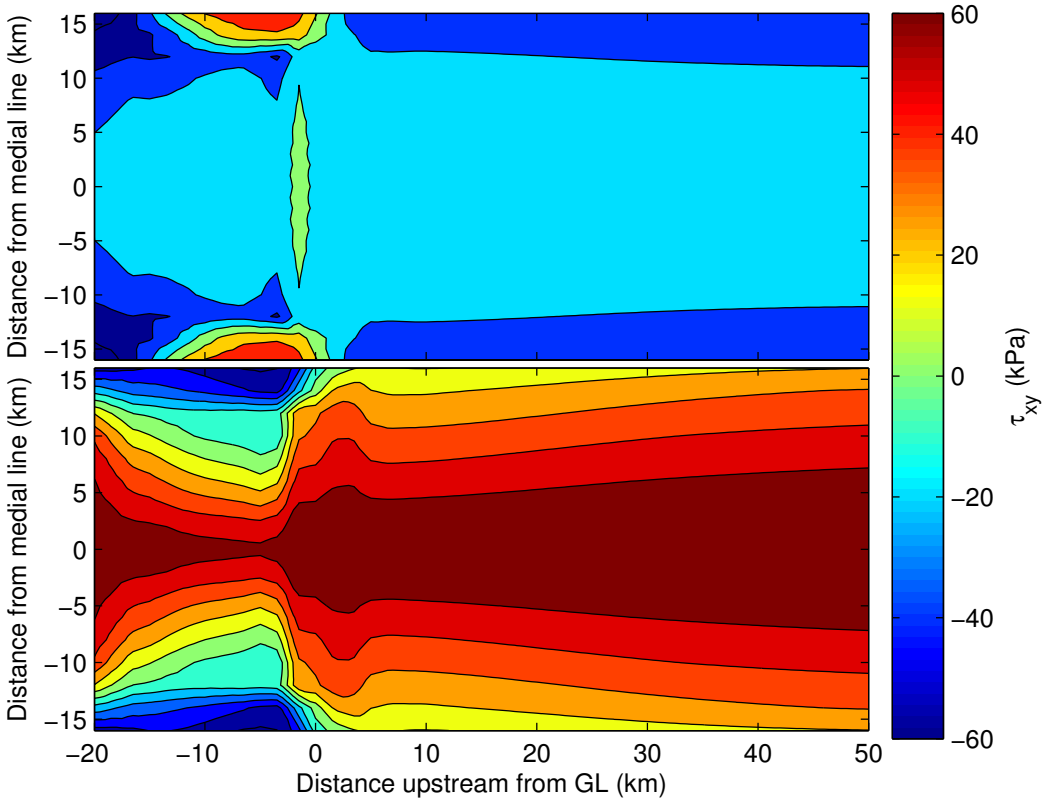

FIGURE A.7: Distribution in modeled basal trasverse shear deviatoric stresses τ_{xy} (kPa) for low tide (upper panel) and high tide (lower panel).

Bibliography

Aðalgeirsdóttir, G., Smith, A. M., Murray, T., King, M. A., Makinson, K., Nicholls, K. W., and Behar, A. E.: Tidal influence on Rutford Ice Stream, West Antarctica: observations of surface flow and basal processes from closely-spaced GPS and passive seismic stations, J. Glaciol., 54, 715–724, doi:10.3189/002214308786570872, 2008.

Alley, R. B., Blankenship, D. D., Bentley, C. R., and Rooney, S. T.: Deformation of till beneath ice stream B, West Antarctica, Nature, 322, 57–59, 1986.

Anandakrishnan, S. and Alley, R.: Tidal forcing of basal seismicity of ice stream C, West Antarctica, observed far inland, J.Geophys. Res., 102, 15,813–15,196, doi:10.1029/97JB01073, 1997.

Anandakrishnan, S., Voigt, D. E., and Alley, R. B.: Ice stream D flow speed is strongly modulated by the tide beneath the Ross Ice Shelf, Geophys. Res. Lett., 30, 1361, doi:DOI:10.1029/2002GL016329, 2003.

Arbic, B., Garner, S., Hallberg, R., and Simmons, H. L.: The accuracy of surface elevations in forward global barotropic and baroclinic tide models, Deep-Sea Research II, 51, 3069–3101, doi:10.1016/j.dsr2.2004.09.014, 2004a.

Arbic, B. K., MacAeal, D. R., Mitrovica, J. X., and Milne, G. A.: Paleoclimate - ocean tides and Heinrich events, nature, 432, 460, doi:10.1038/432460a, 2004b.

Arbic, B. K., Mitrovica, J. X., MacAyeal, D. R., and Milne, G. A.: On the factors behind large Labrador Sea tides during the last glacial cycle and the potential implications for Heinrich events, Paleoceanography, 23, PA3211, doi:10.1029/2007PA001573, 2008.

Arbic, B. K.and Karseten, R. H. and Garret, C.: On tidal resonance in the global ocean and the back-effect of coastal tides upon open-ocean tides, Atmosphere-Ocean, 47, 239–266, doi:10.3137/OC311.2009, 2009.

Bamber, J. L., Alley, R. B., and Joughin, I.: Rapid response of modern day ice sheets to external forcing, Earth Planet. Sci. Lett., 257, 1–13, doi:10.1016/j.epsl.2007.03.005, 2007.

Benn, D. and Evans, D. J. A.: Glaciers and Glaciation, Hodder Arnold Publication, 57 Shelton street, Covent garden, London, WC2H 9HE, 2010.

Bennett, M. R.: Ice streams as the arteries of an ice sheet: their mechanics, stability and significance, Earth-Science Reviews, 61, 309 – 339, doi:10.1016/S0012-8252(02)00130-7, 2003.

Berthier, E., Scambos, T. A., and Shuman, C. A.: Mass loss of Larsen B tributary glaciers (Antarctic Peninsula) unabated since 2002, Geophysical Research Letters, 39, 2012.

Bindschadler, R.: The importance of pressurized subglacial water in separation and sliding at the glacier bed, Journal of Glaciology, 29, 3–19, 1983.

Bindschadler, R. A., King, M. A., Alley, R. B., Anandakrishnan, S., and Padman, L.: Tidally controlled stick-slip discharge of a West Antasrctic ice stream, Science, 301, 1087–1089, doi:10.1126/science.1087231, 2003a.

Bindschadler, R. A., Vornberger, P. L., King, M. A., and Padman, L.: Tidally driven stickslip motion in the mouth of Whillans Ice Stream, Antarctica, Ann. Glaciol., 36, 263–272, doi:10.3189/172756403781816284, 2003b.

Brunt, K. M.: Tidal motion of the Ross Ice Shelf and its interaction with the Siple Coast ice streams, Antarctica, Ph.D. thesis, University of Chicago, 2008.

Brunt, K. M., King, M. A., Fricker, H. A., and Macayeal, D. R.: Flow of the Ross Ice Shelf, Antarctica, is modulated by the ocean tide, J. Glaciol., 56, 157–161, 2010.

Brunt, K. M., Fricker, H. A., and Padman, L.: Analysis of ice plains of the Filchner-Ronne Ice Shelf, Antarctica, using ICESat laser altimetry, J. Glaciol., 57, 965–975, 2011.

Budd, W. F. and Keage, P. L.: Empirical studies of ice sliding, Journal of glaciology, 23, 157–170, 1979.

Cuffey, K. M. and Patterson, W. S. B.: The Physics of Glaciers, Fourth Edition, Butterworth-Heineman, 30 Corporate Drive, Suite 400, Burlington, MA 01803, USA, 2010.

Dach, R., Beutler, G., and Gudmundsson, G.: Analysis of GPS Data from An Antarctic Ice Stream, in: Observing our Changing Earth, edited by Sideris, M. G., vol. 133 of *International Association of Geodesy Symposia*, pp. 569–579, Springer Berlin Heidelberg, doi:10.1007/978-3-540-85426-5_67, URL `http://dx.doi.org/10.1007/978-3-540-85426-5_67`, 2009.

Davis, C. H., Li, Y., McConnell, J. R., Frey, M. M., and Hanna, E.: Snowfall-Driven Growth in East Antarctic Ice Sheet Mitigates Recent Sea-Level Rise, Science, 308, 1898–1901, doi:10.1126/science.1110662, 2005.

de Fleurian, B., Gagliardini, A., Zwinger, T., Durand, G., Le Meur, E., Mair, D., and Råback, P.: A double continuum hydrological model for glacier applications, The Cryosphere, 8, 137–153, doi:10.5194/tc-8-137-2014, 2014.

Doake, C. S. M., Frolich, R. M., Mantripp, D. R., Smith, A. M., and Vaughan, D. G.: Glaciological studies on Rutford ice stream, Antarctica, J. Geophys. Res., 92, 8951–8960, 1987.

Doake, C. S. M., Corr, H. F. J., Jenkins, A., Makinson, K., Nicholls, K. W., Nath, C., Smith, A. M., and Vaughan, D. G.: Rutford ice stream, Antarctica, Antarctic Research Series, 77, 221–235, 2001.

Doake, C. S. M., Corr, H. F. J., Nicholls, K. W., Gaffikin, A., Jenkins, A., Bertiger, W. I., and King, M. A.: Tide-induced lateral movement of Brunt Ice Shelf, Antarctica, Geophys. Res. Lett., 29, 2002.

Dupont, T. K. and Alley, R. B.: Assessment of the importance of ice-shelf buttressing to ice-sheet flow, Geophysical Research Letters, 32, L04 503, doi: 10.1029/2004GL022024, 2005.

Dupont, T. K. and Alley, R. B.: Role of Small Ice Shelves in Sea-level Rise, pp. 1–4, American Geophysical Union, doi:10.1002/9781118782033.ch18, 2006.

Egbert, G. D. and Erofeeva, S. Y.: Efficient ocean modeling of barotropic ocean tides, Journal of atmosphere and ocean technology, 19, 183–204, doi:10.1175/1520-0426, 2002.

Egbert, G. D. and Ray, R. D.: Estimates of M2 tidal energy dissipation from TOPEX/Poseidon altimeter data, Journal of Geophysical Research: Oceans, 106, 22 475–22 502, doi:10.1029/2000JC000699, 2001.

Egbert, G. D., Ray, R. D., and Bills, B. G.: Numerical modeling of the global semidiurnal tide in the present day and in the last glacial maximum, Journal of Geophysical Research: Oceans, 109, doi:10.1029/2003JC001973, 2004.

Engelhardt, H. and Kamb, B.: Basal sliding of ice stream B, West Antarctica, J. Glaciol., 44, 223–230, 1998.

Engelhardt, H., Humphrey, N., Kamb, B., and Fahnestock, M.: Physical Conditions at the Base of a Fast Moving Antarctic Ice Stream, Science, 248, 57–59, 1990.

Fluckiger, J., Knutti, R., and White, J. W. C.: Oceanic processes as potential trigger and amplifying mechanisms for Heinrich Events, Paleoceanography, 21, doi:10.1029/2005PA001204, 2006.

Fountain, A. G. and Walder, J. S.: Water flow through temperate glaciers, Reviews of geophysics, 36, 299–328, 1998.

Fretwell, P., Pritchard, H. D., Vaughan, D. G., Bamber, J. L., Barrand, N. E., Bell, R., Bianchi, C., Bingham, R. G., Blankenship, D. D., Casassa, G., Catania, G., Callens, D., Conway, H., Cook, A. J., Corr, H. F. J., Damaske, D., Damm, V., Ferraccioli, F., Forsberg, R., Fujita, S., Gim, Y., Gogineni, P., Griggs, J. A.,

Hindmarsh, R. C. A., Holmlund, P., Holt, J. W., Jacobel, R. W., Jenkins, A., Jokat, W., Jordan, T., King, E. C., Kohler, J., Krabill, W., Riger-Kusk, M., Langley, K. A., Leitchenkov, G., Leuschen, C., Luyendyk, B. P., Matsuoka, K., Mouginot, J., Nitsche, F. O., Nogi, Y., Nost, O. A., Popov, S. V., Rignot, E., Rippin, D. M., Rivera, A., Roberts, J., Ross, N., Siegert, M. J., Smith, A. M., Steinhage, D., Studinger, M., Sun, B., Tinto, B. K., Welch, B. C., Wilson, D., Young, D. A., Xiangbin, C., and Zirizzotti, A.: Bedmap2: improved ice bed, surface and thickness datasets for Antarctica, The Cryosphere, 7, 375–393, doi:10.5194/tc-7-375-2013, 2013.

Fricker, H. A. and Padman, L.: Tides on Filchner-Ronne Ice Shelf from ERS radar altimetry, Geophys. Res. Lett., 29, 2002.

Fricker, H. A. and Padman, L.: Ice shelf grounding zone structure from ICESat laser altimetry, Geophysical Research Letters, 33, L15 502, doi:10.1029/2006GL026907, 2006.

Fricker, H. A., Coleman, R., Padman, L., Scambos, T. A., Bohlander, J., and Brunt, K. M.: Mapping the grounding zone of the Amery Ice Shelf, East Antarctica using InSAR, MODIS and ICESat, Antarctic Science, 21, 515–532, doi:10.1017/S095410200999023X, 2009.

Glasser, N., Scambos, T., Bohlander, J., Truffer, M., Pettit, E., and Davies, B.: From ice-shelf tributary to tidewater glacier: continued rapid recession, acceleration and thinning of Röhss Glacier following the 1995 collapse of the Prince Gustav Ice Shelf, Antarctic Peninsula, Journal of Glaciology, 57, 397–406, doi: doi:10.3189/002214311796905578, 2011.

Glasser, N. F. and Scambos, T. A.: A structural glaciological analysis of the 2002 Larsen B ice shelf collapse, Journal of Glaciology, 54, 3–16, doi:10.3189/002214308784409017, 2008.

Glen, J. W.: The creep of polycrystalline ice, Proceedings of the Royal Society, Series A, 228, 519–538, 1955.

Goldberg, D., Holland, D. M., and Schoof, C.: Grounding line movement and ice shelf buttressing in marine ice sheets, Journal of Geophysical Research: Earth Surface, 114, F04 026, doi:10.1029/2008JF001227, 2009.

Gray, L., Short, N., Bindschadler, R., Joughin, I., Padman, L., Vornberger, P., and Khananian, A.: RADARSAT interferometry for Antarctic grounding-zone mapping, Annals of Glaciology, 34, 269–276, doi:doi:10.3189/172756402781817879, 2002.

Green, J. A. M.: Ocean tides and resonance, ocean dynamics, 60, 1243–1253, doi:10.1007/s10236-010-0331-1, 2010.

Green, J. A. M. and Huber, M.: Tidal dissipation in the early Eocene and implications for ocean mixing, Geophysical Research Letters, 40, doi:10.1002/grl.50510, 2013.

Green, J. A. M. and Nycander, J.: A comparison of internal wave-drag parameterizations for tidal models, Journal of Physical Oceanography, 43, doi: 10.1175/JPO-D-12-023.1, 2013.

Griffiths, S. D. and Peltier, R. W.: Modeling of Polar Ocean Tides at the Last Glacial Maximum: Amplification, Sensitivity and Climatological Implications, Journal of Climate, 22, 2905–2924, doi:10.1175/2008JCLI2540.1, 2009.

Gudmundsson, G. H.: personal communication.

Gudmundsson, G. H.: Transmission of basal variability to a glacier surface, J. Geophys. Res.: Sol. Ea., 108, 2003.

Gudmundsson, G. H.: Fortnightly variations in the flow velocity of Rutford Ice Stream, West Antarctica., Nature, 444, 1063–4, doi:doi:10.1038/nature05430, 2006.

Gudmundsson, G. H.: Tides and the flow of Rutford Ice Stream, West Antarctica, J. Geophys. Res., 112, F04 007, doi:10.1029/2006JF000731, 2007.

Gudmundsson, G. H.: Ice-stream response to ocean tides and the form of the basal sliding law, The Cryosphere, 5, 259–270, doi:10.5194/tc-5-259-2011, 2011.

Gudmundsson, G. H.: Ice-shelf buttressing and the stability of marine ice sheets, The Cryosphere, 7, 647–655, doi:10.5194/tc-7-647-2013, 2013.

Gudmundsson, G. H. and Raymond, M. J.: On the limit to resolution and information on basal properties obtainable from surface data on ice streams, The Cryosphere, 2, 167–178, doi:10.5194/tc-2-167-2008, 2008.

Gudmundsson, G. H., Krug, J., Durand, G., Favier, L., and Gagliardini, O.: The stability of grounding lines on retrograde slopes, The Cryosphere, 6, 1497–1505, doi:10.5194/tc-6-1497-2012, 2012.

Harrison, W. D.: Short-period observations of speed, strain and seismicity on Ice Stream B, Antarctica, J. Glaciol., 39, 463–470, 1993.

Heinert, M. and Riedel, B.: Parametric modelling of the geometrical ice-ocean interaction in the Ekstroemisen grounding zone based on short time-series, Geophys. J. Int., 169, 407–420, 2007.

Hellmer, H. H., K. F. T. R. D. J. and Rae, J.: Twenty-first-century warming of a large Antarctic ice-shelf cavity by a redirected coastal current, Nature, 485, 225–228, doi:10.1038/nature11064, 2012.

Hemming, S. R.: Heinrich events: Massive late Pleistocene detritus layers of the North Atlantic and their global climate imprint, Reviews of Geophysics, 42, doi:10.1029/2003RG000128, 2004.

Holdsworth, G.: Flexure of a floating ice tongue, J. Glaciol., 8, 133–397, 1969.

Holdsworth, G.: Tidal interaction with ice shelves, Ann. Geophys., 33, 133–146, 1977.

Hulbe, C. L., Scambos, T. A., Youngberg, T., and Lamb, A. K.: Patterns of glacier response to disintegration of the Larsen B ice shelf, Antarctic Peninsula, Global and Planetary Change, 63, 1 – 8, doi:10.1016/j.gloplacha.2008.04.001, 2008.

Katz, R. F. and Worster, M. G.: Stability of ice-sheet grounding lines, Proceedings of the Royal Society of London A: Mathematical, Physical and Engineering Sciences, 466, 1597–1620, doi:10.1098/rspa.2009.0434, 2010.

Khazendar, A., Borstad, C. P., Scheuchl, B., Rignot, E., and Seroussi, H.: The evolving instability of the remnant Larsen B Ice Shelf and its tributary glaciers, Earth and Planetary Science Letters, doi:10.1016/j.epsl.2015.03.014, 2015.

King, E. C., Woodward, J., and Smith, A. M.: Seismic evidence for a water-filled canal in deforming till beneath Rutford Ice Stream, West Antarctica, Geophysical Research Letters, 31, L20 401, doi:doi:10.1029/2004GL020379, 2004.

King, M. and Aoki, S.: Tidal observations on floating ice using a single GPS receiver, Geophysical Research Letters, 30, doi:10.1029/2002GL016182, 2003.

King, M., Penna, N. T., Clarke, P. J., and King, E. C.: Validation of ocean tide models around Antarctica using onshore GPS and gravity data, Journal of Geophysical Research, 110, B08 401, doi:10.1029/2004JB003390, 2005.

King, M. A. and Padman, L.: Accuracy assessment of ocean tide models around Antarctica, Geophysical Research Letters, 32, L23 608, doi:10.1029/2005GL023901, 2005.

King, M. A., Murray, T., and Smith, A. M.: Non-linear responses of Rutford Ice Stream, Antarctica, to semi-diurnal and diurnal tidal forcing, J. Glaciol., 56, 167–176, doi:10.3189/002214310791190848, 2010.

King, M. A., Makinson, K., and Gudmundsson, G. H.: Nonlinear interaction between ocean tides and the Larsen C Ice Shelf system, Geophys. Res. Lett., 38, 1–5, doi:10.1029/2011GL046680, 2011.

Lingle, C. S., Hughes, T. J., and Kollmeyer, R. C.: Tidal flexure of Jakobshavns Glacier, west Greenland, Journal of Geophysical Research: Solid Earth, 86, 3960–3968, doi:10.1029/JB086iB05p03960, 1981.

Lythe, M. B. and Vaughan, D. G.: BEDMAP: A new ice thickness and subglacial topographic model of Antarctica, Journal of Geophysical Research: Solid Earth, 106, 11 335–11 351, doi:10.1029/2000JB900449, 2001.

MacAyeal, D. R.: Numerical simulations of the Ross Sea tides, Journal of Geophysical Research: Oceans, 89, 607–615, doi:10.1029/JC089iC01p00607, 1984.

MacAyeal, D. R.: Large-scale ice flow over a viscous basal sediment: Theory and application to ice stream B, Antarctica, Journal of Geophysical Research: Solid Earth, 94, 4071–4087, doi:10.1029/JB094iB04p04071, 1989.

Makinson, K., Holland, P. R., Jenkins, A., Nicholls, K. W., and Holland, D. M.: Influence of tides on melting and freezing beneath Filchner-Ronne Ice Shelf, Antarctica, Geophys. Res. Lett., 38, L06 601, 2011.

Makinson, K., King, M. A., Nicholls, K. W., and Gudmundsson, G. H.: Diurnal and semidiurnal tide-induced lateral movement of Ronne Ice Shelf, Antarctica, Geophys. Res. Lett., 39, L10 501, 2012.

MARC: Marc users manual, MSC Software Corporation, 2 MacArthur Place, Santa Ana, CA 92707, USA, 2013.

Marsh, O. J., Rack, W., Floricioiu, D., Golledge, N. R., and Lawson, W.: Tidally induced velocity variations of the Beardmore Glacier, Antarctica, and their representation in satellite measurements of ice velocity, The Cryosphere, 7, 1375–1384, doi:10.5194/tc-7-1375-2013, 2013.

Marsh, O. J., Rack, W., Golledge, N. R., Lawson, W., and Floricioiu, D.: Grounding-zone ice thickness from InSAR: inverse modelling of tidal elastic bending, Journal of Glaciology, 60, 526–536, doi:10.3189/2014JoG13J033, 2014.

Martin, M. A., Winkelmann, R., Haseloff, M., Albrecht, T., Bueler, E., Khroulev, C., and Levermann, A.: The Potsdam Parallel Ice Sheet Model (PISM-PIK), Part 2: Dynamic equilibrium simulation of the Antarctic ice sheet, The Cryosphere, 5, 727–740, doi:10.5194/tc-5-727-2011, 2011.

McIntyre, N. F.: The dynamics of ice-sheet outlets, Journal of Glaciology, 31, 99–107, 1985.

Meinshausen, M., Smith, S., Calvin, K., Daniel, J., Kainuma, M., Lamarque, J.-F., Matsumoto, K., Montzka, S., Raper, S., Riahi, K., Thomson, A., Velders, G., and van Vuuren, D.: The RCP greenhouse gas concentrations and their

extensions from 1765 to 2300, Climatic Change, 109, 213–241, doi:10.1007/s10584-011-0156-z, 2011.

Mellor, M. and Testa, R.: Creep of ice under low stress, Journal of glaciology, 8, 147–152, 1969.

Mercer, J. H.: West Antarctic ice sheet and CO2 greenhouse effect: a threat of disaster, Nature, 271, 321–325, doi:10.1038/271321a0, 1978.

Morland, L. W.: Thermomechanical balances of ice sheet flows, Geophysical & Astrophysical Fluid Dynamics, 29, 237–266, doi:10.1080/03091928408248191, 1984.

Mueller, R. D., Padman, L., Dinniman, M. S., Erofeeva, S. Y., Fricker, H. A., and King, M. A.: Impact of tide-topography interactions on basal melting of Larsen C Ice Shelf, Antarctica, Journal of Geophysical Research, 117, C05 005, doi:10.1029/2011JCO07263, 2012.

Murray, T., Smith, A. M., King, M. A., and Weedon, G. P.: Ice flow modulated by tides at up to annual periods at Rutford Ice Stream, West Antarctica, Geophys. Res. Lett., 34, 6–11, doi:10.1029/2007GL031207, 2007.

Murray, T., Corr, H., Forieri, A., and Smith, A. M.: Contrasts in hydrology between regions of basal deformation and sliding beneath Rutford Ice Stream, West Antarctica, mapped using radar and seismic data, Geophysical Research Letters, 35, L12 504, doi:doi:10.1029/2008GL033681, 2008.

Muszynski, I. and Birchfield, G. E.: A coupled marine ice-stream ice-shelf model, Journal of glaciology, 33, 3–15, 1987.

Padman, L. and Fricker, H. A.: Tides on the Ross Ice Shelf observed with ICESat, Geophysical Research Letters, 32, L14 503, doi:10.1029/2005GL023214, 2005.

Padman, L., Erofeeva, S., and Joughin, I.: Tides of the Ross Sea and Ross Ice Shelf cavity, Antarctic Science, 15, 2002.

Padman, L., Erofeeva, S. Y., and Fricker, H. A.: Improving Antarctic tide models by assimilation of ICESat laser altimetry over ice shelves, Geophys. Res. Lett., 35, L22 504, doi:10.1029/2008gl035592, 2008.

Pattyn, F., Perichon, L., Durand, G., Favier, L., Gagliardini, O., Hindmarsh, R., Zwinger, T., Albrecht, T., Cornford, S. L., Docquier, D., Fürst, J., Goldberg, D., Gudmundsson, G., Humbert, A., Hütten, M., Huybrechts, P., Jouvet, G., Kleiner, T., Larour, E., Martin, D., Morlighem, M., Payne, A., Pollard, D., Rückamp, M., Rybak, O., Seroussi, H., Thoma, M., and Wilkens, N.: Grounding-line migration in plan-view marine ice-sheet models: results of the ice2sea MISMIP3d intercomparison, Journal of Glaciology, 59, 410–422, doi: 10.3189/2013JoG12J129, 2013.

Pawlowicz, R., Beardsley, B., and Lentz, S.: Classical tidal harmonic analysis including error estimates in MATLAB using T_TIDE, Comput. Geo., 28, 929–937, 2002a.

Pawlowicz, R., Beardsley, B., and Lentz, S.: classical tidal harmonic analysis including error estimates in MATLAB using T_TIDE, Computers and Geosciences, 28, 929–937, 2002b.

Pelling, H. E., Green, J. M., and Ward, S. L.: Modelling tides and sea-level rise: To flood or not to flood, Ocean Modelling, 63, 21 – 29, doi:http://dx.doi.org/10.1016/j.ocemod.2012.12.004, 2013.

Pond, S. and Pickard, G. L.: Introductory Dynamical Oceanography, 3rd Edition, Butterworth-Heinemann, Linacre House, Jordan Hill, Oxford, OX2 8DP, U.K., 2003.

Pritchard, H. D., Arthern, R. J., Vaughan, D. G., and Edwards, L. A.: Extensive dynamic thinning on the margins of the Greenland and Antarctic ice sheets, Nature, 461, 971–975, 2009.

Pritchard, H. D., Ligtenberg, S. R. M., Fricker, H. A., Vaughan, D. G., van den Broeke, M. R., and Padman, L.: Antarctic ice-sheet loss driven by basal melting of ice shelves, Nature, 484, 502–505, doi:10.1038/nature10968, 2012.

Pugh, D. T.: Tides, surges and mean sea level, Jogn Wiley and Sons Ltd., Chippenham, Wiltshire, 1996.

Rack, W. and Rott, H.: Pattern of retreat and disintegration of the Larsen B ice shelf, Antarctic Peninsula, Annals of Glaciology, 39, 505–510, 2004.

Raymond, M. J. and Gudmundsson, G. H.: Estimating basal properties of ice streams from surface measurements: a non-linear Bayesian inverse approach applied to synthetic data, The Cryosphere, 4, 265–278, doi:10.5194/tc-3-265-2009, 2009.

Reeh, N., Christensen, E. L., Mayer, C., and Olesen, O. B.: Tidal bending of glaciers: a linear viscoelastic approach, Ann. Glaciol., 37, 83–89, doi:10.3189/172756403781815663, 2003.

Rignot, E.: Radar Interferometry detection of hinge-line migration on Rutford Ice Stream and Carlson Inlet, Ann. Glaciol., 27, 25–32, 1998.

Rignot, E.: Changes in ice dynamics and mass balance of the Antarctic ice sheet, Philosophical Transactions of the Royal Society of London A: Mathematical, Physical and Engineering Sciences, 364, doi:10.1098/rsta.2006.1793, 2006.

Rignot, E. and Thomas, R. H.: Mass Balance of Polar Ice Sheets, Science, 297, 1502–1506, doi:10.1126/science.1073888, 2002.

Rignot, E., Casassa, G., Gogineni, P., Krabill, W., Rivera, A., and Thomas, R.: Accelerated ice discharge from the Antarctic Peninsula following the collapse of Larsen B ice shelf, Geophysical Research Letters, 31, n/a–n/a, doi:10.1029/2004GL020697, 2004.

Rignot, E., Mouginot, J., and Scheuchl, B.: Ice Flow of the Antarctic Ice Sheet, Science, 333, 1427–1430, doi:10.1126/science.1208336, 2011.

Rignot, E., Jacobs, S., Mouginot, J., and Scheuchl, B.: DIce-Shelf melting around Antarctica, Science, 341, 266–270, doi:10.1126/science.1235798, 2013.

Robertston, R. A., Padman, L., and Egbert, G. D.: Tides in the Weddel Sea in Ocean, Ice and Atmosphere, Interactions at the Antarctic Continental Margin, Ant. Res. Ser., AGU, Washington D. C., 1998.

Robison, R. A. V., Huppert, H. E., and Worster, G. M.: Dynamics of viscous grounding lines, Journal of Fluid Mechanics, 648, 363–380, doi:10.1017/S0022112009993119, 2010.

Rodgers, C. D.: Inverse methods for atmospheric sounding: theory and practice, World Scientific Publishing, 57 Shelton street, Covent garden, London, WC2H 9HE, 2000.

Rosier, S. H. R., Green, J. A. M., Scourse, J. D., and Winkelmann, R.: Modeling Antarctic tides in response to ice shelf thinning and retreat., J. Geophys. Res.: Oceans, 119, 87–97, doi:10.1002/2013JC009240, 2014a.

Rosier, S. H. R., Gudmundsson, G. H., and Green, J. A. M.: Insights into ice stream dynamics through modeling their response to tidal forcing, The Cryosphere, 8, 1763–1775, doi:10.5194/tc-8-1763-2014, 2014b.

Rosier, S. H. R., Gudmundsson, G. H., and Green, J. A. M.: Temporal variations in the flow of a large Antarctic ice-stream controlled by tidally induced changes in the subglacial water system, The Cryosphere Discussions, 9, 1–33, doi:10.5194/tcd-9-1-2015, 2015.

Rott, H., Skvarca, P., and Nagler, T.: Rapid collapse of Northern Larsen Ice Shelf, Antarctica, Science, 271, 788–792, doi:10.1126/science.271.5250.788, 1996.

Rott, H., Rack, W., Skvarca, P., and De Angelis, H.: Northern Larsen Ice Shelf, Antarctica: further retreat after collapse, Annals of Glaciology, 34, 277–282, doi:doi:10.3189/172756402781817716, 2002.

Rott, H., Muller, F., Nagler, T., and Floricioiu, D.: The imbalance of glaciers after disintegration of Larsen-B ice shelf, Antarctic Peninsula, The Cryopshere, 5, 125–134, doi:10.5194/tc-5-125-2011, 2011.

Sayag, R. and Worster, M. G.: Elastic response of a grounded ice sheet coupled to a floating ice shelf, Phys. Rev. E, 84, 036 111, doi:10.1103/PhysRevE.84.036111, 2011.

Sayag, R. and Worster, M. G.: Elastic dynamics and tidal migration of grounding lines modify subglacial lubrication and melting, Geophys. Res. Lett., 40, 5877–5881, doi:10.1002/2013GL057942, 2013.

Scambos, T., Haran, T., Fahnestock, M., Painter, T., and Bohlander, J.: MODIS-based Mosaic of Antarctica (MOA) data sets: Continent-wide surface morphology and snow grain size, Remote Sensing of Environment, 111, 242 – 257, doi: 10.1016/j.rse.2006.12.020, remote Sensing of the Cryosphere Special Issue, 2007.

Scambos, T. A., Bohlander, J. A., Shuman, C. A., and Skvarca, P.: Glacier acceleration and thinning after ice shelf collapse in the Larsen B embayment, Antarctica, Geophysical Research Letters, 31, 2004.

Schoof, C.: Ice sheet grounding line dynamics: Steady states, stability, and hysteresis, Journal of Geophysical Research: Earth Surface, 112, F03S28, doi: 10.1029/2006JF000664, 2007a.

Schoof, C.: Marine ice-sheet dynamics. Part 1. The case of rapid sliding, Journal of Fluid Mechanics, 573, 27–55, doi:10.1017/S0022112006003570, 2007b.

Schulson, E. M. and Duval, P.: Creep and fracture of ice, Cambridge University Press, Cambridge, CB28RU, UK, 2009.

Scott, J. B. T., Gudmundsson, G. H., Smith, A. M., Bingham, R. G., Pritchard, H. D., and Vaughan, D. G.: Increased rate of acceleration on Pine Island Glacier strongly coupled to changes in gravitational driving stress, The Cryosphere, 3, 125–131, doi:10.5194/tc-3-125-2009, 2009.

Sergienko, O. V., Macayeal, D. R., and Bindschadler, R.: Stick-slip behavior of ice streams: modeling investigations, Ann. Glaciol., 50, 87–94, 2009.

Shames, I. H. and Cozzarelli, F. A.: Elastic and Inelastic Stress Analysis, Taylor and Francis, 325 Chestnut st., Philadelphia, U.S.A., 1997.

Shepherd, A., Wingham, D., and Rignot, E.: Warm ocean is eroding West Antarctic Ice Sheet, Geophysical Research Letters, 31, L23 402, doi:10.1029/2004GL021106, 2004.

Shepherd, A., Wingham, D., Wallis, D., Giles, K., Laxon, S., and Sundal, A. V.: Recent loss of floating ice and the consequent sea level contribution, Geophysical Research Letters, 37, doi:10.1029/2010GL042496, 2010.

Shepherd, A., Ivins, E. R., A, G., Barletta, V. R., Bentley, M. J., Bettadpur, S., Briggs, K. H., Bromwich, D. H., Forsberg, R., Galin, N., Horwath, M., Jacobs, S., Joughin, I., King, M. A., Lenaerts, J. T. M., Li, J., Ligtenberg, S. R. M., Luckman, A., Luthcke, S. B., McMillan, M., Meister, R., Milne, G., Mouginot, J., Muir, A., Nicolas, J. P., Paden, J., Payne, A. J., Pritchard, H., Rignot, E., Rott, H., Sørensen, L. S., Scambos, T. A., Scheuchl, B., Schrama, E. J. O., Smith, B., Sundal, A. V., van Angelen, J. H., van de Berg, W. J., van den Broeke, M. R., Vaughan, D. G., Velicogna, I., Wahr, J., Whitehouse, P. L., Wingham, D. J., Yi, D., Young, D., and Zwally, H. J.: A Reconciled Estimate of Ice-Sheet Mass Balance, Science, 338, 1183–1189, doi:10.1126/science.1228102, 2012.

Shuman, C. A., Berthier, E., and Scambos, T. A.: 2001-2009 elevation and mass losses in the Larsen A and B embayments, Antarctic Peninsula, Journal of Glaciology, 57, 737–754, 2011.

Smith, A. M.: The use of tiltmeters to study the dynamics of Antarctic ice-shelf grounding lines, J. Glaciol., 37, 51–58, 1991.

Smith, A. M.: Introduction to high resolution seismic surveys on Rutford Ice Stream, Filchner-Ronne Ice Shelf Programme Report No. 7, Alfred-Wegener Inst. for Polar and Mar. Res., Bremerhaven, Germany, 1994.

Smith, A. M.: Basal conditions on Rutford Ice Stream, West Antarctica, from seismic observations, Journal of Geophysical Research, 102, 543–552, 1997.

Smith, A. M., Murray, T., Nicholls, K. W., Makinson, K., Aðalgeirsdóttir, G., Behar, A. E., and Vaughan, D. G.: Rapid erosion, drumlin formation, and

changing hydrology beneath an Antarctic ice stream, Geology, 35, 127–130, 2007.

Smith, E. C., Smith, A. M., White, R. S., Brisbourne, A. M., and Pritchard, H. D.: Mapping the Ice-Bed Interface Characteristics of Rutford Ice Stream, West Antarctica, Using Microseismicity, submitted to J. Geophys. Res., 2015.

Smith, G. D.: Viscous relations for the steady creep of polycrystalline ice, Cold regions Science and Technology, 5, 141–150, 1981.

Smith, W. H. F. and Sandwell, D. T.: Global Sea Floor Topography from Satellite Altimetry and Ship Depth Soundings, Science, 277, 1956–1962, doi:10.1126/science.277.5334.1956, 1997.

Steinemann, S.: Results of preliminary experiments on the plasticity of ice crystals, Journal of Glaciology, 2, 404–413, 1954.

Steinemann, S.: Resultats experimentaux sur la dynamique de la glace et leurs correlations avec le mouvement et la petrographie des glaciers, International association of scientific hydrology, 47, 184–198, 1958.

Stephenson, S. N.: Glacier flexure and the position of grounding lines: Measurements by tiltmeter on Rutford Ice Stream Antarctica, Ann. Glaciol., 5, 165–169, 1984.

Sugiyama, S., Skvarca, P., Naito, N., Enomoto, H., Tsutaki, S., Tone, K., Marinsek, S., and Aniya, M.: Ice speed of a calving glacier modulated by small fluctuations in basal water pressure, Nat. Geo., 4, 597–600, 2011.

Taylor, G.: Tidal oscillations in gulfs and rectangular basins, Proceedings of the London Mathematical Society, 20, 141–181, doi:10.1112/plms/s2-20.1.148, 1921.

Thomas, R. H. and Bentley, C. R.: A model for Holocene retreat of the West Antarctic Ice Sheet, Quaternary Research, 10, 150 – 170, doi:10.1016/0033-5894(78)90098-4, 1978.

Thompson, J., Simons, M., and Tsai, V. C.: Modeling the elastic transmission of tidal stresses to great distances inland in channelized ice streams, The Cryosphere Discussions, 8, 2119–2177, doi:10.5194/tc-8-2007-2014, 2014.

Thompson, J. M.: The Short-Timescale Behavior of Glacial Ice, Ph.D. thesis, California Institute of Technology, 2013.

Tsai, V. C. and Gudmundsson, G. H.: An improved model for tidally-modulated grounding line migration, Journal of Glaciology, 61, 216–222, doi:10.3189/2015JoG14J152, 2015.

Vaughan, D. G.: Tidal flexure at ice shelf margins, J. Geophys. Res., 100, 6213–6224, 1995.

Vaughan, D. G.: How does the Antarctic ice sheet affect sea level rise?, Science, 308, 1877–1878, 2005.

Walker, R. T., Christianson, K., Parizek, B. R., Anandakrishnan, S., and Alley, R. B.: A viscoelastic flowline model applied to tidal forcing of Bindschadler Ice Stream, West Antarctica, Earth Planet. Sc. Lett., 319-320, 128–132, doi:10.1016/j.epsl.2011.12.019, 2012.

Walker, R. T., Parizek, B. R., Alley, R. B., Anandakrishnan, S., Riverman, K. L., and Christianson, K.: Ice-shelf tidal flexure and subglacial pressure variations, Earth Planet Sci. Lett., 361, 422–428, doi:10.1016/j.epsl.2012.11.008, 2013.

Walters, R. A.: Small-amplitude, short-period variations in the speed of a tide-water glacier in south-central alaska, U. S. A., Ann. Glaciol., 12, 187–191, 1989.

Weertman, J.: On the sliding of glaciers, J. Glaciol., 3, 33–38, 1957.

Weertman, J.: Stability of the junction of an ice sheet and ice shelf, Journal of Glaciology, 13, 3–11, 1974.

Wiens, D. A., Anandakrishnan, S., Winberry, J. P., and King, M. A.: Simultaneous teleseismic and geodetic observations of the stick–slip motion of an Antarctic ice stream, Nature, 453, 770–4, 2008.

Wilchinsky, A. V.: Studying ice sheet stability using the method of separation of variables, Geophysical & Astrophysical Fluid Dynamics, 94, 15–45, doi:10.1080/03091920108204130, 2001.

Williams, R. T. and Robinson, E. S.: The Ocean Tide in the Southern Ross Sea, Journal of Geophysical Research, 85, 6689–6696, 1980.

Wilmes, S.-B. and Green, J. A. M.: The evolution of tides and tidal dissipation over the past 21,000 years, Journal of Geophysical Research: Oceans, 119, 4083–4100, doi:10.1002/2013JC009605, 2014.

Winberry, J. P., Anandakrishnan, S., Alley, R. B., Bindschadler, R., and King, M. A.: Basal mechanics of ice streams: Insights from the stick-slip motion of Whillans Ice Stream, West Antarctica, J. Geophys. Res., 114, F01016, doi:10.1029/2008JF001035, 2009.

Winberry, J. P., Anandakrishnan, S., Wiens, D. A., Alley, R. B., and Christianson, K.: Dynamics of stick-slip motion, Whillans Ice Stream, Antarctica, Earth Planet Sci. Lett., 305, 283–289, doi:10.1016/j.epsl.2011.02.052, 2011.

Winkelmann, R., Martin, M. A., Haseloff, M., Albrecht, T., Bueler, E., Khroulev, C., and Levermann, A.: The Potsdam Parallel Ice Sheet Model (PISM-PIK), Part 1: Model description, The Cryosphere, 5, 715–726, doi:10.5194/tc-5-715-2011, 2011.

Winkelmann, R., Levermann, A., Frieler, K., and Martin, M. A.: Uncertainty in future solid ice discharge from Antarctica, The Cryosphere Discussions, 6, 673–714, doi:10.5194/tcd-6-673-2012, 2012.

Wuite, J., Rott, H., Hetzenecker, M., Floricioiu, D., De Rydt, J., Gudmundsson, G. H., Nagler, T., and Kern, M.: Evolution of surface velocities and ice discharge of Larsen B outlet glaciers from 1995 to 2013, The Cryosphere Discussions, 8, 6271–6301, 2014.

Zaron, E. and Egbert, G.: Estimating open-ocean barotropic tidal dissipation: The Hawaiian Ridge, Journal of Physical Oceanography, 36, 1019–1035, doi: 10.1175/JPO2878.1, 2006.

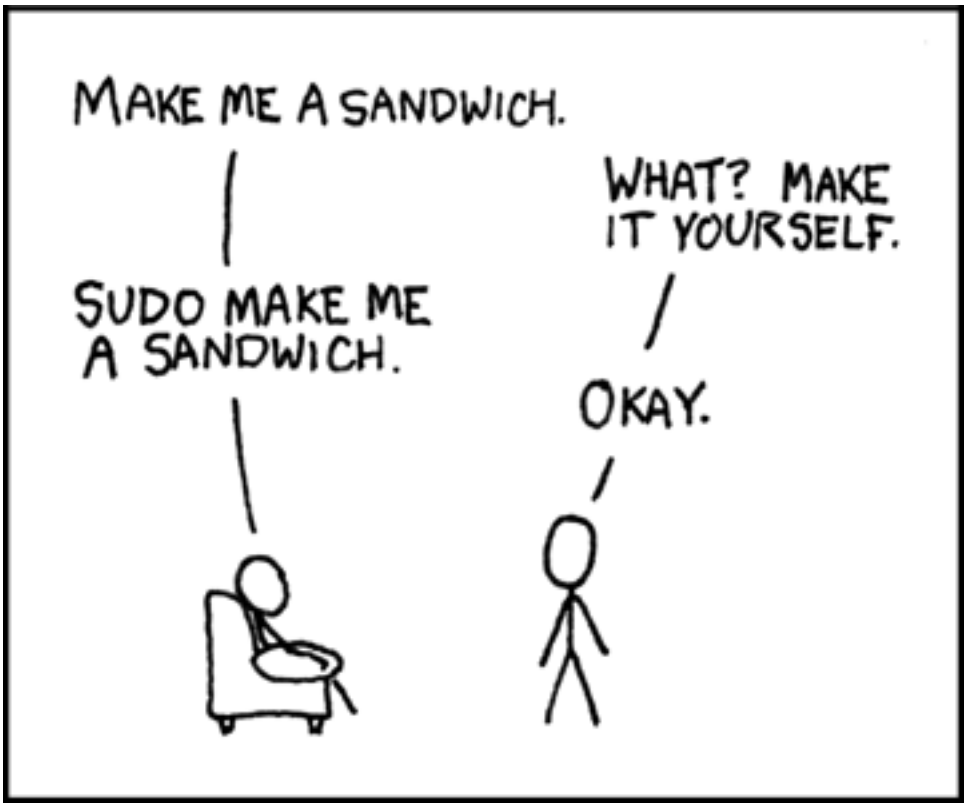
MAKE ME A SANDWICH.
SUDO MAKE ME A SANDWICH.
WHAT? MAKE IT YOURSELF.
OKAY.